

# Design Optimization of Linear Fresnel Reflector Systems

Sirimanna, M.P.G.

*Award date:*
2023

*Awarding institution:*
Coventry University

# Design Optimization of Linear Fresnel Reflector Systems

**By**

**Malambage Pubudu Gayan Sirimanna**

**PhD**

**December 2021**

# Design Optimization of Linear Fresnel Reflector Systems

**By**

**Malambage Pubudu Gayan Sirimanna**

**December 2021**


***A thesis submitted in partial fulfilment of the University's requirements for the Degree of Doctor of Philosophy***

## Ethical Approval



# Certificate of Ethical Approval

| | |
|---|---|
| Applicant: | Malambage Sirimanna |
| Project Title: | Design Optimization of Linear Fresnel Reflector Systems |

This is to certify that the above named applicant has completed the Coventry University Ethical Approval process and their project has been confirmed and approved as Low Risk

| | |
|---|---|
| Date of approval: | 12 Jan 2022 |
| Project Reference Number: | P130520 |

## Abstract

To keep global temperature rise within 1.5°C and meet global net zero targets, it has been suggested that the world needs around 6.7 GW of annual capacity additions from Concentrating Solar thermal Power (CSP) from 2020 to 2030. However, to realise this, improvements are needed to make the technology more cost efficient and attractive for investment. The Linear Fresnel Reflector (LFR) is an emerging CSP technology for power generation, yet needs to benefit from design improvements and cost reductions. This thesis aims to optimize the design parameters of an LFR to improve efficiencies and minimise energy costs. To begin with, optical and thermal models are developed and verified against existing baseline LFR systems. The research goes on to investigate how the optical and thermal models can be coupled together and solved simultaneously using optimization methods. Genetic Algorithm (GA) was selected after testing different optimization methods on a number of LFR designs. Simulations are carried out for performance and cost based objective functions: total theoretical efficiency and Levelized Cost of Electricity (LCOE), and five design variables are examined: mirror number, width and spacing; receiver height and operating temperature. The thesis further explores LFR systems using three different primary mirror types (flat, slightly curved and fully curved) and two alternative receiver temperature operating conditions (constant and variable). Three locations (Spain, China and Australia) are considered to evaluate how optimized LFR designs will change due to the region of installation. The maximum efficiencies for the alternative mirror configurations were found to be comparable, however the optimized design variables were significantly different. In comparison to using flat mirrors, an optimized LFR system using fully curved mirrors increased the total efficiency by 4.5% and reduced land area, mirror area and receiver height by 35%, 29% and 34%, respectively. The performance-based and cost-based designs were most sensitive to non-optimal values of receiver temperature and receiver height, respectively. Changes in mirror spacing were the least sensitive. Optimized results showed that design variable changes from existing systems can drop the LCOE up to 23%; highlighting the importance of highly accurate optimization of the system design. Although, the optimized designs did not vary much between the case study locations, LCOE showed a clear difference. This suggests that the LOCE is largely dominated by the component costs and amount of direct radiation rather than location dependant solar irradiance profiles. Optimized LCOE ranged from 0.074 to 0.083 (USD/kWh), lower than currently reported values for CSP (0.108 USD/kWh). A sensitivity analysis on cost parameters showed that a 20% drop of mirror costs would drop current LCOE by 9.7%. The method presented in this study can be adapted by manufacturers and researchers to optimize mirror-receiver layouts and operating conditions for other LFR configurations.

## Acknowledgements

This work has been supported by many to whom I would like to express my sincere gratitude. My special thanks to my director of studies, Dr Jonathan Nixon, for his guidance, patience and valuable insights. He has always been available whenever I needed him throughout this work. I was also fortunate to be involved in teaching activities with him, which enriched my PhD experience. I would also like to thank my second and third supervisors, Dr Mauro Innocente and Dr Janis Priede, for their continuous support. Their expertise and advice in different stages of this research have been vital in developing this thesis.

I am grateful to my PhD fellows and staff of the Centre for Fluid and Complex systems (FCS). The FCS has been a wonderful place to work with such wonderful persons around. I especially appreciate the support given by Dr Lorna Everall providing resources and sorting out administrative matters throughout. I am also grateful to Dr Philip Costen for proofreading the Thesis. I am very much in debt to Coventry University and FCS for providing me with a full studentship to carry out this research.

I would like to thank the researchers I met during conferences, anonymous reviewers and PhD fellows in the Doctoral Training Alliance (DTA). Their ideas and feedback have undoubtedly enriched this work. I am also grateful to my friends who supported me with proofreading and showing directions for improvements.

Last but not least, I am extremely grateful to my family and my parents. The journey towards completing this thesis has not always been smooth, especially when the Covid-19 pandemic began. Their sacrifices, understanding and love have always been my strength. So, I dedicate this thesis to my parents and family with love.

# Table of contents

## List of figures

## List of tables

# Nomenclature

## Variables

| | |
|---|---|
| $A$ | area ($m^2$) |
| $C$ | cost (€ or €/m or €/$m^2$) |
| $D$ | diameter (m) |
| $d_{cr}$ | cavity depth(m) |
| $g$ | gravitational acceleration ($m/s^2$) |
| $h_{conv}$ | convective heat transfer coefficient (W/ $m^2K$) |
| $h_r$ | receiver height (m) |
| $h_{rad}$ | radiative heat transfer coefficient (W/ $m^2K$) |
| $I$ | intensity of solar radiation (W/ $m^2$) |
| $k$ | thermal conductivity (W/ mK) |
| $K(\theta_T, \theta_L)$ | Incident Angle Modifier |
| $L$ | receiver length(m) |
| $N$ | number of hours of sunlight (h) |
| $n_m$ | number of mirrors |
| $Nu$ | Nusselt number |
| $P$ | parameters |
| $Pr$ | Prandtl number |
| $Q$ | heat transfer (W) |
| $Q_{loss}$ | heat loss to ambient air (W) |
| $Ra$ | Rayleigh number |
| $s_m$ | mirror spacing (m) |
| $T$ | temperature, (K) |
| $U_L$ | heat loss coefficient (W/ $m^2K$) |
| $W$ | plant width |
| $w_m$ | mirror width (m) |
| $w_r$ | receiver width (m) |

## Greek symbols

| | |
|---|---|
| $\varepsilon$ | emissivity |
| $\eta$ | efficiency |
| $\eta_o$ | optical efficiency |
| $\theta_i$ | incident angle (deg.) |
| $\theta_L$ | longitudinal angle (deg.) |
| $\theta_T$ | transverse angle (deg.) |
| $\sigma$ | Stefan-Boltzmann constant ($W/m^2K^4$) |
| $\sigma_{collector,error}$ | total collector optical error (mrad) |
| $\sigma_{rec}$ | equivalent receiver error (mrad) |
| $\sigma_{slope}$ | slope error (mrad) |
| $\sigma_{specularity}$ | specularity error (mrad) |
| $\sigma_{sun}$ | standard deviation of solar distribution (mrad) |
| $\sigma_{track}$ | tracking error (mrad) |

## Subscripts and superscripts

| | |
|---|---|
| $a$ | ambient air |
| $abs$ | absorbed |
| $ap$ | aperture |
| $c$ | glass cover |
| $col$ | collector |
| $const$ | constant |
| $conv$ | convection |
| $im$ | insulation material |
| $L$ | longitudinal direction |
| $lim$ | limit |
| $m$ | mirror |

| | |
|---|---|
| $max$ | maximum |
| $o$ | output |
| $opt$ | optimum |
| $pb$ | power block |
| $r$ | receiver or absorber |
| $rad$ | radiation |
| $sky$ | sky |
| $T$ | transversal direction |
| $th$ | thermal |
| $total, th$ | total theoretical |

**Abbreviations**

| | |
|---|---|
| ANN | Artificial Neural Network |
| CPC | Compound Parabolic Concentrator |
| CSP | Concentrated Solar thermal Power |
| GA | Genetic Algorithm |
| IAM | Incident Angle Modifier |
| IEA | International Energy Agency |
| LCOE | Levelized Cost of Electricity |
| LFR | Linear Fresnel Reflector |
| MCRT | Monte Carlo Ray Tracing |
| NREL | National Renewable Energy Laboratory |
| PSA | Plataforma Solar de Almería |
| PSO | Particle Swarm Optimization |
| PT | Solar Power Tower |
| PTC | Parabolic Trough Collectors |
| PV | Photovoltaics |
| SAM | System Advisor Model |
| SPD | Solar Parabolic Dish |

| | |
|---|---|
| SQP | Sequential Quadratic Programming |
| TES | Thermal Energy Storage |
| TMY | Typical Meteorological Year |

# 1

# Introduction

## 1.1 Background

Over recent history, the world's energy consumption has been continuously rising (Figure 1.1). Statistics show that the world's total energy consumption has nearly doubled during the last four decades, exceeding 400 quintillion joules per year (IEA 2021a). It is expected to grow continuously for years to come. For instance, the U.S. Energy Information Administration (2021) projects that world energy use will increase by around 50% by 2050 in comparison to 2020, mostly driven by the strong economic growth and population particularly in Asia. Irrespective of these rapid growths, there is an imperative need to produce the energy required for modern civilization.

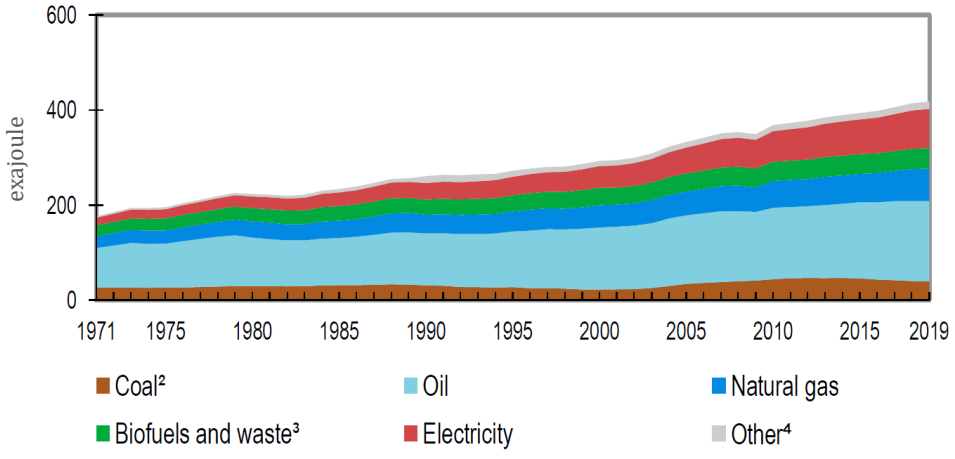


Figure 1.1: World total energy consumption from 1971 to 2019 by fuel, Source: IEA (2021) Key World Energy Statistics, All rights reserved

There are a host of worldwide challenges formed with efforts to fulfil the energy demand of the world. Coal, natural gas and oil collectively contributed to 80% of the world's total energy supply in 2019 (IEA 2021a). It shows that the world still highly depends on these energy sources, which are rapidly depleting with time. On the other hand, burning these fuels releases greenhouse gases, mainly carbon dioxide ($CO_2$), which is the prime reason for global warming. Climate change including more frequent and severe weather, sea-level rise and various environmental issues are just a few consequences of global warming, which affects millions of people worldwide, indicating that it is a global crisis of the era. In 2008, passing the Climate Change Act, the United Kingdom committed to ensure that the net UK carbon amount for the year 2050 is at least 80% lower than the 1990 levels (Department for Business, Energy & Industrial Strategy 2018). Later in the 2015 Paris Agreement, 195 countries representing 90% of global economic activities agreed to stretch national targets to keep the global temperature rise below 2°C (United Nations Climate Change 2018). While the policy level decisions are being made for regulating, $CO_2$ emission from fuel combustion has nearly doubled during the last four decades figuring to around 33600 million tons by 2019 (IEA 2021a). More than 99% out of this was from coal, natural gas and oil. Therefore, there is a dire need to mitigate $CO_2$ emissions from these conventional energy sources. Then again, the world is also forced to seek out sustainable renewable energy sources as alternatives for depleting conventional energy sources.

Solar energy has a global tremendous availability as a renewable energy source. A simple calculation shows that around 89000 TW of solar energy is received on the earth's surface, and within one and half hours it would provide more energy than the world can consume within one year. To harvest this inexhaustible energy source, there are two main solar power generation technologies currently in operation at a commercial level, namely solar photovoltaics (PV) and Concentrated Solar thermal Power (CSP). In a CSP plant, sunlight is concentrated onto a receiver using mirrors to generate heat. Typically, this heat is carried away by a working fluid to generate power using a steam turbine. One of the major challenges in solar power generation is the intermittent nature of solar energy. CSP technology has an inherited

advantage of being able to use thermal storage in comparison to electrochemical storage, which is often used alongside solar PV technology, producing dispatchable electricity. This makes CSP technology attractive, especially at a large scale (Lovegrove and Csiro 2012). A lower carbon footprint than solar PV (Desideri et al. 2013; Aqachmar et al. 2021) and the possibility of coupling with conventional thermal power plants are some of the additional benefits of CSP technology.

## 1.2 CSP technologies

In 200 BC, it is said that Archimedes used mirror-like panels to burn ships that attacked Syracuse city. Although the veracity of this story is still debatable, it shows that the idea of concentrating solar energy has been a topic of interest since ancient times. There have been several related inventions since the era of Archimedes. However, industrial level development appeared only in the 1980s in California (Lovegrove and Csiro 2012) and now it is becoming a remarkable power generation technology. With appropriate support, CSP could provide 9.6% of global electricity from solar power alone by 2050 (IEA 2010). The electricity cost generated by CSP has been rapidly decreasing over the years as seen in Figure 1.2 (IRENA 2020). However, CSP energy costs are still high in comparison to other renewables and in order to attain global Net-Zero targets, the International Energy Agency asserts that the world needs around 6.7 GW of annual capacity additions using CSP from 2020 to 2030. This is a significant annual growth of 31%, which must be supported by energy policies and further cost reductions (IEA 2021b). In order to reach these targets, CSP is currently being developed under four categories, outlined below

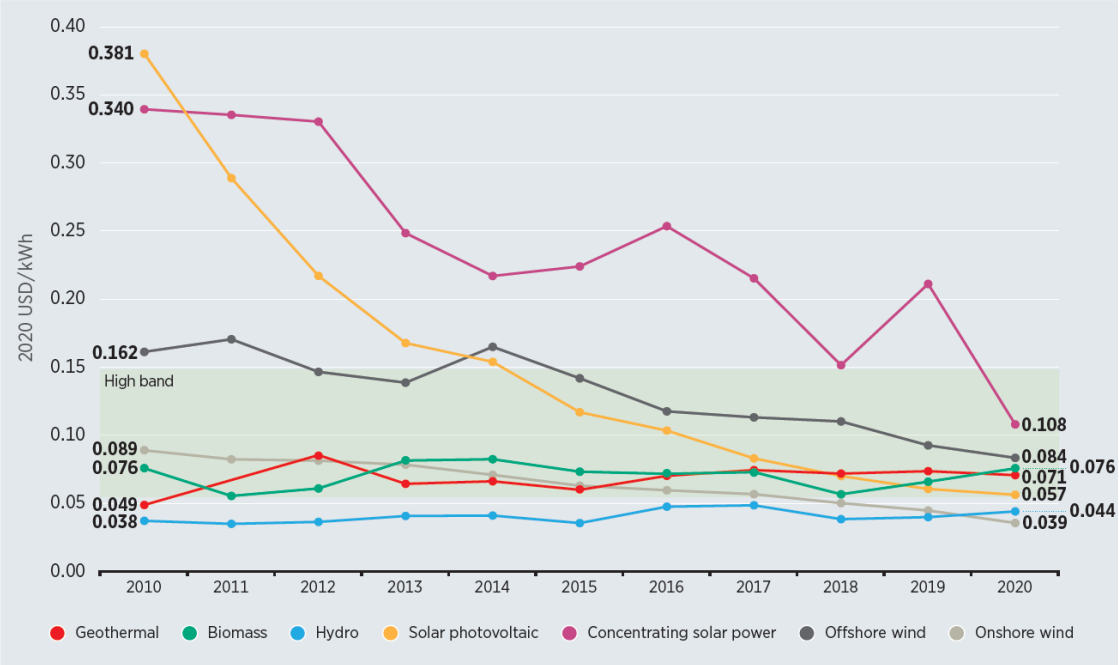


*Source: IRENA Renewable Cost Database*

Figure 1.2: Change of Levelized Cost of Electricity (LCOE) of renewables over the years, Source: (IRENA 2020) Renewable Power Generation Costs in 2020, All rights reserved

### 1.2.1 Parabolic Trough Collector

A Parabolic Trough Collector (PTC) is currently the most established CSP technology. The first graphically documented PTC was designed by John Ericsson at the end of the nineteenth century. Following different developments taking place over a century, the most outstanding design and implementation took place in the 1980s with nine plants known as SEGS (Solar Electricity Generating System) being commissioned in the Mojave Desert, California, USA. They have been acting as a "technology showcase" for other PTC developments since then, showing a prominent level of technical credibility and confidence (Moya 2012). Figure 1.3 depicts a parabolic trough power plant located in the Mojave Desert, California.

Figure 1.3: A 30MW parabolic trough power plant located at Kramer Junction in the Mojave Desert, California, USA (U.S. Department of Energy 2003)

PTC primarily consists of a parabolic shaped long mirror known as a parabolic trough. The mirror reflects incident solar radiation to an absorber or a receiver mounted on the focal line of the trough. Therefore, PTC is categorised as a line focusing technology. The mirrors, mounted on large supporting structures, can rotate around the absorber in order to track the sun from east to west. The central axis of the absorber therefore lies in the north-south direction in most of the PTCs, which is referred to as north-south orientation. A heat transfer fluid, water or thermal oil, flows through the absorber and delivers the heat extracted from the concentrated solar energy to a turbine, which normally runs on the Rankine cycle. There may be a series of heat exchangers and storage tanks between the turbine and the absorber depending on the design of the PTC.

### 1.2.2 Solar Parabolic Dish

The oldest build of a Solar Parabolic Dish (SPD) is reported in the Paris Universal Exposition in 1878. It was designed as an improvement to PTC, where a higher proportion of the absorber surface area can be utilised. The first developments similar to current designs were initiated around the 1980s in California, where the first Stirling engine unit called Vanguard was used on a parabolic dish concentrator (Gordon 2001). Currently, SPD systems consist of paraboloid shaped mirrors with

two axis tracking systems to track the sun throughout the day. The mirrors focus the solar radiation onto the focal point of the paraboloid where the energy can be absorbed by a heat engine or a working fluid in order to generate electricity (Figure 1.4).

Figure 1.4: The Maricopa solar plant, 1.5MW parabolic dish system, in Arizona, USA (United Sun Systems International Ltd, 2012), licensed under CC BY-SA 4.0

### 1.2.3 Solar Power Tower

The history of the Solar Power Tower (PT) dates back to the 1950s, where a set of flat mirrors were used to heat a boiler installed at an elevated height. This concept was expected to be adapted in high power installations since producing large paraboloid mirrors had been extremely expensive. It was proposed to break the parabolic mirror into facets and project them outward from the receiver to the ground, where they can individually reflect direct solar radiation onto a receiver (Baum, Aparasi, and Garf 1957). Today's PT plants consist of a large number of mirrors, known as heliostats, which can track the sun and reflect beam radiation to a receiver. The receiver is a type of heat exchanger mounted on a tall tower. Heliostats are typically placed around the tower in circular patterns (Figure 1.5). The thermal energy absorbed by the receiver is eventually delivered to the turbine by using working fluids.

Figure 1.5: The world's first commercial Solar Power Tower plant: PS10, 11MW plant located near Seville, Spain; Reprinted from (Islam et al. 2018), Copyright (2018), with permission from Elsevier

### 1.2.4 Linear Fresnel Reflector (LFR)

Augustin Jean Fresnel, a French optical physicist, revealed in 1918 that the effect of large lenses can be duplicated using many small lens components. This concept was later adapted in developing the LFR, and the name "Fresnel" systems has now become established. The first large system which had a construction similar to current developments was reported in 1961 (Mills 2012). Current LFR systems consist of long narrow flat or slightly curved mirrors capable of single axis tracking to reflect solar radiation onto a fixed absorber (Figure 1.6). The absorber may be covered with a secondary reflector to capture more solar radiation. The absorbed heat is then carried away by a heat transfer fluid or steam is generated inside the absorber itself.

LFR technology has been used for power generation as well as several other applications. Table 1.1 shows a list of selected LFR power plants built around the world. Most of these power plants have been designed for power generation using the steam Rankine cycle at the commercial level. The power generation capacity has been gradually increased over the years. Cogeneration is another major application where heat is generated in addition to electricity. This heat can be used for process heat, desalination or absorption cooling. In addition to these common applications

of LFR systems, several studies report other uses such as pyrolysis, fibre daylighting systems and solar cooking, as given in Table 1.2.

Figure 1.6: Puerto Errado 2, a 30MW LFR power plant located in Murcia, Spain (Zhu et al. 2014), Copyright (2014), with permission from Elsevier

Table 1.1: A list of selected LFR power plants built around the world (Bellos 2019; NREL 2021)

| Name | Country | Type | Status | Nominal Turbine/ Power Cycle Capacity (MW) | Year Completed |
|---|---|---|---|---|---|
| Dacheng Dunhuang | China | Commercial | Operational | 50 | 2019 |
| Llo | France | Commercial | Operational | 9 | 2019 |
| Dhursar (CLFR) | India | Commercial | Operational | 125 | 2014 |
| Puerto Errado 2 | Spain | Commercial | Operational | 30 | 2012 |

| | | | | | |
|---|---|---|---|---|---|
| Liddell | Australia | Commercial | Currently Non-Operational | 3 | 2012 |
| Kimberlina | USA | Demonstration | Currently Non-Operational | 5 | 2008 |

Table 1.2: Different LFR applications and relevant studies

| Application | Reference |
|---|---|
| Cogeneration: Heat production | (Dabwan and Mokheimer 2017; Burin, Lo Giudice, and Bazzo 2018; López, Restrepo, and Bazzo 2018; Moaleman et al. 2018) |
| Cogeneration: Freshwater production | (Askari, Ighball Baniasad and Ameri 2017; Askari, Ighbal Baniasad and Ameri 2018; Askari, Ighball Baniasad, Ameri, and Calise 2018) |
| Desalination | (Askari, Ighball Baniasad and Ameri 2016; Sharan and Bandyopadhyay 2017; Alhaj, Mabrouk, and Al-Ghamdi 2018) |
| Solar absorption cooling | (Bermejo, Pino, and Rosa 2010 ; Serag-Eldin 2014; Gallego, Antonio J. et al. 2019) |
| Other applications | (Farooqui 2015; Barbón et al. 2018b; Sánchez, Clifford, and Nixon 2018) |

### 1.2.5 A comparison between available CSP technologies

Table 1.3 shows a comparison between available CSP technologies. Being the most commercially used technology at present and with various developments over the years, PTC shows a high maturity with limited potential for improvements. PDC on the other hand has had limited attention, in spite of the potential to achieve the highest conversion efficiencies of about 30%. One of the main reasons behind this is

the substantial financial investment involved, which is about 10000 USD per kW installed (Schiel and Keck 2012).

Table 1.3: A comparison among different CSP technologies (Zhang et al. 2013; Liu et al. 2016; Islam et al. 2018)

| | PTC | SPD | PT | LFR |
|---|---|---|---|---|
| Capacity (MW) | 10-200 | 0.01-0.4 | 10-150 | 10-200 |
| Plant peak efficiency (%) | 14-20 | ~30 | 23-35 | ~18 |
| Annual average conversion efficiency (%) | 13-15 | 22-24 | 14-18 | 9-13 |
| LCOE (USD/kW h) | 0.26-0.37(no TES) 0.22-0.34(with TES) | - | 0.20-0.29 (6-7.5 h TES) 0.17-0.24(12-15 h TES) | 0.19-0.38 (no TES) 0.17-0.37(6 h TES) |
| Maturity | High, commercially proven | Low, demonstration projects | Medium, recently commercially proven | Medium, pilot plants, commercially available |

PT and LFR have been receiving growing attention in recent past years due to their greater potential to become dominant power generation technologies in future. Compared to other commercially available CSP systems, LFR shows some unique cost benefits in terms of mirrors, tracking system, operation and maintenance; compared to PT, the concentration ratio of LFR can be tailored to match the temperature limits of receiver materials (Zhu et al. 2014). Furthermore, being a less mature technology, LFR provides a significant outlook for improvement.

## 1.3 Approach to this work

Although the LFR is a relatively simple CSP technology to build and operate, modelling this solar collector is a complex problem. For example, it is far more optically challenging to model than a PTC, where only one parabolic mirror reflects direct solar radiation to a receiver tube (Cheng et al. 2018); an LFR's mirror layout is asymmetrical with changing irradiance angles and additional phenomena such as shadowing and blocking of reflected radiation from adjacent rows can become significant. As a result, there are lots of design parameters to consider when designing an LFR, such as mirror number, width, curvature, spacing; receiver size and height. Furthermore, a number of different receiver types can be coupled with the concentrator, which can change the optical and thermal performance of the system. However, with advancements in mathematical optimization techniques, enhanced ray tracing tools – to consider solar ray interactions between the mirrors and receiver surfaces – and improvements in computational power, there is an opportunity to improve the design process of LFR systems. For instance, improving the solar field design and application of different optimization methods on CSP design would be critical to make LFR more commercially attractive in future (Mills 2012; Vasallo and Bravo 2016). Modelling and design optimization of LFR systems remains a relatively unanswered area to date and will be a significant contribution to the area. This work will inform future design and operational decisions of LFR systems.

## 1.4 Research questions, aim and objectives

In order to address the work needed in section 1.3, the following research questions have to be answered. Then the aim and objectives of this work are formed accordingly.

### 1.4.1 Research questions

1. Can thermal and ray tracing models be coupled together and optimized for designing LFR systems?
2. How do different parameters (mirror types/operating temperatures/locations) and requirements (maximising performance/minimising energy costs) influence optimal LFR designs?
3. How sensitive are the optimal LFR designs to potential changes in costs and design variables?

### 1.4.2 Aim

To establish a framework for optimizing the performance and cost-efficiency of LFR systems for different applications and settings.

### 1.4.3 Objectives

1. To evaluate how knowledge on CSP optimization can be transferred to LFR design
2. To determine LFR design variables to be optimized and develop mathematical models to evaluate the performance
3. Validate thermal and optical models against baseline LFR systems
4. Develop a framework for integrating optical and thermal models with mathematical optimization and test different optimization algorithms
5. Evaluate the framework for different performance and cost based objective functions
6. Examine the effects of different mirror designs, solar radiation profiles and manufacturing cost variations on optimum LFR designs
7. Investigate the sensitivity of the design variables and cost assumptions, and determine which design variables are the most important to maintain high performance/low energy cost in LFR designs

## 1.5 Thesis structure

In Chapter 2 of this thesis, a comprehensive literature review is conducted on optimization studies of CSP systems. The state-of-the-art in LFR system optimization is discussed in detail and the research gap is established. Furthermore, how optimization studies have been conducted in other CSP systems is discussed to inform the design optimization of LFR systems. In Chapter 3, the methodology of this research is outlined. Modelling of LFR systems is discussed in Chapter 4. This chapter provides a detailed description of how optical and thermal models are developed, coupled and verified. Chapter 5 presents the optimization framework developed and the formulation of the optimization problem with relevant objective functions and design variables. Suitable optimization methods that work on LFR's coupled optical and thermal modelling approach are also determined in this chapter. The optimization of LFR systems based on performance and cost to answer the research questions is presented in Chapter 6 along with a detailed discussion. Chapter 7 provides the conclusions and recommendations for future work, highlighting each research question addressed and contribution to knowledge.

# 2

# Literature review

## 2.1 Introduction

This chapter provides an up-to-date literature review on CSP optimization. The purpose of this chapter is to identify common LFR configurations, design variables and parameters, to establish the research gap, and to explore the optimization of CSP systems to evaluate how existing knowledge can be transferred to LFR design. The design evolution of LFR systems, starting from early research to modern designs, is presented in section 2.2. Design optimization based on optical modelling, thermal modelling and economic modelling is then discussed in sections 2.3-2.5, respectively. Efforts on coupled optical and thermal modelling are discussed in section 2.6 and the significance of addressing such a design optimization is also highlighted. Sections 2.7-2.8 present the design optimization of other CSP systems to learn from more conventional technologies. Section 2.9 summarises all CSP related optimization studies to highlight potential design variables, objective functions, optimization methods and platforms to be used. Section 2.10 elaborates on the research gap identified following the literature review.

## 2.2 Design evolution of LFR systems

Numerous research has been carried out over the last few decades relating to the design of LFR systems. The first large system which had a construction similar to current developments is reported in 1961 (Mills 2012). The development of this technology has been affected largely by the first world oil crisis in 1973, international agreements on global warming and government incentives since then. In early research Singh, R. N., Mathur, and Kandpal (1980), from the Indian Institute of Technology, investigated the concentration characteristics of an LFR considering three design variables, where mirror

width and spacing were kept constant. Their study was based on simple flat surfaces, which were used as mirrors and receivers. Following their theoretical investigation, Choudhury and Sehgal (1986) fabricated a small prototype employing a tubular receiver (Figure 2.1). They yielded a stagnation temperature of 385° C, demonstrating the usefulness of this technology. Inspired by the work of Singh, Mathur, and Kandpal (1980), the optical design of LFRs with flat and tubular receivers was further discussed in subsequent research (Mathur, Kandpal, and Negi 1991a; Mathur, Kandpal, and Negi 1991b). The authors presented the concentration characteristics of flat and tubular receivers using numerical calculations. The aforementioned work acted as an inspiration for the further development of this technology.

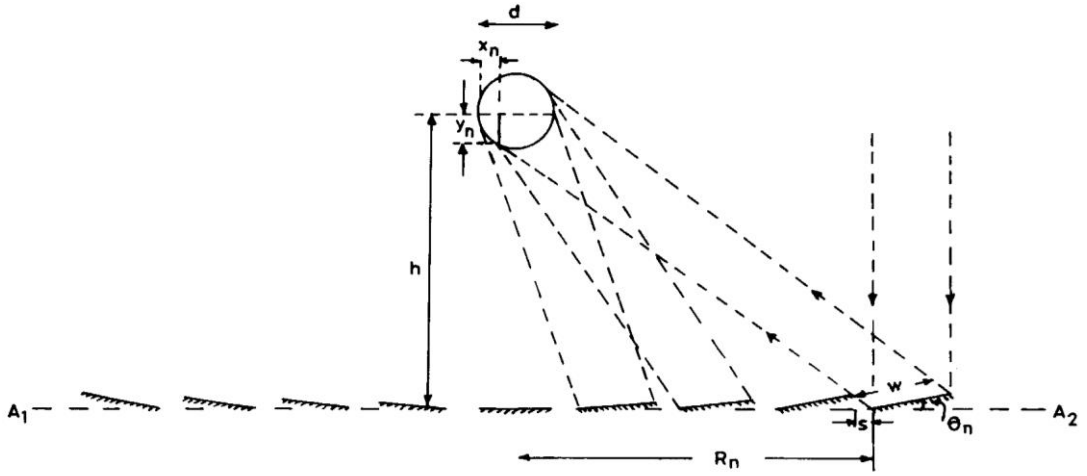


Figure 2.1: Schematic of an early LFR design; Reprinted from Choudhury and Sehgal (1986), Copyright (1986), with permission from Elsevier

Following on from early research conducted in the 1980s', LFR prototypes started to emerge from the late '90s. A 50MW power plant was installed in Liege, Belgium in 1999 by a company called Solarmundo (Häberle et al. 2002). This LFR system, known as Solarmundo(Figure 2.2), has been the point of reference for many subsequent research and installations. For instance, based on Solarmundo Morin et al. (2006) presented a roadmap towards developing an LFR system to be installed in PSA, Spain in 2006. By the end of 2009, three LFR plants had been installed worldwide: FRESDEMO (0.8 MW) and Puerto Errado 1(1.4 MW) in Spain; Kimberlina (5MW) in the USA (Bellos 2019). The first commercial level LFR plant, Puerto Errado 2, was completed in 2012 with a capacity of 30MW (Islam et al. 2018). The capacity of the plants has been gradually increasing since

then and Dhursar (125MW) in India is reported as the largest LFR system to date. Several other systems are under construction in various countries such as China, Morocco, India and France (Islam et al. 2018; Bellos 2019).

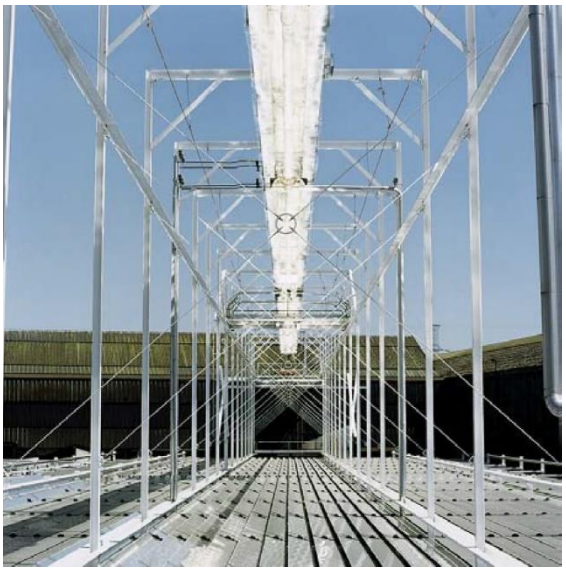

Figure 2.2: Solarmundo prototype installed in Liege, Belgium (Zhu et al. 2014), Copyright (2014), with permission from Elsevier

The performance of an LFR system largely depends on mirrors, mirror configurations and receiver designs. Over the years, research has been focused on improving LFR performance by employing different component designs. Figure 2.3 shows some of the new mirror field designs which have been studied by researchers to reduce two common energy losses in LFR, namely the blocking of solar rays and end losses. Figure 2.4 shows the most common types of receivers used in LFR systems: a single tube receiver with a secondary concentrator and a trapezoidal cavity receiver with multi-tubes. Some latest single-tube receiver designs have an evacuated tube in the middle to reduce heat losses as shown in Figure 2.5. Evacuated tubes have been widely used in PTC and solar hot water systems becoming a well-developed technology to date. Some of the well-known evacuated tubes, also known as HCE (Heat Collecting Element), in the market are Schott PTR® 70, RIOGLASS PTR® 70 and UVAC 70-7G (SCHOTT solar 2013; RIOGLASS Solar 2020).

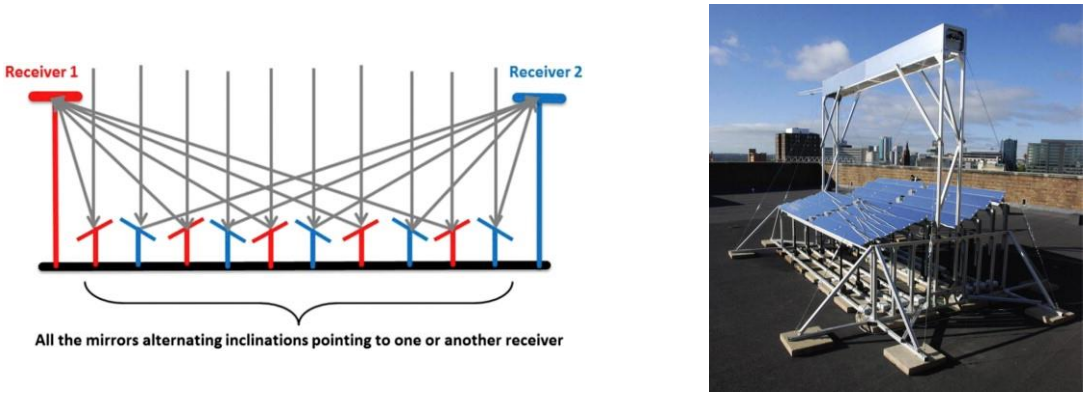


(a) (b)

Figure 2.3: (a) Compact Linear Fresnel Reflectors (CLFR) design built to avoid blocking effects (Montes et al. 2014) (b) Elevated mirror design (Nixon, Dey, and Davies 2013) to improve energy collection and reduce land area; Reprinted with permission from Elsevier

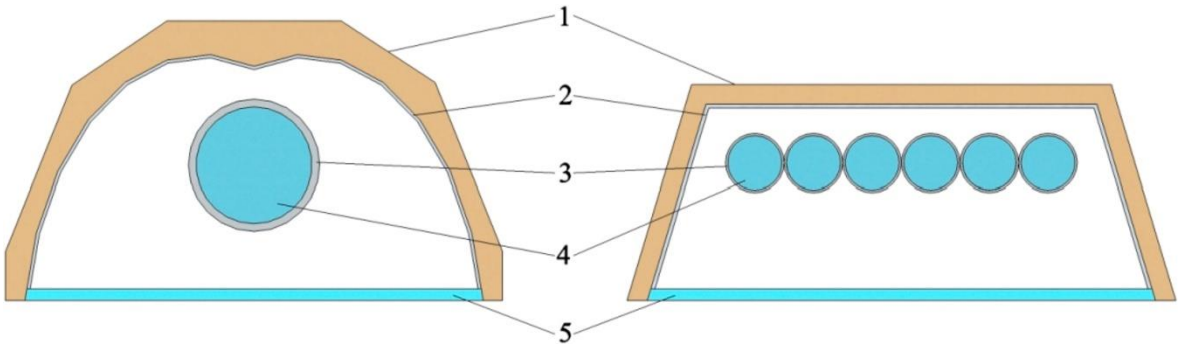


Figure 2.4: The most common two receiver designs in LFR: 1-Insulation, 2-Secondary reflective surface, 3-Steel tube, 4-Working fluid, 5-Flat glass cover; Reprinted from Pulido-Iparraguirre et al. (2019), Copyright (2019), with permission from Elsevier

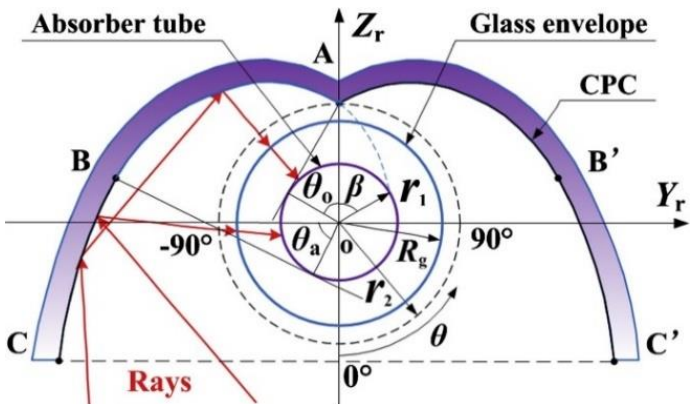


Figure 2.5: Compound Parabolic Concentrator (CPC) with evacuated tube; Reprinted from Qiu et al. (2015), Copyright (2015), with permission from Elsevier

Of the two common receiver types, the single-tube receiver with a secondary concentrator is frequently the most common design implemented in LFR plants. Some of the largest and well-known plants such as Solarmundo, FRESDEMO, Augustin Fresnel 1and Puerto Errado 2 employed this design (Montes et al. 2014; Islam et al. 2018) and a considerable number of LFR designs agreed in using the same (Pulido-Iparraguirre et al. 2019). The trapezoidal cavity receiver with multi-tubes seems to have advantages such as high efficiency in transferring heat to the carrier fluid, and flexibility to select the number of tubes to match preferred thermal and hydraulic requirements (Abbas, Muñoz, and Martínez-Val 2012). However, the multi-tube receiver is still in the research stage and no well-known prototype has been reported using this design. Figure 2.6 shows a schematic diagram of a well-established typical LFR system at present.

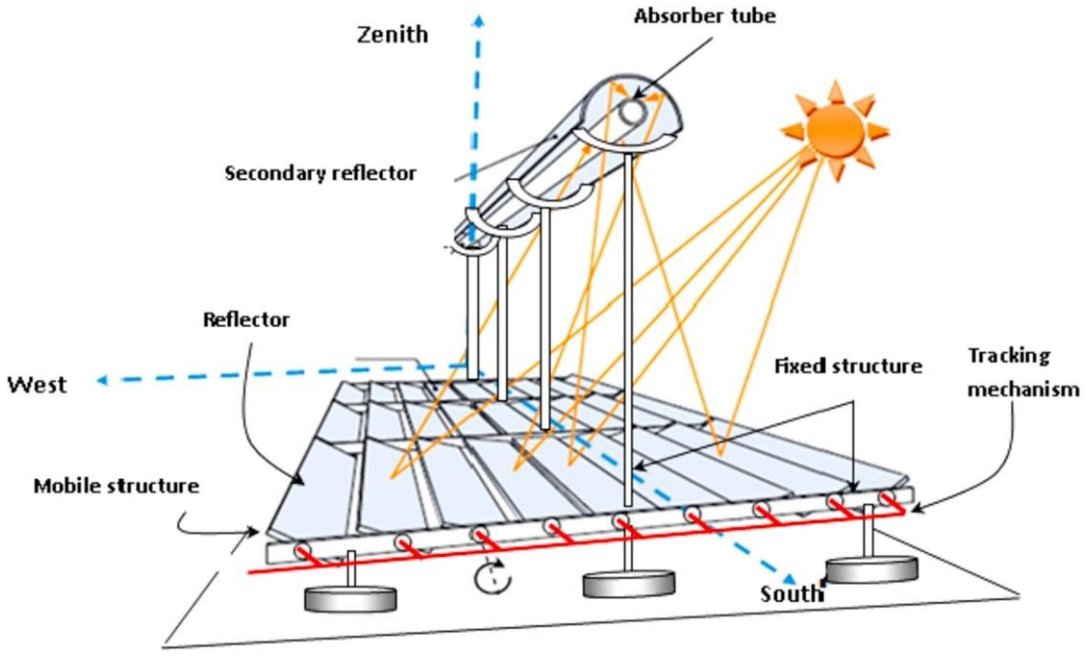


Figure 2.6: Schematic diagram of a typical LFR system; Reprinted from Ajdad et al. (2019), Copyright (2019), with permission from Elsevier

## 2.3 Optical modelling and optimization of LFR

Most of the research on LFR design optimization only started to appear a few years after the first pilot LFR plants such as FRESDEMO and Puerto Errado 1(Bellos 2019), which were installed around 2009. One of the first efforts to improve LFR performance by identifying the optimum design variables was performed by Facão and Oliveira (2011)

and Nixon and Davies (2012). Facão and Oliveira (2011) analysed a trapezoidal cavity receiver using numerical simulations. They used mirror field dimensions of an already installed LFR system and conducted a simplified ray tracing simulation. Computational Fluid Dynamics (CFD) was used to evaluate the overall heat transfer coefficient of the receiver. The authors proposed the best receiver dimensions for the predefined mirror field. Nixon and Davies (2012) presented a methodology to identify the optimum mirror spacing arrangement and conducted a cost-exergy analysis for four cost sensitivity scenarios to find the minimum cost. Their methodology, supported by ray tracing and a simple thermal analysis, allowed them to consider only a few mirror spacing alternatives based on transverse angle changes. Both aforementioned researches tried to find the optimum design by evaluating only a few design configurations while keeping serval important parameters fixed. These researches brought up the concept of optimization to the LFR system design and identified the requirement for more detailed optical and thermal simulations combined with a systematic optimization approach.

The analytical approach is an effective way to include many design variables in optimization and save computational time. In 2015, Abbas and Martinez (2015) considered variable mirror widths in addition to variable mirror spacing and tried to maximise receiver flux density through an analytical model. The authors showed an increased efficiency for constant widths and variable mirror spacing for a study performed on the FRESDEMO LFR plant. They found that variable widths and constant mirror spacing, however, did not show an efficiency improvement. This result provided justification for employing constant mirror widths in LFR systems, in addition to expected cost and maintenance benefits. The results of their study only showed trends of efficiency improvements and recommended a systematic optimization study for mirror field design variables such as mirror number, widths and spacing.

Compared to the analytical approach, Monte Carlo Ray Tracing (MCRT) is a more accurate method for optical simulations in CSP systems (Duan et al. 2020). Qiu et al. (2017) developed an optical model based on the MCRT method and combined it with Multi Objective Genetic Algorithm (MOGA) to optimize the aiming strategy of mirrors for two receiver types. Objective functions were selected as a flux non-uniformity index and the optical loss to obtain a uniform flux distribution on the receiver. Compared to the traditional one-line aiming strategy, their new MOGA optimization strategy showed that

flux uniformity can be obtained at the expense of optical efficiency. However, they did not investigate how different mirror field parameters affect the optimized results. As there was no work published on LFR mirror field optimization, Abbas et al. (2017) tried to fill this gap by addressing the optical design and calculating the flux intensity at the receiver using an MCRT code. They analysed the variation of exergy efficiency for different mirror numbers, filling factor and collector width. However, to save computational time during the optimization, the authors had to use a set of pre-designs for the solar field without incorporating the MCRT codes in the optimization process. By the end of 2017, MCRT codes had been embedded in LFR optical optimization studies however, the mirror field design had not been sufficiently addressed.

There have been studies on combining MCRT with Particle Swarm Optimization (PSO) to improve the efficiency of the optimization. Cheng et al. (2018) presented a novel optimization model for LFR, combining MCRT with the PSO method as an alternative to inefficiency associated with applying conventional optimization models, which had originally been designed for PTC. The new optical optimization model was developed on a FORTRAN platform combining MCRT with PSO. The code was validated using SolTrace and TracePro by comparing solar flux distribution on the absorber. The authors found that flat mirrors on LFRs can be optimized to obtain an annual optical efficiency of over 60%, compared to a similar configuration with cylindrical or parabolic mirrors, showing that it would be a substantial cost-effective improvement as flat mirrors can be easily manufactured (Cheng et al. 2018). Another study has been carried out using the same ray tracing and optimization method, which has been highlighted as an improvement to Cheng et al.'s (2018) study (Ajdad et al. 2019). They developed a calculation code (named OPSOL) to trace a solar ray based on a Monte Carlo algorithm in order to obtain solar energy captured by the absorber. One of the main objectives of the study was to successfully implement PSO methods on LFR by forming a coupling strategy between the MCRT algorithm and the optimization method. Therefore, in their work, the authors highlighted the optimization process further and considered three cases based on the geometrical configuration of the collector. Although both of the above studies managed to include some mirror field parameters (e.g. mirror width) in the optimization, important parameters, such as mirror number, had been fixed based on existing prototypes. In this way they could reduce the number of parameters to be optimized and

reduce the computational time. However, the main focus of these studies was to present the development of a new method, its validation and implementation.

Some studies have focused on improving LFR performance by proposing novel changes to a standard design. Pulido-Iparraguirre et al. (2019) presented an optimized optical design considering three geometrical changes proposed from a standard collector. Tilting the mirror field along with the receiver and displacement of the receiver, which had been previously studied by different researchers, were incorporated into their design. They also introduced a novel modification by tilting a segment of the mirror field. To analyse the new changes optically, they developed an in-house ray tracing code, which was validated against an open source ray tracing software. The authors concluded that an energy collection enhancement from 2% to 61% can be achieved by incorporating the new modifications compared to a standard LFR design. However, their conclusions were mainly based on an optical analysis only. Moreover, the optimization approach was to conduct many simulations around a selected LFR system and select the parameters, which provided the best performance.

Reducing the end losses has been another method of improving energy performance, especially for small scale LFR systems. Barbón et al. (2016) studied the lateral variation of solar energy received on an absorber of small scale LFR plants focussing on analysing the end loss and reflected light loss. These losses are not typically considered as they can be relatively small in large scale plants with long receiver tubes. The authors developed a mathematical model that enables the absorber's position and length to be optimized based on numerical integration. The authors extended their study on small scale systems by applying the aforementioned mathematical model to find the optimal arrangement for several LFR systems installed on an urban building roof (Barbón et al. 2018a). An in-house code for ray tracing was developed and the effect of roof type and orientation was analysed. However, according to the objective of their study, the three optimization algorithms, developed based on a packing mathematical problem, did not cover mirror field and receiver parameters in detail.

## 2.4 Thermal modelling and optimization of LFR

Optimizing the thermal design of LFRs has been mainly based on CFD simulations. Facão and Oliveira (2011) analysed a trapezoidal cavity receiver using CFD to evaluate the overall heat transfer coefficient considering all three heat transfer models, conduction, convection and radiation. The authors proposed the best receiver insulation thickness and cavity depth based on the minimum heat transfer coefficient. However, the best solutions were based on solar flux received on a predefined mirror field and for a few distinct values of design variables. Moghimi, Craig, and Meyer (2015) further extended the work of Facão and Oliveira (2011) by including three more design variables and considerably more CFD simulations. They also tried to minimise the wind resistance area in addition to the heat loss. A two-dimensional ANSYS fluent simulation was carried out assuming a uniform temperature of the receiver pipe. Solar radiation absorbed by the receiver was simulated based on the mirror field of the FRESDEMO prototype and introduced to the model as a uniform tube temperature. They initially conducted 79 CFD simulations for seven design variables to find an optimum using the Response Surface Method (RSM). The authors provided a set of candidate solutions for the geometry of the receiver suggesting the possibility of having several optimum designs. This research shows that the receiver optimization has been isolated from the mirror field design to avoid complexity. Moreover, the selection of the optimum design has been based on only a few to several dozens of distinct simulations.

## 2.5 Economic modelling of LFR

Although several cost analysis studies are found in the literature, accurate cost breakdowns of LFR systems are still rare. The most comprehensive cost modelling to date for a large-scale LFR plant has been presented by Mertins (2009). Their cost breakdown has been based on the Solarmundo project, a large-scale LFR prototype built in Liège, Belgium. The Mertins' (2009) study provided a detailed cost breakdown with cost coefficients for the primary mirror area, receiver structure, mirror gaps and receiver costs. Furthermore, other costs, such as the power plant unit and infrastructure, were also provided. Nixon and Davies presented a simple method to calculate the cost of an LFR system (Nixon and Davies 2012). They divided the total cost into four components:

frame, land, concentrator and receiver. These costs were directly proportional to the collector size, and mirror and receiver areas. A detailed study on cost estimation relationships has been presented by Barbón et al. (2019) considering manufacturing and other related costs. Since their model had been developed for small-scale LFRs, Bayón-Cueli et al. (2020) later applied the cost model to determine the optimum LFR distribution on building roofs based on minimum cost. In their model, the costs of the mirrors and the frame were directly proportional to the mirror area, neglecting the mirror spacing cost. The receiver cost was taken as a function of the mirror area and absorber length. All costs were expressed in terms of mirror width, mirror area, receiver height and the number of mirrors. However, some of these cost components were specific to small-scale systems, which suited their study, but would not be applicable to large prototypes or commercial level plants.

Some of the LFR optimization studies have conducted an economic analysis as a part of their study. Most of these studies use the cost models presented by Mertins (2009). Moghimi, Craig, and Meyer (2017) used Mertins' (2009) model to calculate the LCOE of a trapezoidal cavity receiver. Rungasamy, Craig, and Meyer (2019) used the same cost model to compare a standard Compact Linear Fresnel Reflector (CLFR) against two optically optimized etendue-conserving CLFRs. A different cost model to Mertins (2009), has been presented by Marugán-Cruz et al. (2019) to simulate the performance of a Direct Steam Generation (DSG) LFR plant. They also provided the cost values for many parameters, such as land and mirror areas, storage, power block, labour, operation and maintenance. Their study, however, did not break down the costs based on different mirror field parameters, such as the number of mirrors and receiver height. Furthermore, some of the references where the cost values were taken from are traced back to studies on PTC systems. This shows the scarcity of LFR cost data and studies are typically focused on LCOE comparisons only.

## 2.6 Combined optical, thermal and cost optimization of LFR systems

Simultaneous optical and thermal performance analysis requires complex simulations, which often become challenging to handle in the optimization stage. Most of the conventional optimization methods do not respond well to such a complex mathematical model. Moghimi, Craig, and Meyer (2017) tried to address this complexity by following a

two-step approach. They initially carried out an optical simulation for a mirror field and a trapezoidal receiver, and its results were subsequently used for a thermal analysis and optimization by the response surface method in ANSYS DesignXplorer. Unlike many other studies, they included a detailed cost model, a global optimization method, and both receiver and mirror field parameters in their study. However, by taking the stepwise approach, they avoided the simultaneous optical and thermal simulation. Furthermore, their approach avoided including the receiver temperature in the optimization and it is one of the most critical design variables that affect the overall system performance.

An effort to conduct an LFR mirror field optimization based on cost has been presented by Boito and Grena (2016). They optimized non-uniform mirror width, spacing and focal length based on plant cost per annual solar radiation. Their model, which was based only on the geometric optical collection of a flat horizontal receiver, did not include surface optical properties or thermal properties. Although their study had been based on cost optimization, neither an energy analysis nor heat loss calculation was carried out. The authors recommended including a thermal analysis, a more detailed receiver, optical properties and optical errors in further work.

Roostaee and Ameri (2019) tried to embed a thermal analysis in an optimization of an LFR mirror field with a trapezoidal cavity receiver by following an analytical approach. Starting with obtaining mirror width, they followed a stepwise approach to optimize each parameter. In the final step, the heat loss for different temperature ratios for the receiver was calculated to check the suitability of the design. However, the authors found that their method of treating the temperature needs improvements. They also concluded that an LFR optimization based on optical analysis alone, without considering the effect of receiver heat loss, was ineffective. Furthermore, they recommended conducting a detailed energy performance analysis simultaneously while optimizing the design variables.

A comprehensive LFR design optimization has to deal with both optical and thermal performance simultaneously as solar energy gains and heat losses are equally important to obtain the energy or power output. A study conducted by Roostaee and Ameri (2019) demonstrated that the receiver dimensions and its heat loss are dynamically connected to mirror field design. Furthermore, addressing both optical and thermal design leads to a more accurate cost of energy analysis. Researchers who tried to develop an accurate

cost of energy analysis or detailed energy models, (Boito and Grena 2016; Moghimi, Craig, and Meyer 2017; Roostaee and Ameri 2019), highlight two common directions as requirements for future work. Firstly, both receiver and mirror field design variables need to be included in an optimization. Secondly, comprehensive optical and thermal models need to be developed, which are dynamically linked.

## 2.7 Optical simulation and optimization of Solar Power Tower systems

As Solar Power Tower (PT) systems have been far more developed than LFR technology, PT systems are investigated to learn from their design optimizations. Studies on optical simulation and optimization of PT systems show more similarity with each other compared to studies on LFR systems. The optical efficiency of PT systems is expressed as a multiplication of five efficiencies or factors. This includes the cosine effect, atmospheric attenuation, intercept factor (or spillage), shading and blocking efficiency and reflectivity of mirrors (Besarati and Goswami 2014; Farges, Bézian, and El Hafi 2018; Wang, J., Duan, and Yang 2018; Saghafifar, Gadalla, and Mohammadi 2019). The cosine effect is caused by the required orientation of the heliostat to reflect a solar ray onto the tower. A decrease in effective mirror reflective area due to this effect is proportional to the cosine of the angle between the mirror surface normal and the incident solar ray. Atmospheric attenuation considers the different effects of the atmosphere on the reflected rays such as scattering and absorption. Optical simulation on PT systems mainly differs depending on the method used to treat the intercept factor, shading and blocking.

The intercept factor (or interception efficiency) and shading and blocking factors are the most computationally intensive parameters to calculate. The intercept factor, which represents the fraction of solar rays hitting the receiver surface after having been reflected by the heliostat, depends on the location of the heliostat, sun shape error, optical errors and tracking errors. Some authors refer to this parameter as spillage, which is opposite to the intercept factor, representing the rays missed by the receiver. The calculation of shading and blocking factor requires additional computational effort as it depends on the locations of neighbouring heliostats in addition to its own location with respect to the receiver tower. It is important to note that the sun's position during the day has to be considered in the above calculations. In optical simulations of PT systems,

pre-developed analytical models are used to calculate the intercept factor. Commonly used models are HFLCAL, developed by the German Aerospace Centre (DLR), and UNIZAR, developed at the University of Zaragoza, Spain (Besarati and Goswami 2014). To calculate the shading and blocking factor, analytical and geometrical projection methods such as the Sassi (1983) method are used. A more comprehensive description of other models and methods is found in Rizvi et al. (2021).

PT optimization studies are typically based on applying analytical methods and models such as HFLCAL and UNIZAR for different problems. The HFLCAL model has been mostly used in these studies, as it is much simpler and slightly more accurate than UNIZAR (Besarati and Goswami 2014; Wang, Duan, and Yang 2018). Using the HFLCAL model: Besarati and Goswami (2014) proposed a new method to improve the computational time of shading and blocking efficiency. They maximised the overall solar field efficiency of a selected heliostat field and found their method considerably reduced the computational time; Besarati, Goswami, and Stefanakos (2014) optimized a heliostat field for an optimal aiming strategy for uniform flux distribution on the receiver; Ghirardi et al. (2021) presented a heliostat layout optimization for maximising overall efficiency rather than annual power production. Gallego, A. J. and Camacho (2018) used both the HFLCAL and UNIZAR models in their study, which was based on the evaluation of a distributed heliostat field design approach instead of the common centralised design approach. The analytical approach used in PT optimization studies has enabled fast optical simulations for large heliostat fields.

Instead of using analytical methods such as HFLCAL, which are not very efficient for analysing solar flux in complex setups, only a few researchers have tried the alternative ray tracing approach. Wang, K. et al. (2016) developed a novel MCRT model to simulate radiation heat transfer in a PT's cavity receiver using the Gebhart method. Their model was later used to identify the best aiming strategy for PT considering solar flux distribution inside a cavity receiver (Wang, K. et al. 2017). The distribution of aiming points on the aperture and heliostat were simultaneously optimized within the code. The authors found that the flux uniformity on the inner surface of the receiver was more important than what was on the aperture. Their optimization was performed on a rather small heliostat field as a case study, and they presented some guidelines on how the optimization can be extended to a large heliostat field using the well-known PS10 plant

in Spain. Farges, Bézian, and El Hafi (2018) developed an optical model using MCRT and proposed a redesign for the collector field of the PS10 leading to an improvement in energy collection. Heliostats were divided into six groups based on the size, and their width and heights were optimized using stochastic PSO. Typical Meteorological Year (TMY) data was used to eliminate some of the assumptions made by previous studies. The studies on the ray tracing approach in PT optimization are limited and focused around an existing power plant such as PS10.

In addition to PT optimization based on optical performance, some studies proposed design improvements using LCOE based optimization and novel low cost designs. Collado and Guallar (2016) proposed a two-stage optimization methodology to design the heliostat field of large PT plants. Initially, energy collected by the heliostat field is maximised for a set of selected combinations of design variables. In the second stage, optimization of LCOE is carried out with the help of a capital cost model used in the System Advisor Model (SAM). They concluded that the optimum design of the plant strongly depends on the temperature of the receiver surface. Saghafifar, Gadalla, and Mohammadi (2019) designed and optimized a field with non-equal heliostats based on the optical efficiency and LCOE. The authors developed a new code called AINEH (Analysis of Implementation of Non Equal Heliostats) for this purpose and conducted a heliostat field redesign for the PS10 power plant. In their study, LCOE was calculated based only on the energy recovered by the heliostat field, neglecting the heat losses. To cut down the cost of tracking devices, Hu and Huang (2018) proposed a new tracking method by mounting heliostats and a receiver on a tracking device. Optical efficiency, blocking and shading factor were numerically calculated and the best performing design parameters were graphically identified. They found that the new design was highly efficient compared to conventional designs; however, they did not conduct a cost analysis for their new design. These PT optimization studies highlight the need for conducting a reasonable thermal analysis alongside a cost analysis.

Almost all of the PT optimization studies are based on optimizing a heliostat field, which follows a certain geometrical pattern. The location of a heliostat in the geometrical pattern is obtained by deterministic rules. Some of the commonly used patterned layouts are radial cornfield, rectangular cornfield, campo and bio-mimetic. In some designs, the rows are staggered to gain a better performance (Rizvi et al. 2021). The patterned layout

designs have made the optimization of PT heliostat fields possible with reasonable computational power. There have been some efforts on pattern-free heliostat field optimization (Carrizosa et al. 2015; Yang, Lee, and Lee 2020), which have brought more flexibility around conventional pattern layouts. Design variables for the layout optimization have been taken as the dimensions, orientation and location of the heliostats, while the tower height has been kept as a constant except in very few studies such as Ghirardi et al. (2021). Objective functions in PT optimization studies have been based on solar energy incident on the receiver on a daily or yearly basis. Different studies use slightly different terminology based on insolation weighted efficiency (Besarati and Goswami 2014; Saghafifar, Gadalla, and Mohammadi 2019; Ghirardi et al. 2021) or optical efficiency (Wang, Duan, and Yang 2018; Yang, Lee, and Lee 2020). Although optimization methods such as PSO have been used in some studies (Farges, Bézian, and El Hafi 2018), Genetic Algorithm (GA) has been extensively used in PT optimization studies (Besarati and Goswami 2014; Wang et al. 2017; Gallego and Camacho 2018; Wang, Duan, and Yang 2018; Saghafifar, Gadalla, and Mohammadi 2019).

Generally, PT optimization studies are purely based on optical analysis. Almost all of the studies have not considered heat loss and tower operating temperatures. Some studies use rough estimation methods such as using efficiency factors to account for heat losses and power block efficiencies. Furthermore, most optical analyses have been based on pre-developed analytical models. An optimum heliostat layout has been identified around a standard layout pattern. This setup has resulted in fast optical simulations capable of analysing annual weighted efficiencies. LCOE analyses are based only on the optical energy received on the receiver without considering the thermal energy losses. The latest studies are focused on addressing the aforementioned limitations.

## 2.8 Parabolic Trough and Solar Parabolic Dish systems

Although Parabolic Trough Collector (PTC) and dish systems are the oldest CSP designs, design optimization studies are as not common as in the other two common technologies. One of the main reasons is that PTCs and Solar Parabolic Dish (SPD) systems are significantly optically different to LFRs and PTs, where a large number of mirrors are focused on one receiver. PTCs and dish systems have a dedicated mirror for a receiver and parabolic geometries always focus solar rays to a focal line or a point. Furthermore,

the mirror and the receiver track the sun as a single unit, whereas the orientation of the mirrors changes with respect to the receiver in LFR and PT systems. These differences create a significantly simplified solar ray interaction between the receiver and the mirror of a PTC or a dish system.

There have been some efforts to identify the optimum receiver and mirror geometry parameters through optical modelling of PTC. Hoseinzadeh, Kasaeian, and Behshad Shafii (2018) analysed the effect of the geometric changes in the component of a PTC. They selected three parameters, rim angle, aperture and receiver diameter, to control the local concentration ratio. The MCRT code was developed and the three parameters were changed simultaneously to improve the concentration ratio and optical efficiency. As an improvement to conventional cylindrical and parabolic trough mirrors, Tasi presented a new mirror geometry using the free-form surface creation method for a heat-pipe receiver (Tsai 2016). A skew ray tracing approach was followed to obtain solar irradiance received on the absorber and the geometry of the collector was then optimized to achieve uniform solar flux distribution on the absorber. This new design showed a considerable improvement compared to conventional trough designs. The aforementioned studies, however, did not require employing a specific optimization method based on the problems they addressed.

The use of GA for multi-parameter optimization of a PTC receiver was reported by Guo and Huai (2016). Their objective was to address the complex interplay of different thermal parameters in the system since the optimal performance cannot be achieved by varying a single parameter while others are kept constant. Furthermore, they incorporated the second law analysis into their model considering the high degree of irreversibility of the problem. Therefore, the authors selected exergy efficiency as one of the objective functions for the optimization while the other being thermal efficiency. They selected four parameters to be optimized, namely mass flow rate, average working fluid temperature, diameter and wall temperature of receiver. They found that the temperature had the greatest effect on the exergy efficiency in comparison to other parameters used.

Several studies report efforts to find the optimized designs considering the entire mirror field, power block parameters and other auxiliary systems. Desai, Kedare, and Bandyopadhyay (2014) proposed a methodology to determine the optimum design

radiation level in PTC plants to screen various design objectives during the conceptual design level. They considered characteristics of both the collector field and the turbine to evaluate thermodynamics and investment, operational and maintenance costs of power plants. For the cases analysed, they concluded that the cost optimum design radiation level is lower compared to that of the thermodynamically optimum level. Furthermore, a comparison showed that optimum design radiation in LFR plants was always lower than in PTC plants. In a later study, Desai and Bandyopadhyay (2015) carried out a thorough analysis on the energy and costs of PTC plants. They studied the effects of changing turbine parameters such as inlet temperature and pressure, plant size and modifications of the Rankine cycle on LCOE. The above studies do not use a specific optimization method such as GA. The use of Artificial Neural Network (ANN) to optimize a PTC plant from a set of pre-designs was later reported by Boukelia, Arslan, and Mecibah (2016). They carried out techno-economic optimization of PTC considering the solar field, thermal energy storage, power block and fuel backup system. The authors optimized five parameters, ambient temperature, the intensity of beam radiation, solar multiple, collector row spacing and hours of thermal energy storage, based on LCOE. The System Advisor Model(SAM), which uses TRNSYS software and Solar Thermal Electric Components model library, and EBSILON software were used to simulate 1024 different pre-designs. None of the above studies has used an optical analysis method such as ray tracing as their effort was to consider the entire power generation system. Furthermore, only Boukelia, Arslan, and Mecibah (2016) used a metaheuristic method for optimization.

Optimization studies on Solar Parabolic Dish systems (SPD) are less common compared to other CSP systems. Ahmadi et al. (2013) conducted a comprehensive thermo-economic multi-objective optimization study on an SPD collector using GA. A detailed thermodynamic model was developed and coupled with an economic model to form three objective functions, a thermo-economic factor, power output and thermal efficiency. Five decision variables were defined based on working fluid temperature, irreversibility, temperature and heat transfer areas of source and sink. Three well-known decision making methods, TOPSIS, LINMAP and fuzzy Bellman-Zadesh, were used to select the optimum solution from the Pareto frontier obtained from the optimization. Another GA-based SPD optimization was presented by Yan, J., Peng, and Cheng (2018) for a novel design of a dish concentrator formed by discretising a conventional parabolic dish design. A previously developed ray tracing code based on the axisymmetric characteristic of the

novel collector was used for optical simulation. They combined the ray tracing code with GA to optimize the novel concentrator by minimising the flux non-uniformity index of the absorber surface. A cost optimization based on a detailed structural analysis for an SPD was presented by Glynn John and Lakshmanan (2017). In their study, the size of the dish was optimized using a graphical method for minimum cost, subject to wind-load resistance constraints. According to available literature, GA has been the most common PT optimization method while having cost-based objective functions and a couple of decision space variables.

## 2.9 Design variables, objective functions, optimization methods and platforms used in CSP optimization

Table 2.1 presents a list of different CSP optimization studies showing design variables, objective functions, optimization methods and platforms.

Table 2.1: A summary of CSP optimization studies

| Reference | CSP Technology | Maximise/minimise /Optimize | Variables | Model/simulation | Computational platforms/ programming languages/simulation software | Optimization Method/Approach |
|---|---|---|---|---|---|---|
| (Pulido-Iparraguirre et al. 2019) | LFR | Rays impinging on the receiver | Geometrical parameters of the mirror field | MCRT based optical model | Matlab | Exhaustive |
| (Roostaee and Ameri 2019) | LFR | Ray spillage | Receiver wall angle and width, mirror width | Analytical optical | - | Graphical, exhaustive |
| (Ajdad et al. 2019) | LFR | Daily optical efficiency | Geometrical parameters of the mirror field | MCRT based optical model | OPSOL code | PSO |
| (Barbón et al. 2018) | LFR | Collection area | Mirror field width and length, spacing between reflectors | Optical, Geometric(for reflectors) | Mathematica, Matlab | Exhaustive |
| (Cheng et al. 2018) | LFR | Nominal annual optical efficiency | Mirror width, focal length, | MCRT based optical model | FORTRAN | PSO |

| | | | | | | |
|---|---|---|---|---|---|---|
| | | | mirror width to gap ratio, dimension of a single tube receiver | | | |
| (Qiu et al. 2017) | LFR | flux non-uniformity index, optical loss | Aiming point location | MCRT based optical model | FORTRAN | GA |
| (Abbas et al. 2017) | LFR | Exergy efficiency | Number of mirrors, filling factor, collector width | MCRT based optical model | - | Univariate, Fibonacci |
| (Moghimi, Craig, and Meyer 2017) | LFR | Solar energy received, receiver heat loss and insulation area, Plant installation cost | Receiver optimization: cavity shape, tube arrangement, tube number, mounting height, insulation thickness; Mirror optimization: number, width, gap and focal length | Optical, thermal and cost | ANSYS: Workbench, Fluent, DesignXplorer; SolTrace; Excel VBA | Multi Objective Genetic Algorithm (MOGA) |

| | | | | | | |
|---|---|---|---|---|---|---|
| (Boito and Grena 2016) | LFR | Plant cost per collected radiation | Mirror width, focal length and spacing | Geometrical optical, cost | Matlab | Broyden–Fletcher–Goldfarb–Shanno (BFGS), Simulated Annealing |
| (Moghimi, Craig, and Meyer 2015) | LFR | Receiver heat loss, wind area of the receiver | Geometrical parameters of the receiver | CFD thermal | ANSYS: Fluent, DesignXplorer | Kriging, MOGA |
| (Farges, Bézian, and El Hafi 2018) | PT | Heliostat field optical efficiency, energy collected | Heliostat width and height, receiver width height and tilt angle, tower height | MCRT based optical model | EDStar | PSO |
| (Besarati, Goswami, and Stefanakos 2014) | PT | Yearly insolation weighted efficiency | Two parameters needed to define the prophylaxis layout pattern | Analytical optical | Matlab | GA |
| (Gallego and Camacho 2018) | PT | Receiver energy collection, flux peaks | Coordinates of the aiming points for heliostats | Analytical optical | Matlab | GA |
| (Saghafifar, Gadalla, and Mohammadi 2019) | PT | Annual weighted efficiency, LCOE | Eight variables to define the non- | Analytical optical | Matlab | GA |

| | | | | | | |
|---|---|---|---|---|---|---|
| | | | equal heliostat layout | | | |
| (Wang, Duan, and Yang 2018) | PT | Instantaneous Optical Efficiency | spacing between consecutive rows, heliostat pedestal height | Analytical optical | Visual Studio Community 2015 | GA |
| (Collado and Guallar 2016) | PT | Levelised cost of Energy, heliostat energy collection | Tower optical height, receiver radius | Cost model, geometric model | SAM | Parametric |
| (Boukelia, Arslan, and Mecibah 2016) | PTC | LCOE | Solar multiple, design solar radiation, ambient temperature, collector spacing, hours of storage | Energy simulation for the entire plant, Cost model | EBSILON, SAM, Matlab | ANN used on a set of pre-designs |
| (Guo and Huai 2016) | PTC | Exergy efficiency, Thermal efficiency | Temperatures of working fluid and receiver wall, mass flow rate | Thermal model for the receiver | NA | GA |
| (Tsai 2016) | PTC | Irradiance ratio | Collector geometrical parameters | Optical model | ZEMAX, SolidWorks-Flow simulations | Exhaustive |

| | | | | | | |
|---|---|---|---|---|---|---|
| (Yan, Peng, and Cheng 2018) | SPD | Flux non-uniformity factor | Element rotation angle | Optical simulation | C++ | GA |
| (Glynn John and Lakshmanan 2017) | SPD | Cost, Power, Efficiency | Geometrical parameters of the Dish | Cost model | - | Graphical |
| (Ahmadi et al. 2013) | SPD | thermo-economic function, thermal efficiency, power output | temperature ratio, irreversibility factor, heat source temperature, hot working fluid temperature, ratio of heat transfer areas | Thermo-economic model | Matlab | Non-dominated Sorting GA - (NSGA- II ) |

Based on Table 2.1, the following points can be highlighted:

- GA has been largely used in the optical optimization of PT systems. In addition to this, exhaustive search has also been considerably used in CSP design for cases where the search space is rather small. There is also a trend to develop and apply in-house PSO algorithms in recent years.
- General-purpose programming languages such as FORTRAN and C++ have been used with PSO and GA optimization methods. However, Matlab has been the main computing environment used in all CSP optimization studies. Starting from a straightforward brute force (or exhaustive search) approach, it has been used to implement several optimization methods such as GA and ANN.
- In PT systems, the norm is to use pre-developed analytical optical codes to conduct heliostat layout optimization. However, in LFR systems MCRT based in-house optical models are used for mirror field optimization. Almost all of the studies are limited to optical simulations without taking thermal aspects into account and a fixed tower/receiver height.
- LFR design optimization has been based on optical analysis alone without sufficient emphasis on thermal aspects.
- Most of the LFR optical optimization studies address the mirror field alone considering three common design variables: mirror width, spacing and focal length. Studies that combine the mirror field and receiver design together are rare. Receiver design variables such as receiver height and diameter have not been sufficiently addressed.

## 2.10 Research gap addressed in this thesis

A comprehensive LFR design optimization must deal with both optical and thermal performance simultaneously as solar energy gains and heat losses are equally important to obtain the power output and cost of energy. Although similar research is rare, this concept has been shown in some research such as Roostaee and Ameri (2019), where the dynamic connection of receiver dimensions and its heat loss to the mirror field design is demonstrated. Furthermore, addressing both optical and thermal design results in a more accurate cost of energy or electricity analysis. Few researchers tried to develop an

accurate cost of energy analysis (Boito and Grena 2016; Moghimi, Craig, and Meyer 2017) or a detailed energy model (Roostaee and Ameri 2019) have highlighted two common directions, which need further work (see section 2.6 for more detail).

- Include both receiver and mirror field parameters as design variables to be optimized
- Develop dynamically linked(coupled) comprehensive optical and thermal models

Due to the complexity involved, the aforementioned research gap has not yet been sufficiently addressed in an existing LFR design optimization study. Based on the literature, the following two aspects become important while addressing this research gap.

- Employing a suitable optimization technique to overcome the complexity that arises from: coupled optical and thermal modelling; receiver design variables added in addition to the mirror field variables
- Establishing a framework where: different mirror configurations and receiver designs can be optimized; different optimization methods and optical simulation tools can be employed

## 2.11 Summary

This chapter provided an up-to-date literature review on CSP optimization. Initially the design evolution of LFR systems, from early research to modern designs, was discussed. The common LFR configurations and receiver types were identified. Literature on optical and thermal optimization of LFRs was discussed in detail along with economic modelling. LFR design variables and parameters used in other studies were identified. Furthermore, a review of CSP systems showed that, optimization efforts in PT and LFR systems were significantly higher than in the other two common technologies, PTC and SPD. In PT systems, the norm was to use pre-developed analytical optical codes to conduct heliostat layout optimization. In LFR systems, MCRT-based in-house optical models were used for mirror field optimization. Almost all of the studies were limited to optical simulations without taking thermal aspects into account. Although, there was a significant difference

between modelling approaches, both PTs and LFRs shared common optimization methods and platforms. The research gap identified through the review was presented explicitly at the end of this chapter. Different LFR configurations, design variables and parameters, modelling approaches, optimization methods and platforms identified are used in Chapter 3 to develop the Methodology.

# 3

# Methodology

The research methods used to achieve this study's aim, objectives and research questions are discussed in this chapter. Initially, the analytical and numerical modelling approach followed in this study is explained. The selection of design variables and configurations for the rest of the study is then clarified. Details of optical and thermal modelling with the main assumptions used, model verifications and coupling of the models with an optimization algorithm are described next. The use of the developed framework to test alternative optimization methods to select the best performing optimization methods is explained subsequently. Different scenarios selected based on the research questions are presented for two objective functions (total theoretical efficiency and LCOE) and five design variables (number of mirrors; mirror width and spacing; receiver height and temperature). The methods of evaluating the results are finally described.

## 3.1 Modelling approach and defining the scope of this research

There are two distinct methods to conduct a theoretical analysis of an LFR system, namely an analytical approach and a mixed approach, which is a combination of analytical and numerical methods. Early research used analytical approaches for initial investigations and identifying concentration characteristics of basic LFR designs. However, the analytical approach is only suitable to analyse a few primary parameters assuming ideal conditions and, in practice, becomes challenging to use it for complicated designs. Alternatively, numerical approaches such as CFD are focused on a high level of detail on one aspect such as thermal performance and are reported to be computationally intensive. Therefore, based on the level of complexity of the problem to be addressed, a mixed approach of analytical and numerical methods is applied in this research. As the

starting point of the research, an LFR system is mathematically modelled to analyse the optical and thermal behaviours of alternative designs.

The research goes on to select several critical design variables, parameters and configurations, as identified in the literature review chapter. A schematic diagram of the selected LFR configuration based on common industrial designs and other studies is shown in Figure 3.1. The LFR system shown, employing eight mirror rows and a receiver on top, is just one design choice that falls under the selected configuration. The receiver types selected for this study were a trapezoidal cavity receiver and a single tube receiver with a secondary concentrator, as outlined in Chapter 2.2. Based on the outcome of Chapter 2, the main design variables needed to fully define the LFR mirror field were the number of mirrors, mirror width and mirror spacing. In the case of curved primary mirrors, focal length has been reported as another design variable. However, in order to evaluate the effects of mirror curvatures in detail, three mirror curvature types are investigated (flat, slightly curved and fully curved) (Bernhard et al. 2008; Mills 2012; Qiu et al. 2015) as different scenarios in this study. Unlike previous research on LFR design, the coupled optical and thermal modelling approach used in this thesis enables receiver temperature to also be considered as a design variable. The other receiver related variables are receiver height and width/diameter. In the case of a standard industrial receiver design, the receiver width/diameter is fixed. More detailed descriptions of design variables are found in Chapters 4.4 and 5.3.

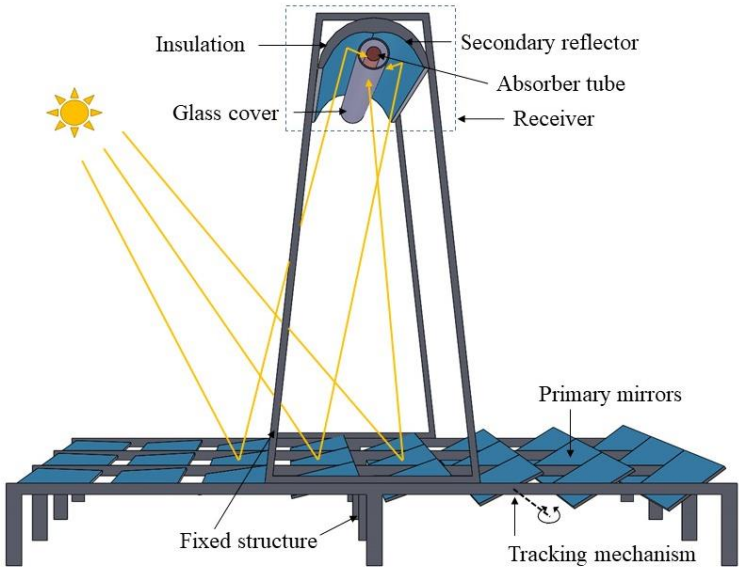


Figure 3.1: Schematic diagram of a typical LFR configuration studied in this work

## 3.2 Optical modelling

Although analytical approaches and developing in-house codes for Monte Carlo Ray Tracing (MCRT) are possible, optical modelling is carried out in this work using SolTrace. Being a specially designed tool for CSP optical design, SolTrace enables optical modelling with high accuracy and detail, such as non-parallel solar rays, multiple reflections and directional dependant surface optical properties. Furthermore, it enables the modelling of an optically challenging receiver such as a CPC and evacuated tube. Developed by National Renewable Energy Laboratory (NREL) (Wendelin, Dobos, and Lewandowski 2013), SolTrace has become an established MCRT tool for modelling CSP systems (Zhu 2013; Montes et al. 2014; Qiu et al. 2015). The optical model for an LFR developed in SolTrace is then verified against other results found in the literature.

## 3.3 Thermal modelling

Thermal models are developed using analytical equations and empirical correlations. The energy output of the LFR system is modelled under steady state conditions using heat transfer theory and adopting relevant sub-models from the literature. The energy output and potential power generation of the system depend on the receiver operating temperature. Unlike other geometrical variables, the operating temperature is controlled

by the solar irradiance, and receiver flow parameters such as mass flow rate and inlet fluid temperature. Having fluid flow parameters in the modelling equations drastically increases the computational time in the optimization stage. Therefore, a uniform temperature boundary condition is assumed at the absorber tube to avoid additional complexity. This boundary condition has previously been used successfully by Sahoo, Singh, and Banerjee (2012) and Moghimi, Craig, and Meyer (2015) to decouple the effects of the flow parameters on thermal performance. Furthermore, the potential power output of an LFR system is obtained using the uniform absorber temperature combined with the Carnot cycle as done in other LFR studies(Romero, Gonzalez-Aguilar, and Zarza 2015; Abbas et al. 2016; Nixon and Davies 2012). This simple approach results in temperature-dependant power output calculations without overstraining optimization models with two-phase flows and additional parameters. To evaluate the effects of the temperature variation on the performance at different operational hours, two receiver temperature operating conditions, constant and variable, are considered. In the first operating condition, a single constant receiver temperature is maintained in the system. In the second operating condition, the receiver temperature is allowed to change, but maintained below a maximum limit (e.g. 400°C). The thermal models developed are verified against experimental and other simulation results reported. Power output and energy costs of selected designs are finally calculated based on the ideal steam Rankine cycle and annual solar irradiance data to get a detailed performance evaluation of LFR systems under the operating parameters of existing power plants.

## 3.4 LFR optimization framework

A framework that enables linking an optimization method to the coupled optical and thermal models is developed to allow different optimization methods to be applied and tested. There are four main elements needed to formulate an optimization problem, namely, objective function, design variables (a.k.a. decision variables), variables' bounds and constraints. To evaluate performance and cost based designs, two objective functions are investigated: total theoretical efficiency and Levelized Cost of Electricity (LCOE). The total theoretical efficiency provides the maximum limit of power generation based on the Carnot principle (Romero, Gonzalez-Aguilar, and Zarza 2015; Abbas et al. 2016). LCOE is a common techno-economic indicator used to evaluate the energy costs of CSP systems

(Boukelia, Arslan, and Mecibah 2016; Saghafifar, Gadalla, and Mohammadi 2019). All variables identified as critical for the design are considered in this work when seeking an optimal design. In a practical scenario, the bounds are selected to cover the entire range of design variables reported in the literature. Furthermore, the ranges of the bounds are further extended beyond their reported values to avoid artificially over-constraining the design space. Constraints are identified based on the mathematical models, practical and cost limitations. A detailed description of the optimization problem formulation is found in Chapter 5.3.

Once the optimization problem is formulated, a suitable optimization method is used to solve the problem. The selection of a suitable optimization method depends on several factors. Firstly, it can depend on several mathematical qualities of variables such as dimensionality, uncertainty, being independent or dependent, and continuous or discrete. Secondly, the selection is based on the objective function, which can be the most common method of selection (e.g. single or multi-objective objective optimization problem). Furthermore, the nature of the objective function such as convex, non-convex, simulation-based and surrogate-based leads to several optimization methods. Thirdly, the selection is based on the nature of the constraints. The nature of the current optimization problem can be described as in Table 3.1 based on all selection methods described.

Table 3.1: Describing the optimization problem in this research

| | |
|---|---|
| Variables | multi-dimensional; mutually independent; static(do not depend on other parameters such as time); deterministic(no uncertainty), both continuous and discrete |
| Objective function | simulation-based; non-convex; single objective |
| Constraints | constrained problem |

Having simulation-based objective functions and both discrete and continuous variables, the most direct approach to solve the current optimization problem is metaheuristics methods. However, as the selection of a suitable optimization algorithm can be problem dependent, common derivative-based and derivative-free methods were also tested in this study in addition to the metaheuristics methods.

## 3.5 Testing of alternative optimization methods and use of GA

To test and evaluate different optimization methods, one design variable (e.g. receiver height) is initially investigated (1D problem) for an LFR system with a trapezoidal receiver, while fixing the other design variables at constant values. An exhaustive search (brute force approach) is conducted to accurately identify the global optimum. Derivative-based (interior point, SQP and active set), derivative-free (pattern search and fminsearch), population based (GA) and simulated annealing optimization methods are then applied to see how close these approaches are to the global optimum. These methods are selected as they are frequently used for similar problems and are readily available in software platforms (For instance, fminsearch is a built-in function included in the Matlab optimization toolbox). Three best performing methods from this simulation are selected to be applied for a multi-dimensional problem with a trapezoidal receiver. The same approach of comparing the results of brute force and the selected methods is used to decide the best optimization method based on accuracy and computational time.

As an outcome of testing alternative optimization methods, one method is selected to be used in the rest of the research (GA has been selected as described in Chapter 5). A single-tube receiver with a CPC is considered at this stage, as it is the most established type in commercial and prototype LFR power plants (Montes et al. 2014; Islam et al. 2018). This receiver uses the SCHOTT PTR®70 (SCHOTT solar 2013), currently known as RIOGLASS PTR®70 (RIOGLASS Solar 2020), which is a common off-the-shelf component used in similar systems. The design of the CPC is taken from Chaitanya Prasad, Reddy, and Sundararajan (2017), which has been used in several other studies (Balaji, Reddy, and Sundararajan 2016; Bellos and Tzivanidis 2018a). A detailed parameter setting, which provides the best convergence for the selected method, is identified by evaluating a large number of simulations as suggested in the literature. Moreover, the confidence level of the variability of the global solution found is statistically established.

## 3.6 Evaluation of different optimization scenarios

The optimization framework developed is used to answer the research questions 2 and 3 defined in Chapter 1 (research question 1 is related to developing the framework itself). Two objective functions (total theoretical efficiency and LCOE) and five design variables

(number of mirrors; mirror width and spacing; receiver height and temperature) are used for this purpose. The dimensions of the receiver are fixed at this stage based on the industrial receiver design selected.

To answer the research questions, three different case study locations are used: Spain, China and Australia. These locations are selected based on well-known and latest industrial developments, and differences in latitudes for LCOE optimization. To represent the annual variation of the solar radiation profile, measured weather data for four days (Li, C. et al. 2018; Xie et al. 2021) are taken from the TMY dataset. However, a generic solar radiation profile on the transverse plane is considered (Sánchez, Clifford, and Nixon 2018; Roostaee and Ameri 2019) for the performance based objective function. This would have little impact on the comparisons between the scenarios modelled and significantly saves the computational time in the optimization. Detailed simulations considering 365 days of TMY data are finally conducted on the optimized systems.

Different scenarios are optimized based on the two objective functions to answer the research questions. Nine scenarios are investigated for the total theoretical efficiency consisting of: flat, slightly curved and fully curved primary mirror types; constant and variable temperature operating conditions with two maximum temperature limits. Three scenarios are examined for LCOE consisting of the three locations. Furthermore, the consequences of installing an LFR design in a certain location, which has been optimized for a different location are investigated.

All the scenarios are compared in terms of optimized results: values of design variables and relevant objective functions. For instance, different mirror types are compared in terms of total theoretical efficiency and design variables to identify potential improvements. Similarly, the best receiver temperature operating condition and optimum temperatures to maximise the efficiency are identified. Location-specific optimization results are compared to identify the LCOE and design changes. Furthermore, the sensitivity of the optimal designs to potential changes in costs and design variables is examined. Results of other optical optimization studies and data on existing LFR systems are compared to identify the similarity/dissimilarity between the designs. Potential LCOE and design improvements with respect to commercial designs are finally proposed using this study.

# 4

# Modelling of Linear Fresnel Reflector (LFR) systems

## 4.1 Introduction

In this chapter, modelling the energy output of Linear Fresnel Reflector (LFR) systems is discussed in detail and optical, thermal and cost models are outlined. The optical modelling of an LFR is initially discussed along with how ray tracing can be used to conduct an optical analysis. Thermal modelling of different LFR receiver types is then discussed with relevant modelling equations. A cost model is presented to be used for the cost of energy evaluations. Optical and thermal models are finally verified using experimental studies, existing LFR systems and other modelling studies.

## 4.2 Energy output of an LFR system

Conservation of energy is one of the main governing laws of any thermodynamic system. Therefore, modelling an LFR needs to consider the energy balance at the receiver, where solar energy is collected and transferred to a working fluid. Based on this principle, the energy output of the system ($Q_o$) (often referred to as the useful heat gain), can be found from the difference between the heat input ($Q_{in}$) to the receiver and heat loss to ambient air ($Q_{loss}$) (Morin et al. 2012).

$$Q_o = Q_{in} - Q_{loss} \tag{4.1}$$

After reflection by the mirrors, solar energy incident over the receiver area ($A_r$) is absorbed as heat and transferred to the working fluid. This becomes the heat input ($Q_{in}$) to the system. As a consequence of absorbing heat and increasing the receiver

temperature ($T_r$) compared to the surrounding temperature ($T_a$), a portion of absorbed energy is lost to the surrounding. The heat output of an LFR system can therefore be described by (Duffie and Beckman 2013; Zheng 2017),

$$Q_o = I_{r,abs} A_r - A_r U_L (T_r - T_a) \tag{4.2}$$

where $I_{r,abs}$, $U_L$, $T_r$ and $T_a$ are intensity of absorbed solar radiation, heat loss coefficient of the receiver, receiver temperature and ambient temperature, respectively. A uniform absorber temperature is assumed here as used by Sahoo, Singh, and Banerjee (2012) and Moghimi, Craig, and Meyer (2015). It is important to note that equation (4.2) is applied to the heat absorbing element, although the word "receiver" is commonly used.

Only a part of the solar radiation received on LFR mirrors is reflected and absorbed by the receiver. This fraction is given by the optical efficiency ($\eta_o$) which is defined as the ratio between the total solar power received on full primary mirror aperture area to the power absorbed by the receiver (Kincaid et al. 2018). For a mirror field with *n* number of mirrors, considering Direct Normal Irradiance *(DNI)* receiving on the $i^{th}$ mirror at an incident angle of $\theta_i$,

$$\eta_o = \frac{I_{r,abs} A_r}{\sum_{i=1}^{i=n} DNI\ A_{m,i} \cos \theta_i} \tag{4.3}$$

Combining equations (4.2) and (4.3),

$$Q_o = \eta_o \sum_{i=1}^{i=n} DNI\ A_{m,i} \cos \theta_i - A_r U_L (T_r - T_a) \tag{4.4}$$

According to equations (4.3) and (4.4), analysing the energy output of an LFR system requires optical and thermal models to calculate the solar energy absorbed by the receiver and heat loss coefficient ($U_L$) respectively. Optical and thermal analyses are described in sections 4.3-4.7.

## 4.3 Use of Incident Angle Modifier (IAM) for energy analysis

Inspired by PTC technology, it is conventional to express optical efficiency in terms of the Incident Angle Modifier (IAM). This is a convenient way to consider both transversal and longitudinal directions, especially to calculate annual energy output. Figure 4.1 provides a schematic of an LFR system showing transverse and longitudinal planes.

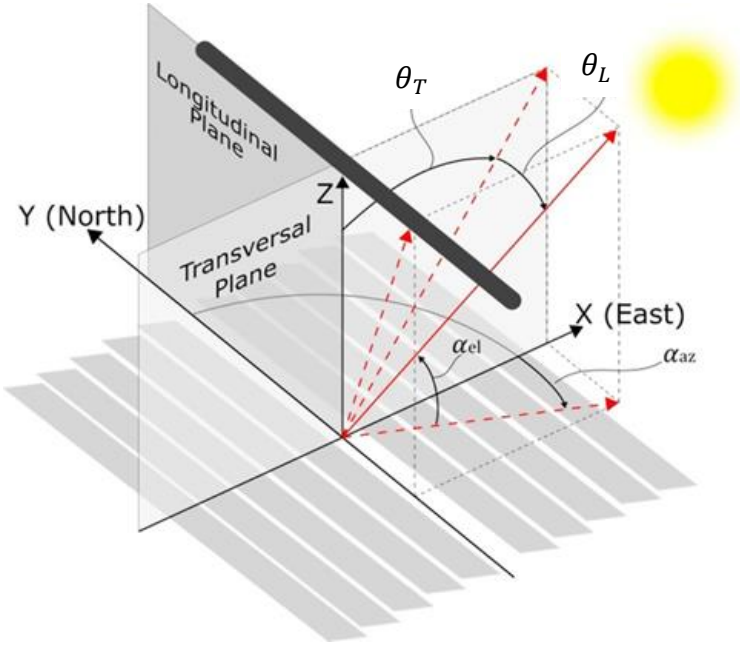


Figure 4.1: LFR system showing transverse and longitudinal planes; Reprinted from Kincaid et al. (2018), Copyright (2018), with permission from Elsevier

Optical efficiency ($\eta_o$), defined in equation (4.3) is a function of the transverse angle ($\theta_T$) and longitudinal angle ($\theta_L$).

$$\eta_o = \eta_o(\theta_T, \theta_L) \tag{4.5}$$

Optical efficiency can be expressed in terms of IAM as in equation (4.6). Equation (4.7) provides an accurate approximation to calculate the IAM based on separate calculations on the transversal and longitudinal planes (McIntire 1982; Bellos and Tzivanidis 2018b; Kincaid et al. 2018). IAM is taken as $K(\theta_T, \theta_L)$ hereafter as used in McIntire (1982).

$$\eta_o(\theta_T, \theta_L) = K(\theta_T, \theta_L)\, \eta_{o,max} \tag{4.6}$$

$$K(\theta_T, \theta_L) \approx K_T(\theta_T) K_L(\theta_L) \tag{4.7}$$

where,

$$K_L(\theta_L) = \frac{\eta_o(\theta_T = 0, \theta_L)}{\eta_{o,max}} \tag{4.8}$$

$$K_T(\theta_T) = \frac{\eta_o(\theta_T, \theta_L = 0)}{\eta_{o,max}} \tag{4.9}$$

Bellos and Tzivanidis (2018) suggested an analytical equation to calculate $K_L(\theta_L)$ as,

$$K_L(\theta_L) = \cos\theta_L - \frac{h_r}{L}\sqrt{1 + \left(\frac{W}{4h_r}\right)^2}\ \sin\theta_L \tag{4.10}$$

where, $h_r$, $W$ and $L$ are receiver height, plant width and length, respectively. However, the length of a large pilot or commercial LFR plant can typically be up to 1000 m with a receiver height less than 10 m. Furthermore, plant width can normally be a few times as much as the receiver height. Therefore, the second term of the equation (4.10) is negligible compared to the values of $\cos\theta_L$. This gives,

$$K_L(\theta_L) \approx \cos\theta_L \tag{4.11}$$

Combining equations (4.6) to (4.11) as,

$$\eta_o(\theta_T, \theta_L) \approx \frac{\eta_o(\theta_T, \theta_L = 0)}{\eta_{o,max}}\ \cos\theta_L\ \eta_{o,max} \tag{4.12}$$

Further simplifying the equation (4.12) to get the optical efficiency,

$$\eta_o(\theta_T, \theta_L) \approx \eta_o(\theta_T, \theta_L = 0)\cos\theta_L \tag{4.13}$$

Rearranging equation (4.4) by combining equations (4.5) and (4.13), to get the heat output considering both transverse and longitudinal directions.

$$Q_o \approx \eta_o(\theta_T, \theta_L = 0\ ) \cos \theta_L\ DNI\ A_{ap} - A_r U_L (T_r - T_a) \tag{4.14}$$

Equation (4.14) enables calculating the energy output of the LFR system for both daily and annual variation of solar irradiance in various locations. This equation can be conveniently used to obtain the annual energy output for the cost of energy calculations.

## 4.4 Design variables and configurations modelled

Figure 4.2 shows a 2D schematic diagram of a ray of light hitting a mirror and being reflected to an evacuated tube receiver. All the rays reflected from the mirrors are focussed on the centreline of the receiver tube or the receiver tube plane for a trapezoidal receiver. The transverse angle ($\theta_T$) changes with the direction of solar rays coming to the system and depending on the collector's location, specific day of the year and time of the day. The number of rays hitting the receiver also varies with changes in the design variables: number of mirrors ($n_m$), mirror width ($w_m$), mirror spacing ($s_m$) and receiver height ($h_r$) and mirror focal length ($f_m$). Receiver design variables related to a single tube and trapezoidal receivers are absorber diameter ($D_r$) and receiver width ($w_r$), respectively. Receiver temperature ($T_r$) introduced in section 4.2 is the non-geometrical design variable considered in this study.

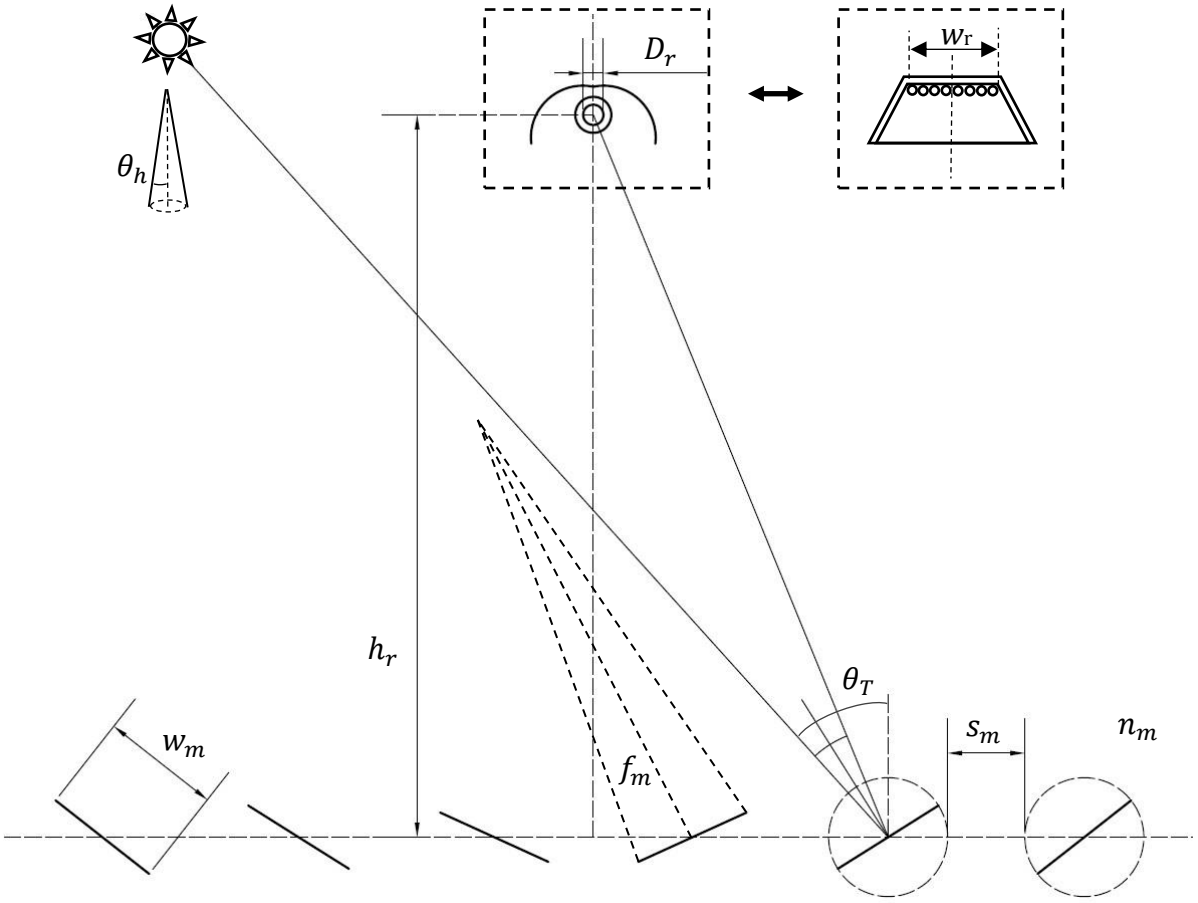


Figure 4.2: Schematic of a 2D view of an LFR plant indicating main geometrical parameters considered for optical simulation

## 4.5 Optical modelling

### 4.5.1 Optical parameters of an LFR system

The optical performance of an LFR determines the input power to the collector and is important for performance optimization and safe operation. Many studies on LFR and PT systems have focused on this topic, as discussed in Chapter 2. The optical analysis is an integral step in the design and analysis for optimum operation even in more conventional PTCs (Yang, Sensoy, and Ordonez 2018). However, optical analysis of an LFR is relatively more complex compared to PTCs, demanding more computational time due to the higher number of mirrors, a secondary reflector, structural shadowing and adjacent mirror rows blocking each other (Cheng et al. 2018).

For CPS applications, the sun cannot be considered a point source but a sphere of a specific radius (Kalogirou 2009). Therefore, it creates a certain angle as seen from the earth. One-half of this angle is known as half acceptance angle ($\theta_h$) which is normally taken as 4.65 mrad (≈0.27°). This effect is frequently approximated as circular Gaussian distribution. Based on measurements made by Grether and Hunt, a Gaussian distribution with standard deviation($\sigma_{sun}$), also known as root mean squared (RMS) width, of 2.73 mrad is typically used to represent the sun (Landman 2017) and used in this study.

The optical properties of mirror and absorber elements play a critical role in CSP systems. Surface optical properties, reflectivity, absorptivity and transmissivity, show directional and spectral dependence. As solar rays reach the mirror and absorber surfaces at different angles, different corresponding optical properties have to be considered for accurate analysis. Directional dependence of receiver solar absorptivity and solar reflectivity of primary mirrors have been experimentally identified by Tesfamichael and Wäckelgård (2000) and Sutter et al. (2018), respectively (Figure 4.3 and Figure 4.4). These values have been used in the optical model for different incident angles varying from 0° to 90°. The transmissivity of all the mirrors is taken as zero as they are non-transparent. In addition to this, typical values of transmissivity and refractive index for the glass tubes are taken as 0.97 and 1.5, respectively.

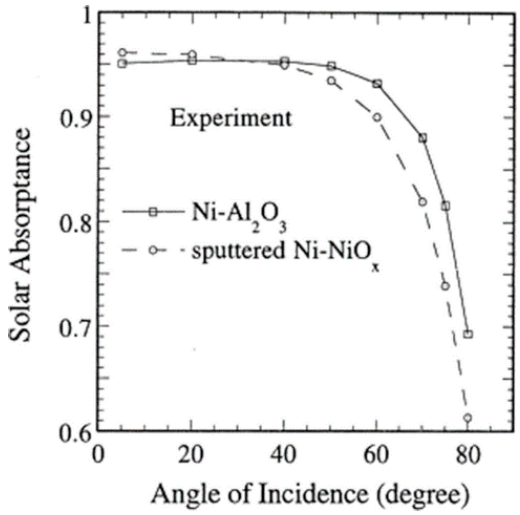


Figure 4.3: Solar absorptivity vs incident angle for receiver material; Reprinted from Tesfamichael and Wäckelgård (2000), Copyright (2000), with permission from Elsevier

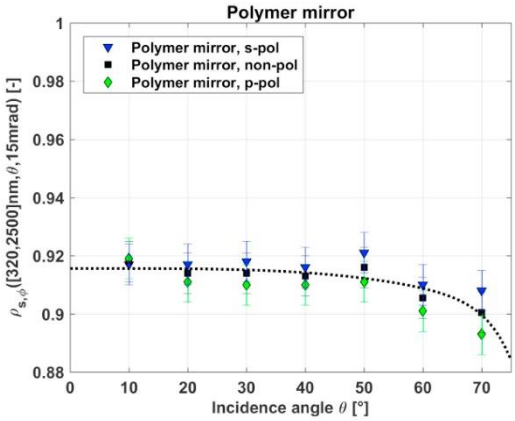


Figure 4.4: Solar reflectivity vs incident angle for primary mirrors; Reprinted from Sutter et al. (2018), Copyright (2018), with permission from Elsevier

Optical losses in CSP systems occur for several reasons. Common causes are surface irregularities, structural factors, limitations of tracking mechanism, dust and ageing. Dust and ageing effects are not addressed in this work. All other aforementioned factors are typically categorised under optical errors. Surface irregularities at macro and micro levels are referred to as slope error and specularity error, respectively. The total optical error ($\sigma_{total}$) can be modelled using a Gaussian distribution, as in equations (4.15) and (4.16) (Kincaid et al. 2019). In this work, a total collector optical error ($\sigma_{collector,error}$) of 5 mrad is used based on the work of Chemisana et al. (2013), Zhu (2013) and Montes et al. (2014) to account for slope error ($\sigma_{slope}$), specularity error ($\sigma_{specularity}$) and tracking error ($\sigma_{track}$) of primary mirrors, and equivalent receiver error ($\sigma_{rec}$).

$$\sigma_{total}^2 = \sigma_{sun}^2 + \sigma_{collector,error}^2 \tag{4.15}$$

$$\sigma_{collector,error} = \sqrt{\sigma_{specularity}^2 + \left(2\sigma_{slope}\right)^2 + (2\sigma_{track})^2 + (\sigma_{rec})^2} \tag{4.16}$$

### 4.5.2 Automation of optical modelling using SolTrace

Monte Carlo Ray Tracing (MCRT) is often used to simulate the sunrays hitting a solar reflector and absorber surface to model optical performance (see Table 2.1 in Chapter 2). However, implementing the MCRT technique can often be challenging to designers since

it requires prior knowledge in ray tracing and computer programming. Furthermore, a comprehensive code can demand a high computational time in the modelling stage alone causing major computational challenges in the optimization stage. Alternatively, there are several ray tracing packages available to designers, such as SolTrace, Optica and Tonatiuh. These ray tracing tools are frequently used to validate in-house codes developed by researchers. SolTrace is the most widely used ray tracing tool for CSP design, which has been proven to provide accurate optical analyses for a variety of applications (Zhu 2013; Moghimi, Craig, and Meyer 2015; Qiu et al. 2015). This tool has been developed by the National Renewable Energy Laboratory (NREL) in the USA and is freely available (Wendelin, Dobos, and Lewandowski 2013). Therefore, SolTrace is selected as the tool to analyse the optical performance of LFR systems.

Although SolTrace has been widely used by the research community, validated and freely available, there are several limitations associated with this tool. There is the lack of documentation and support, except for basic help files. A 3D model of mirror elements appears only when the ray tracing is successfully completed. Therefore, it can be difficult to identify modelling errors made at intermediate steps. Figure 4.5 shows the SolTrace interface with the specification of mirror elements, shown in different rows and columns. A typical modelling approach, supported by the user interface, is to manually enter the values of each cell to define the mirror element coordinates, aperture and surface area, curvature specifications and optical interactions. Furthermore, solar profile, optical properties of mirror elements and ray tracing options have to be defined at the relevant stages. All these manual modelling steps in SolTrace have to be replaced by automated steps in order to enable any form of optimization. As SolTrace supports the LK scripting language, automation of the entire optical modelling process was carried out using LK scripting in this study. LK is a powerful scripting language that is designed to be small, fast, and easily embedded in other applications. An LK language guide provided by Dobos (2017) was used as a reference to develop the LK scripting. Furthermore, each SolTrace simulation requires a large number of coordinates (shown in Figure 4.5) to generate an LFR system in 3D space and these coordinate data were generated using a separate geometrical model (see Appendix A for a sample Matlab code developed).

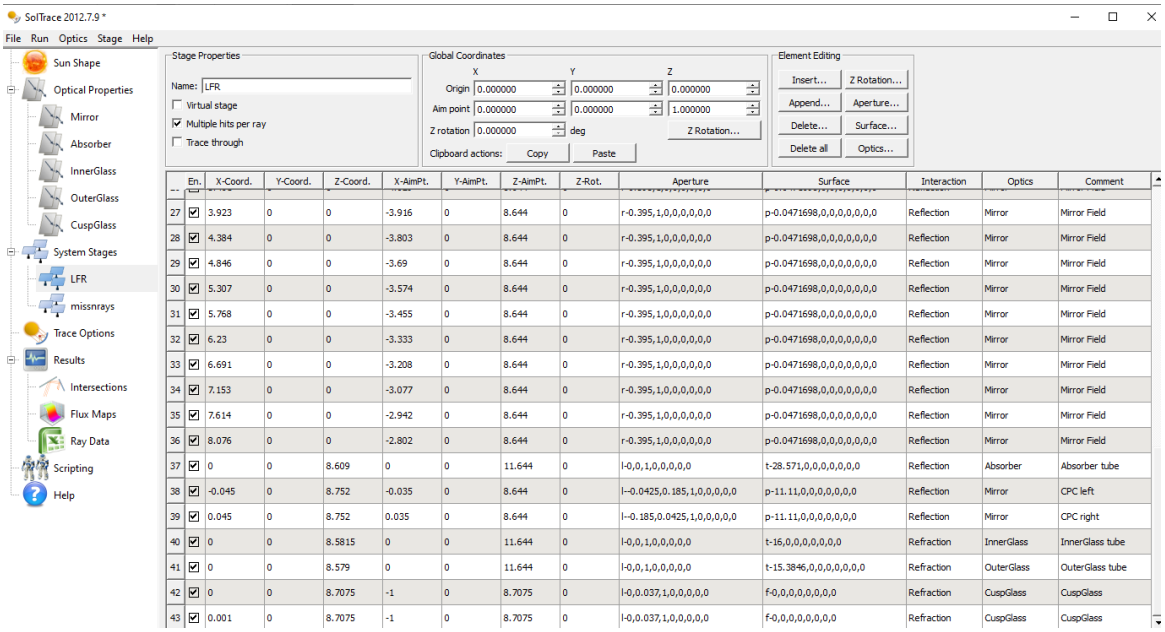


| | En. | X-Coord. | Y-Coord. | Z-Coord. | X-AimPt. | Y-AimPt. | Z-AimPt. | Z-Rot. | Aperture | Surface | Interaction | Optics | Comment |
|---|---|---|---|---|---|---|---|---|---|---|---|---|---|
| 27 | ☑ | 3.923 | 0 | 0 | -3.916 | 0 | 8.644 | 0 | r-0.395,1,0,0,0,0,0,0 | p-0.0471698,0,0,0,0,0,0,0 | Reflection | Mirror | Mirror Field |
| 28 | ☑ | 4.384 | 0 | 0 | -3.803 | 0 | 8.644 | 0 | r-0.395,1,0,0,0,0,0,0 | p-0.0471698,0,0,0,0,0,0,0 | Reflection | Mirror | Mirror Field |
| 29 | ☑ | 4.846 | 0 | 0 | -3.69 | 0 | 8.644 | 0 | r-0.395,1,0,0,0,0,0,0 | p-0.0471698,0,0,0,0,0,0,0 | Reflection | Mirror | Mirror Field |
| 30 | ☑ | 5.307 | 0 | 0 | -3.574 | 0 | 8.644 | 0 | r-0.395,1,0,0,0,0,0,0 | p-0.0471698,0,0,0,0,0,0,0 | Reflection | Mirror | Mirror Field |
| 31 | ☑ | 5.768 | 0 | 0 | -3.455 | 0 | 8.644 | 0 | r-0.395,1,0,0,0,0,0,0 | p-0.0471698,0,0,0,0,0,0,0 | Reflection | Mirror | Mirror Field |
| 32 | ☑ | 6.23 | 0 | 0 | -3.333 | 0 | 8.644 | 0 | r-0.395,1,0,0,0,0,0,0 | p-0.0471698,0,0,0,0,0,0,0 | Reflection | Mirror | Mirror Field |
| 33 | ☑ | 6.691 | 0 | 0 | -3.208 | 0 | 8.644 | 0 | r-0.395,1,0,0,0,0,0,0 | p-0.0471698,0,0,0,0,0,0,0 | Reflection | Mirror | Mirror Field |
| 34 | ☑ | 7.153 | 0 | 0 | -3.077 | 0 | 8.644 | 0 | r-0.395,1,0,0,0,0,0,0 | p-0.0471698,0,0,0,0,0,0,0 | Reflection | Mirror | Mirror Field |
| 35 | ☑ | 7.614 | 0 | 0 | -2.942 | 0 | 8.644 | 0 | r-0.395,1,0,0,0,0,0,0 | p-0.0471698,0,0,0,0,0,0,0 | Reflection | Mirror | Mirror Field |
| 36 | ☑ | 8.076 | 0 | 0 | -2.802 | 0 | 8.644 | 0 | r-0.395,1,0,0,0,0,0,0 | p-0.0471698,0,0,0,0,0,0,0 | Reflection | Mirror | Mirror Field |
| 37 | ☑ | 0 | 0 | 8.609 | 0 | 0 | 11.644 | 0 | l-0,0,1,0,0,0,0,0 | t-28.571,0,0,0,0,0,0,0 | Reflection | Absorber | Absorber tube |
| 38 | ☑ | -0.045 | 0 | 8.752 | -0.035 | 0 | 8.644 | 0 | l--0.0425,0.185,1,0,0,0,0,0 | p-11.11,0,0,0,0,0,0,0 | Reflection | Mirror | CPC left |
| 39 | ☑ | 0.045 | 0 | 8.752 | 0.035 | 0 | 8.644 | 0 | l--0.185,0.0425,1,0,0,0,0,0 | p-11.11,0,0,0,0,0,0,0 | Reflection | Mirror | CPC right |
| 40 | ☑ | 0 | 0 | 8.5815 | 0 | 0 | 11.644 | 0 | l-0,0,1,0,0,0,0,0 | t-16,0,0,0,0,0,0,0 | Refraction | InnerGlass | InnerGlass tube |
| 41 | ☑ | 0 | 0 | 8.579 | 0 | 0 | 11.644 | 0 | l-0,0,1,0,0,0,0,0 | t-15.3846,0,0,0,0,0,0,0 | Refraction | OuterGlass | OuterGlass tube |
| 42 | ☑ | 0 | 0 | 8.7075 | -1 | 0 | 8.7075 | 0 | l-0,0.037,1,0,0,0,0,0 | f-0,0,0,0,0,0,0,0 | Refraction | CuspGlass | CuspGlass |
| 43 | ☑ | 0.001 | 0 | 8.7075 | -1 | 0 | 8.7075 | 0 | l-0,0.037,1,0,0,0,0,0 | f-0,0,0,0,0,0,0,0 | Refraction | CuspGlass | CuspGlass |

Figure 4.5: SolTrace interface with each mirror element modelled

### 4.5.3 Setting up ray tracing parameters for different designs

In ray tracing, a large number of individual rays are generated and traced through the system. Each ray is subjected to different optical interactions depending on the geometry of the system and corresponding optical properties. A converged solution is achieved by producing a large number of rays. A large number of rays combined with complex geometries results in high processing times. The combined approach of probabilistic and deterministic ray interactions in the SolTrace code has proven its ability to solve even the most complex geometries at the expense of extra computational time. Kincaid et al. (2019) and Moghimi, Craig, and Meyer (2015) used one million rays to model LFR systems with similar complexity and Kincaid et al. (2019) obtained a convergence error lower than 0.1% for the aforementioned number of rays. Therefore, one million rays are used in this research.

Three primary mirror types, flat, slightly curved or fully curved, are considered in this work as mentioned in the methodology chapter. Slightly curved mirrors have a large focal length for all mirrors, which look flat to the naked eye (Figure 4.6). Furthermore, this slight curve can be achieved just by straining flat glass mirrors. Fully curved mirrors have an individual focal length for each mirror, focussed on the receiver. The approach used

here was to take the gap between the receiver tube centreline and mirror rotating axis as the focal length for each mirror row. In the case of all curved mirrors, parabolic geometries were used to model them in SolTrace. Qiu et al. (2015) showed that optimized cylindrical mirrors and parabolic mirrors provide nearly the same optical performance.

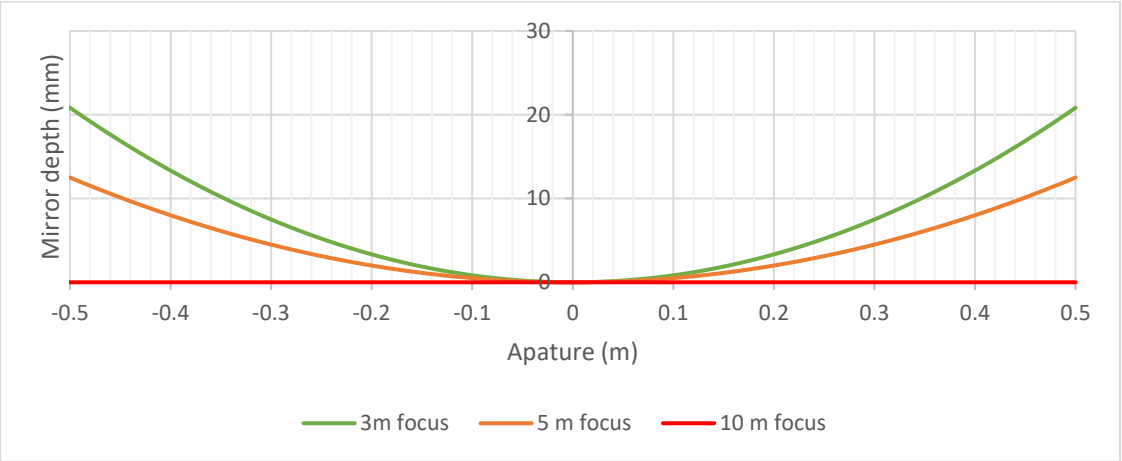


Figure 4.6: A comparison of different mirror depths of parabolic mirrors with a 1 m aperture

Figure 4.7 shows a snapshot of one of the SolTrace simulation runs using the aforementioned modelling method. Only 200 rays are shown here for clarity and an enlarged view of the receiver is shown in the figure to show the ray interaction in the absorber tube, cover glass and secondary reflector. Rays that end up missing the receiver tube target are shown in red.

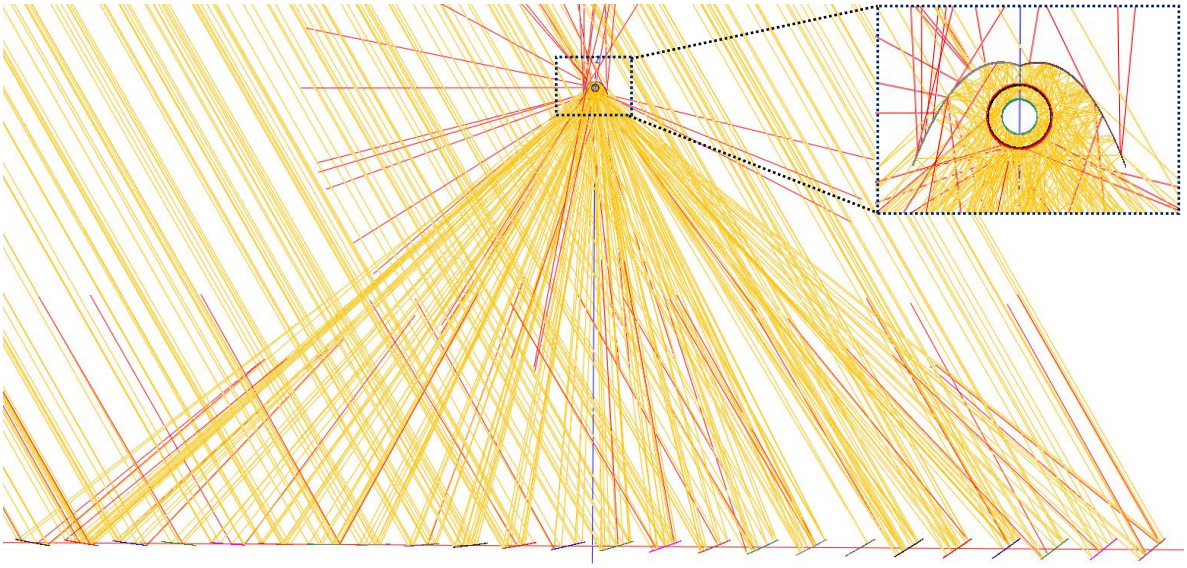

Figure 4.7: A snapshot from SolTrace showing one of the thousands of LFR designs simulated. Rays that do not hit the absorber tube are shown in red

## 4.6 Thermal modelling of a single tube receiver

Under thermal modelling, the receiver design installed most commonly is initially considered. Figure 4.8 shows the modes of heat transfer for a single tube receiver with an absorber tube surrounded by a glass cover.

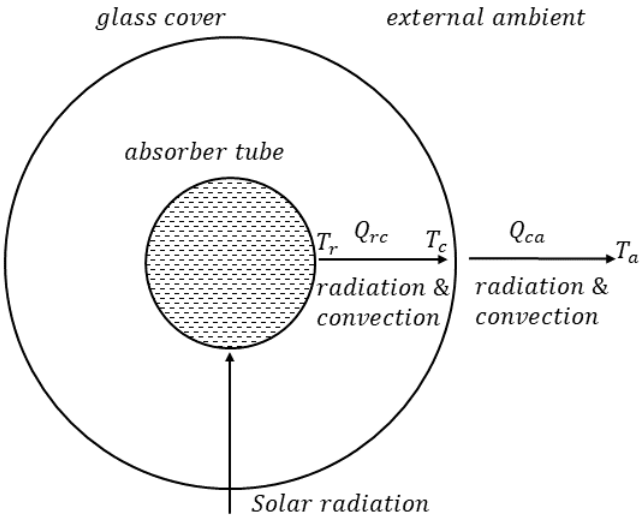


Figure 4.8: Different heat transfer modes and their components for a single tube receiver

The radiation heat exchange between the absorber tube and the glass cover ($Q_{rc,rad}$) is expressed as (Forristall 2003; Duffie and Beckman 2013),

$$Q_{rc,rad} = \frac{\pi D_r L \sigma (T_r^4 - T_c^4)}{\left(\frac{1}{\varepsilon_r} + \frac{(1-\varepsilon_r)}{\varepsilon_c}\left(\frac{D_r}{D_c}\right)\right)} \tag{4.17}$$

where $D$, $T$ and $\varepsilon$ are the diameter, temperature and emissivity with subscripts $r$ and $c$ denoting the receiver and glass cover, respectively. $L$ is the length of the receiver tube. Convective heat loss in the absorber tube ($Q_{rc,conv}$) can be expressed as (Forristall 2003),

$$Q_{rc,conv} = \pi D_r L \, h_{conv,rc}(T_r - T_c) \tag{4.18}$$

As proposed by Forristall (2003), the convective coefficient $h_{conv,rc}$ can be taken as $1.115 \times 10^{-4} \, W/m^2K$ for air at vacuum conditions (Cagnoli et al. 2018). However, convective heat loss in an evacuated receiver tube is assumed to be negligible in industrial applications (Industrial Solar GmbH 2021). Furthermore, a simple calculation would show that the convective component can be as low as 0.001% of the radiative component, owing to the extremely low convective heat transfer coefficient and high absorber temperature. Therefore $Q_{rc,conv}$ is assumed to be negligible in the calculations.

Radiative heat transfer of the glass cover with external ambient ($Q_{ca,rad}$) can be given as in equation (4.19). Duffie and Beckman (2013) assumed that the outer glass cover exchanges heat with the sky, which is at sky temperature ($T_{sky}$). This assumption is true for a glass cover that sees the bare sky without being covered by a secondary reflector such as CPC. In a design where a secondary reflector is used on the top and the glass cover never sees the sky, the radiative heat exchange occurs with the reflector and the surrounding which is not covered by the reflector. Therefore, it is more reasonable to assume these temperatures are closer to the ambient temperature ($T_a$) than $T_{sky}$. Cagnoli et al. (2018) used the same assumption in their work to replace $T_{sky}$ with $T_a$.

$$Q_{ca,rad} = \pi D_c L \varepsilon_c \sigma (T_c^4 - T_a^4) \tag{4.19}$$

Convective heat loss in the glass outer cover with external ambient ($Q_{ca,conv}$) can be expressed by,

$$Q_{ca,conv} = \pi D_c L\, h_{conv,ca}(T_c - T_a) \tag{4.20}$$

$$h_{conv,ca} = Nu_{D_c}\frac{k_a}{D_c} \tag{4.21}$$

where $h_{conv,ca}$, $Nu$ and $k_a$ refer to the convection coefficient of the external glass cover surface, Nusselt number and thermal conductivity of air, respectively.

Cagnoli et al. (2018) conducted a detailed CFD analysis on the thermal performance of an LFR receiver with a secondary concentrator, and concluded that wind effects on the receiver performance are negligible for an evacuated tube. They also mentioned that, the convective heat transfer condition between the glass cover and the external ambient does not affect the heat loss by the absorber tube. Therefore, the Nusselt number is calculated based on natural convection as in Incropera and DeWitt (2002) and Forristall (2003),

$$Nu_{D_c} = \left\{ 0.6 + \frac{0.387 {Ra_{D_c}}^{1/6}}{\left[1 + \left(\frac{0.559}{Pr_{ca}}\right)^{9/16}\right]^{8/27}} \right\}^2 \quad for\ Ra_{D_c} \leq 10^{12} \tag{4.22}$$

$$Ra_{D_c} = \frac{g\beta(T_c - T_a)\, D_c^3}{\nu^2}\, Pr_{ca} \tag{4.23}$$

where $g$, $Pr$ and $Ra$ are the gravitational acceleration, Prandtl number and Rayleigh number, respectively. The coefficient of volume expansion is taken as $\beta = 1/T$. Air properties are calculated at $(T_c + T_a)/2$.

It is common to assume steady state conditions and an opaque glass envelope for thermal radiation (Forristall 2003) in single tube receivers. Based on this assumption $Q_{loss}$ can be found from,

$$Q_{loss} = Q_{rc,rad} + Q_{rc,conv} = Q_{ca,rad} + Q_{ca,conv} \quad (4.24)$$

## 4.7 Thermal modelling of a trapezoidal cavity receiver

### 4.7.1 Calculation of heat loss coefficient

The trapezoidal cavity receiver has been frequently examined in research due to its low-cost design. Compared to a parabolic shaped secondary concentrator, a trapezoidal cavity uses flat reflective surfaces and is therefore cheaper to produce. Furthermore, this design does not require expensive glass tubes or a glass to metal welding, which is difficult to create. A schematic diagram of trapezoidal cavity receiver design with multi-tubes is shown in Figure 4.9. Receiver width ($w_r$) is a design variable in this study. A wide range of values has been reported for wall inclination ($\varphi$) and cavity depth ($d_{cp}$) in the literature (Facão and Oliveira 2011; Natarajan, Reddy and Mallick 2012; Qiu et al. 2016). Although, these parameters can also be design variables for a trapezoidal receiver, suitable fixed values are assigned at the optimization stage to reduce the number of design variables addressed.

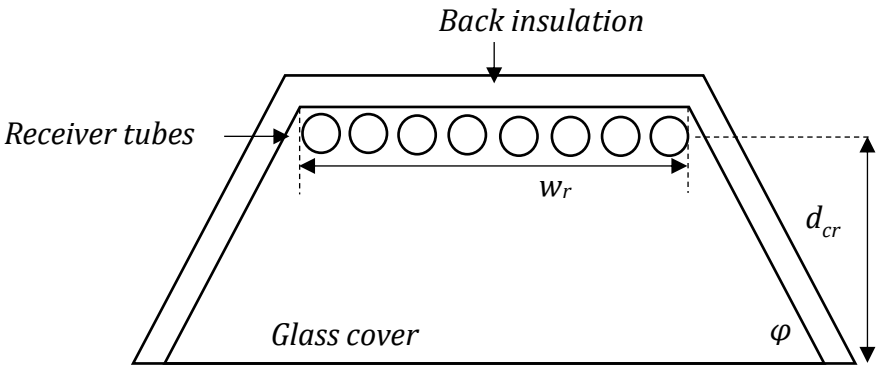


Figure 4.9: A schematic diagram of a trapezoidal cavity receiver with multi-tubes

To model the energy gains and losses in a trapezoidal cavity receiver, a parallel plate thermal method is used, where the receiver is modelled as two long parallel plates (Figure 4.10). This approach allows all significant heat transfer components to be included in an accurate thermal model and minimises lengthy iterating calculations to

save computational time. A similar approach has been used by other researchers (Singh, P. L., Sarviya, and Bhagoria 2010; Nixon 2012).

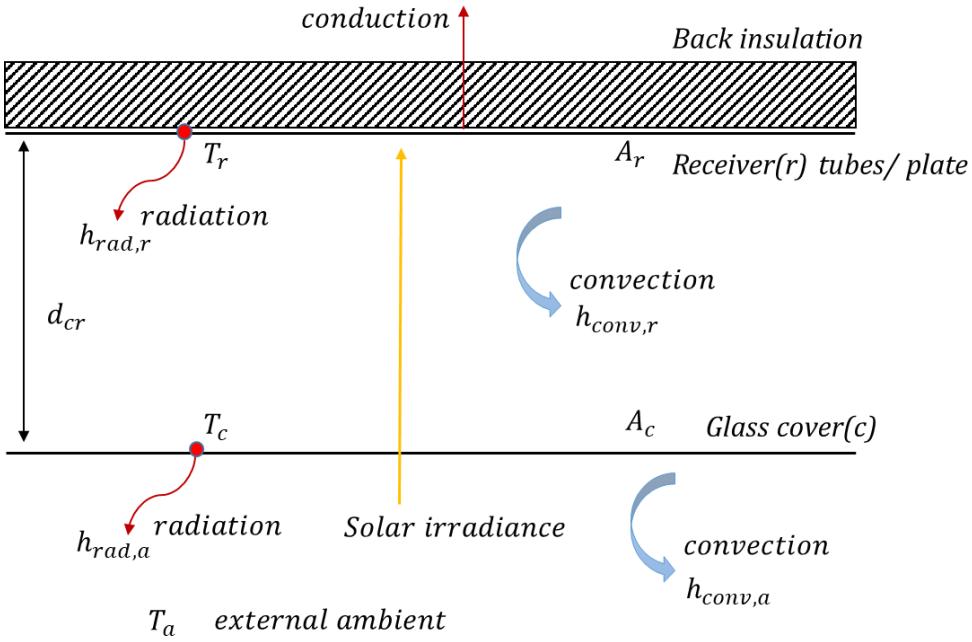


Figure 4.10: Heat transfer mechanisms of a trapezoidal cavity receiver are shown in a parallel plate thermal model

The heat loss coefficient ($U_L$) of a trapezoidal cavity receiver can be estimated as the sum of heat losses from the bottom of the receiver through the glass cover and through the insulation on the top. The heat loss coefficients from the bottom (glass cover) and top (insulation) of the receiver are taken as $U_{L1}$ and $U_{L2}$, respectively.

$$U_L = U_{L1} + U_{L2} \tag{4.25}$$

The heat loss from the bottom (glass cover) of the receiver is due to convection and radiation, and can be expressed as,

$$\frac{1}{U_{L1}} = \frac{1}{(h_{conv,r} + h_{rad,r})} + \left(\frac{A_r}{A_c}\right)\left(\frac{1}{h_{conv,a} + h_{rad,a}}\right) \tag{4.26}$$

where, $h_{conv,r}$ and $h_{rad,r}$ are convective heat transfer coefficient and radiative heat transfer coefficient from the receiver plate, respectively. $h_{conv,a}$ and $h_{rad,a}$ are the convective heat transfer coefficient and radiative heat transfer coefficient from glass cover to air, respectively. $A_r$ and $A_c$ are the surface areas of the plate facing the cavity and the glass cover, respectively. $h_{conv,r}$ can be estimated considering the convection heat transfer between two parallel plates as in equation (4.27) (Duffie and Beckman 2013). Since the receiver plate is normally hotter than the cover, creating pure conduction conditions between the plate and the cover, the Nusselt number ($Nu$) is taken as 1.

$$h_{conv,r} = Nu_{cr}\frac{k_a}{d_{cr}} \tag{4.27}$$

The thermal conductivity of air and the gap between the plates are taken as $k_a$ and $d_{cr}$, respectively. Air properties are taken at the mean temperature of parallel plates which is taken as $(T_r + T_c)/2$. Similarly, the convection coefficient $h_{conv,a}$ considering the laminar flow of air over the flat glass cover can be estimated as,

$$h_{conv,a} = Nu_{ca}\frac{k_a}{L_{ca}} \tag{4.28}$$

$$Nu_{ca} = 0.64(Re)^{0.5}(Pr_{ca})^{0.33} \quad 10^3 < Re < 2.6 \times 10^5 \tag{4.29}$$

$$Re = \frac{VL_{ca}}{\nu} \tag{4.30}$$

$$Pr_{ca} = \frac{\mu C_{pa}}{k_a} \tag{4.31}$$

where, $Re, Pr$, $V$and $L_{ca}$are Reynolds number, Prandtl number, fluid velocity and characteristic length, respectively. $C_{pa}$, $\mu$ and $\nu$ are specific heat, dynamic viscosity and kinematic viscosity of air. Air properties are taken at the mean temperature of the cover plate and ambient air, which is $(T_c + T_a)/2$.

Radiation heat transfer from the receiver plate is calculated considering the radiation interaction between the two parallel plates. Considering gray and diffuse radiation for an opaque surface and taking the radiation view factor as 1 (Cengel 2003),

$$h_{rad,r} = \frac{\sigma(T_r^2 + T_c^2)(T_r + T_c)}{\left(\frac{1}{\varepsilon_c} + \frac{1}{\varepsilon_r} - 1\right)} \tag{4.32}$$

where, $\sigma$ and $\varepsilon$ are Stefan-Boltzmann constant and emissivity, respectively.

Assuming the glass cover exchanges heat with an external ambient of $T_a$, the radiation heat transfer of the glass cover can be given by,

$$h_{rad,a} = \sigma\varepsilon_c(T_c^2 + T_a^2)(T_c + T_a) \tag{4.33}$$

The heat loss coefficient given in the equation (4.25) is obtained based on the conduction heat loss through the top insulation,

$$\frac{1}{U_{L2}} = \frac{1}{k_{im}/t_{im}} \tag{4.34}$$

where, $k_{im}$and $t_{im}$ are the thermal conductivity and thickness of insulation material respectively.

### 4.7.2 Calculation of glass cover temperature

The heat transfer equations mentioned in the section 4.7.1 can be solved if the glass cover temperature ($T_c$) is known. Alternatively, a suitable equation solving tool can be used. Under the steady state conditions, the heat input to the glass cover will be equal to the heat output. Heat input consists of radiation and conduction between the receiver plate and the glass cover. Heat output is a result of radiative losses to the surrounding and convection heat exchange with ambient air. Therefore, equations (4.27), (4.28), (4.32) and (4.33) can be combined as in equation (4.35).

$$\begin{aligned} h_{conv,r}\left(\frac{A_r + A_c}{2}\right)(T_r - T_c) + h_{rad,r}\left(\frac{A_r + A_c}{2}\right)(T_r - T_c) \\ = \quad h_{conv,a}A_c\,(T_c - T_a) + h_{rad,a}A_c\,(T_c - T_a) \end{aligned} \tag{4.35}$$

By rearranging the equation (4.35), $T_c$ can be obtained from the equation (4.37).

$$\left(h_{conv,r} + h_{rad,r}\right)\left(\frac{A_r + A_c}{2}\right)(T_r - T_c) = \left(h_{conv,a} + h_{rad,a}\right)A_c\,(T_c - T_a) \tag{4.36}$$

$$T_c = \frac{\left(\left(h_{conv,r} + h_{rad,r}\right)\left(\frac{A_r + A_c}{2}\right)T_r + \left(h_{conv,a} + h_{rad,a}\right)A_c T_a\right)}{\left(h_{conv,r} + h_{rad,r}\right)\left(\frac{A_r + A_c}{2}\right) + \left(h_{conv,a} + h_{rad,a}\right)A_c} \tag{4.37}$$

## 4.8 Receiver temperature operating conditions

Receiver temperature ($T_r$), previously introduced in equation (4.2), is an essential parameter required to solve thermal model equations presented in sections 4.6 and 4.7. Furthermore, the thermal energy output and potential power generation of the system depend on the operating temperature of the receiver. Unlike the other geometrical variables, receiver operating temperature is controlled by the solar irradiance, and receiver flow parameters, such as mass flow rate and inlet fluid temperature. Having fluid flow parameters in the modelling equations drastically increases the computational time and complexity of an optimization problem. Therefore, a uniform temperature boundary condition is assumed at the absorber tube to avoid additional complexity. This boundary condition has previously been used by Sahoo, Singh, and Banerjee (2012), Nixon and Davies (2012) and Moghimi, Craig, and Meyer (2015) to decouple the effects of the flow parameters on thermal performance. This temperature variation at different operational hours of the LFR system is categorised under two receiver temperature operating conditions, namely constant and variable. In the first operating condition, a single constant receiver temperature is maintained in the system. In the second operating condition, the temperature is either at a maximum limit (e.g. 400°C, based on material limits) or at an optimum receiver temperature ($T_{r,opt}$) to be maintained in order to maximise the power output (Kalogirou, 2004b),

$$T_{r,opt} = \sqrt{T_{r,max} T_a} \tag{4.38}$$

where, $T_{r,max}$ is the maximum receiver temperature and often referred to as stagnation temperature. This stagnation temperature can be calculated from equation (4.39).

$$T_{r,max} = \frac{I_{r,abs} A_r}{A_r U_L} + T_a \tag{4.39}$$

Other studies (Nixon and Davies 2012; Lin et al. 2013) have previously used this method to calculate LFR receiver temperature in their models. It is seen that $T_r$ and $U_L$ are coupled parameters and therefore have to be solved iteratively.

## 4.9 Energy analysis through the Rankine cycle

The steam Rankine cycle is the typical power cycle used in CSP power plants (NREL 2021). Converting thermal power delivered from the solar collector to electricity involves serval power block parameters to be considered such as evaporator effectiveness ($\eta_{ev}$), thermal efficiency of the power cycle ($\eta_{th}$), isentropic efficiency of the turbine ($\eta_{isen}$), mechanical efficiency of gearbox ($\eta_{mech}$), generator efficiency ($\eta_{gen}$) and fraction of auxiliary energy ($\eta_{aux}$). The power block efficiency ($\eta_{pb}$) considering all of these parameters can be expressed as in equation (4.40) (Escalante, Balestieri, and de Carvalho 2022).

$$\eta_{pb} = (\eta_{ev})(\eta_{th})(\eta_{isen})(\eta_{mech})(\eta_{gen})(\eta_{aux}) \tag{4.40}$$

In order to omit complicated heat exchange calculations, a minimum pinch point temperature difference is commonly used between the hot and cold fluid in an evaporator. This method is used here instead of calculating $\eta_{ev}$ by maintaining a lower steam temperature than the receiver temperature of the solar collector (Sun, Liu, and Duan 2018; Ziółkowski et al. 2021). The ideal Rankine cycle is shown on a T-s diagram as

in Figure 4.11 and it consists of the following four thermodynamic processes (Wang, X. D. et al. 2010).

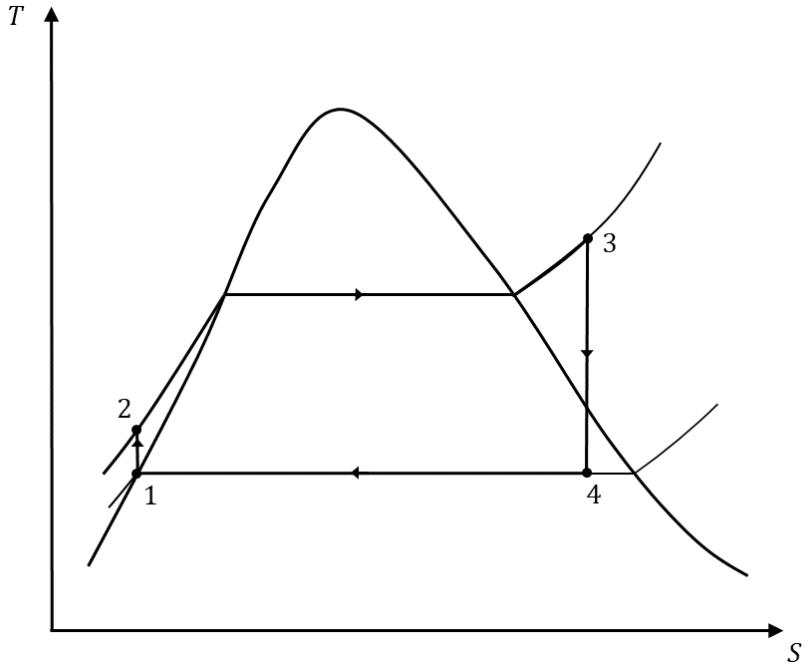


Figure 4.11: T-s diagram of an ideal Rankine cycle

1-2 Isentropic compression in a pump
2-3 Constant pressure heat addition (from solar collector)
3-4 Isentropic expansion in a turbine
4-1 Constant pressure heat rejection in a condenser

The thermal efficiency ($\eta_{th}$), of the Rankine cycle is determined as in equation (4.41) using the heat input and net-work delivered by the Rankine cycle ($W_{net}$) (Wang et al. 2010 ; Shahin, Orhan, and Uygul 2016).

$$\eta_{th} = \frac{W_{net}}{Q_o} \tag{4.41}$$

As the Rankine cycle is typically analysed as a steady-flow process, $\eta_{th}$ can be expressed in terms of enthalpy values of different states shown in Figure 4.11.

$$\eta_{th} = \frac{(h_{3-}h_2) - (h_{4-}h_1)}{(h_{4-}h_1)} \tag{4.42}$$

## 4.10 Cost modelling of LFR systems

Studies that provide a detailed cost breakdown based on actual LFR systems are not widely available. Most research has typically used values presented by Mertins (2009) following a detailed cost breakdown of the well-known Solarmundo LFR prototype (Moghimi, Craig, and Meyer 2017; Rungasamy, Craig, and Meyer 2019) with costs being categorised into four main areas: components, cost of mirrors, cost of mirror spacing, cost of receiver and cost of receiver height.

In order to calculate the mirror cost and mirror spacing cost, linear equations are used. Mertins (2009) combined the mirror, mounting, tracking and control systems into one component to obtain the mirror cost. The cost of a mirror per meter length of the plant ($C_m$) was assumed to be linearly proportional to the width of the mirror ($w_m$) as in equation (4.43). In the same way, the cost of mirror spacing per meter length of the plant ($C_s$) is mainly affected by the cost of the structure and can be expressed as in equation (4.44).

$$C_m = k_m w_m \tag{4.43}$$

$$C_s = k_s s_m \tag{4.44}$$

The constants, $k_m$ and $k_s$ are typically taken as 61 €/m$^2$ and 11.5 €/m$^2$ respectively (Mertins 2009; Moghimi, Craig, and Meyer 2017). Mirror spacing is given by $s_m$.

For a single tube receiver with a CPC, the cost of the receiver ($C_r$) and cost of receiver height ($C_h$) are largely dependent on the receiver tube diameter ($d_t$). This can be due to several parameters related to structural requirements, size of the CPC and cost of lifting operations. Mertins (2009) assumed that the receiver costs would be proportional to these parameters with an exponent of $n_c$. Furthermore, considering a receiver diameter

of 0.219 m of the Solarmundo plant, Mertins (2009) derived equations (4.45) and (4.46) to estimate the receiver costs.

$$C_r = k_r \left(\frac{d_t}{0.219}\right)^{n_c} \tag{4.45}$$

$$C_h = k_h \left(\frac{d_t}{0.219}\right)^{n_c} \tag{4.46}$$

Equations (4.45) and (4.46) use constants $k_r$ and $k_h$, which are taken as 654 €/m and 19.8 €/m², respectively. The exponent $n_c$ is calculated based on a detailed cost breakdown provided in Table 4.1 and calculated using equation (4.47) (Mertins 2009).

$$n_c = \frac{\ln\left(\sum \frac{C_i N_t}{k}\left(\frac{d_t}{0.219}\right)^{n_{C,i}}\right)}{\ln\left(\frac{d_t}{0.219}\right)} \tag{4.47}$$

The cost constants $k$, $C_i$ and the exponent $n_{C,i}$ for each cost element are shown in Table 4.1 and the number of tubes ($N_t$) is one for a single tube receiver with CPC.

Table 4.1: Cost elements for receiver and receiver height to be used with equation (4.47) (Mertins 2009)

| Receiver cost element | $k$ | $n_{C,i}$ | $C_i$, €/m |
|---|---|---|---|
| Absorber tube | | 2 | 161.2 |
| Selective coating | | 0.9 | 56.6 |
| Welding | | 0.7 | 116.4 |
| Construction | $k_r$ | 1.4 | 136.5 |
| Transportation and packing | | 0.6 | 26.4 |
| Assembly | | 0.6 | 112.6 |
| Secondary mirror, glass cover | | 0.9 | 44.1 |
| | | $n_{C,i}$ | $C_i$, €/m² |
| Construction | | 1.4 | 14.2 |
| Transportation and packing | $k_h$ | 1.0 | 0.9 |
| Assembly | | 1.0 | 4.6 |

Moghimi, Craig, and Meyer (2017) later used the equation (4.47) for a cost calculation of multi-tube receivers. However, when introducing a different number of tubes to this equation, corresponding cost elements have to be modified based on the receiver design.

Direct specific cost ($C_c^d$) [€/m$^2$], per unit mirror area of an LFR system can be expressed as,

$$C_c^d = \frac{C_m\, n_m + C_h(4 + h_r) + C_s(n_m - 1) + C_r}{n_m w_m} \tag{4.48}$$

As the mirror field of the Solarmundo was located 4 m above the ground, ($4+h_r$) was taken as the effective height for the cost calculation. The total cost of mirrors and mirror spacing were calculated by taking the number of mirrors ($n_m$) into account.

Land cost, including land acquisition and preparation is calculated separately as an indirect cost. The land cost is proportional to the total area of the mirrors ($A_c$) and determined using a land cost constant ($C_l$) of 3 €/m$^2$.

$$C_L = C_l A_c \left(1 + \frac{s_m}{w_m}\right) \tag{4.49}$$

The total investment of the plant ($C_t$) is expressed as in equation (4.50). The indirect cost constants used in this research are the same as those reported by Mertins (2009), and used by Moghimi, Craig, and Meyer (2017) and Rungasamy, Craig, and Meyer (2019) as given in Table 4.2.

$$C_t = \left(\left(C_c^d A_c + f_p\right)(1 + k_e) + C_L + f_I\right)(1 + k_u) + f_{PU} \tag{4.50}$$

Table 4.2: Indirect costs for a 50MW LFR power plant (Mertins 2009)

| Coefficient | Cost | Description |
|---|---|---|
| $f_p$ | 4 002 000 € | piping and steam traps |
| $f_I$ | 640 000 € | infrastructure |
| $f_{PU}$ | 33 600 000 € | Power plant unit (turbine, generator, condenser, feed water container and preheater) |
| $k_e$ | 0.225 | project efforts |
| $k_u$ | 0.05 | Uncertainties as a fraction of total investment |
| $k_{ac}$ | 0.09368 | Annuity factors as a fraction of total investment considering 25 years with an interest rate of 8% |
| $k_i$ | 0.01 | Annual insurance cost as a fraction of total investment |
| $k_{O\&M}$ | 0.02 | Operation and maintenance as a fraction of total investment |

The Levelized Cost of Electricity (LCOE), based on the assumption that the operating costs and electricity production remain constant throughout the lifetime of the project, is calculated as in equation (4.51) (Mertins 2009; Moghimi, Craig, and Meyer 2017; Rungasamy, Craig, and Meyer 2019).

$$LCOE = \frac{(k_{ac} + k_i + k_{O\&M})\, C_t}{Annual\ electricity\ yield} \tag{4.51}$$

## 4.11 Model verification

In this section, optical and thermal models described for a trapezoidal receiver and a single tube receiver with CPC in sections 4.5-4.7 are tested against experimental studies and other published models. As the studies that provide combined optical and thermal models are rare, the models are verified separately. A trapezoidal receiver design proposed by Pye (2008) and a commercial level receiver tube (SCHOTT PTR®70) with a CPC are used to verify the thermal models by comparing the receiver heat loss. A pilot LFR system installed in Vallipuram, India is used to verify the optical model for the single tube receiver by comparing the optical efficiency and receiver heat flux. Finally, a coupled optical and thermal model is compared against a modelling study of the Solarmundo LFR system using the total thermal efficiency.

### 4.11.1 Verification of the thermal model for a trapezoidal receiver

The trapezoidal receiver design, as seen in Figure 4.12, has been previously modelled by Pye (2008) using a CFD-based laminar steady-state cavity heat loss model. Reddy and Kumar (2014) analysed the same receiver using a two-dimensional numerical model for different cavity depths. The Parameter combination used in their work is shown in Table 4.3.

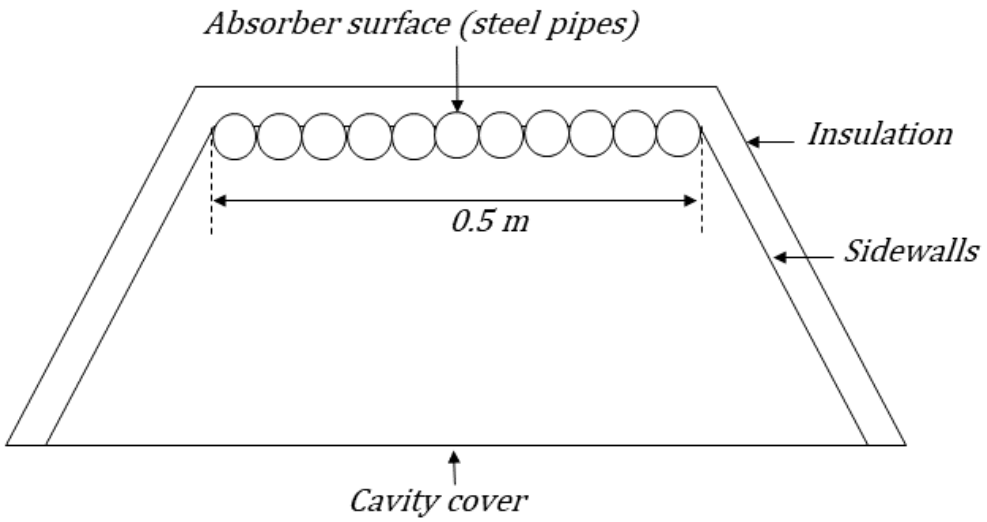


Figure 4.12: Trapezoidal receiver design of Pye (2008)

Table 4.3: Variable and fixed parameters used in steady state heat loss model (Pye 2008)

| | Parameter | Values |
|---|---|---|
| Varied parameters | Cavity depth | 100, 200, 300 mm |
| | Cavity width | 500, 1200 mm |
| | Absorber temperature | 530, 570, 610 K |
| | Ambient temperature | 290, 305 K |
| | External convection coefficient | 2.6, 10 W/m$^2$ |
| Fixed parameters | Absorber emissivity in cavity | 0.49 |
| | Wall emissivity in cavity | 0.1 |
| | Internal and external emissivity of the cover | 0.9 |
| | Cavity temperature | 370 K |
| | Side-walls external heat loss coefficient | 0.5 W/m$^2$K |
| | Sky temperature | 5 K above ambient |

In this work, the trapezoidal receiver shown in Figure 4.12 was modelled using the parallel plate thermal model as described in section 4.7 assigning the parameters given in Table 4.3. The modelling results are shown against results provided by Pye (2008) and Reddy and Kumar (2014) who used the same design (see Figure 4.13). Heat loss against cavity depth was obtained for three receiver temperatures, 530 K, 570 K and 610 K. The model developed by Reddy and Kumar (2014) provides lower heat losses compared to Pye (2008) by 7%, 6% and 9% for 530 K, 570 K and 610 K receiver temperatures, respectively. The model used in this thesis (section 4.7) provides higher heat losses compared to Pye (2008) by 4%, 5% and 7% for respective temperature values. All three models show a high heat loss variation for high temperatures. However, based on this comparison, the current model shows a better agreement with Pye (2008) compared to Reddy and Kumar (2014).

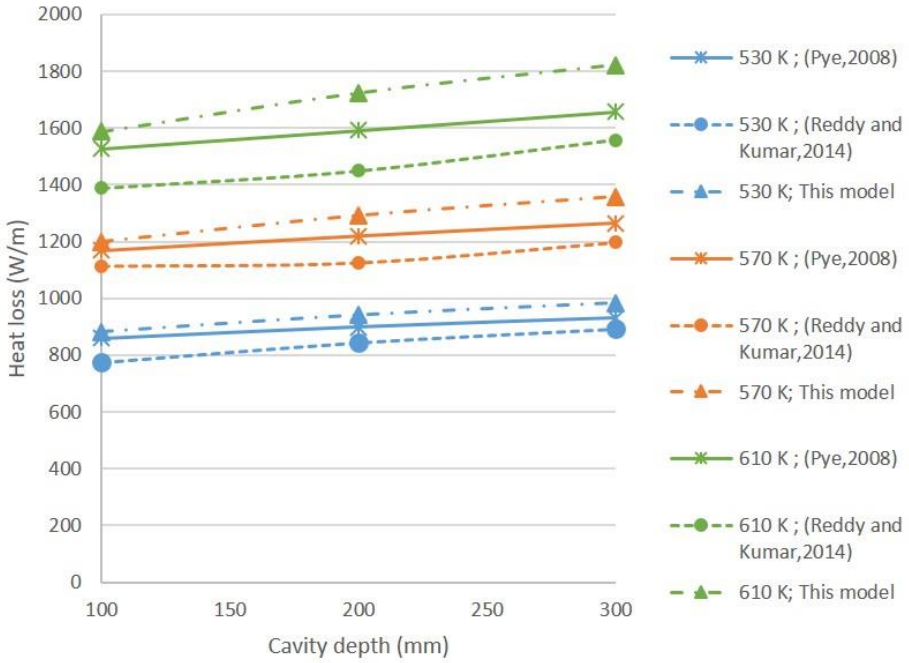


Figure 4.13: A comparison of the thermal model for a trapezoidal receiver with Pye (2008) and Reddy and Kumar (2014)

### 4.11.2 Verification of the thermal model for an evacuated tube with CPC

This section compares the evacuated tube thermal model used in this study for receiver heat loss with three other works. Cagnoli et al. (2018) numerically modelled the LFR system, located at the green energy park, Morocco, shown in Figure 4.14. They analysed the temperature dependency of the receiver's heat loss using a ray tracing code and CFD simulation. The receiver tube design used in their work was similar to the SCHOTT PTR®70, an off-the-shelf industrial design. The technical data used for the modelling is given in Figure Appendix A.1. The SCHOTT PTR®70, has been previously experimentally tested by NREL (Burkholder and Kutscher 2009).

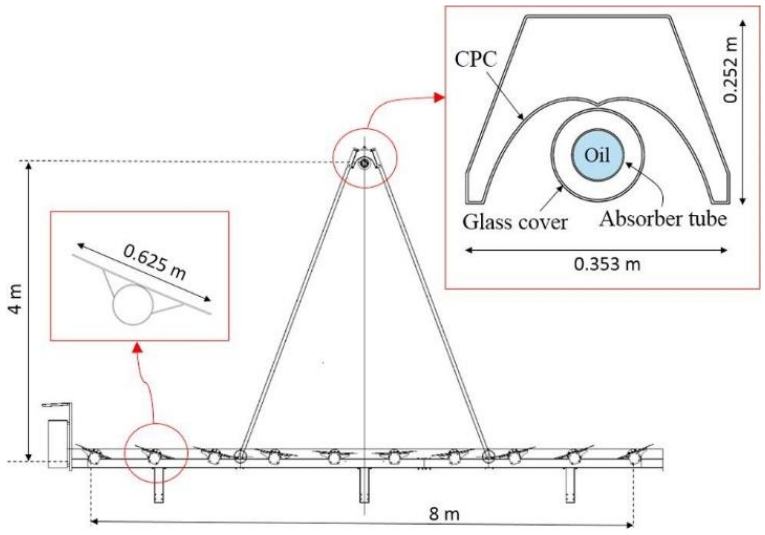


Figure 4.14: LFR collector modelled by Cagnoli et al. (2018); Copyright (2018), Reprinted with permission from Elsevier

The thermal model described in section 4.6 was used to model the SCHOTT PTR®70 and obtain the heat loss for the comparison. Figure 4.15 shows this modelling result against Cagnoli et al. (2018), NREL (Burkholder and Kutscher 2009) and technical specification provided for PTR®70 (SCHOTT solar 2013). The evacuated tube thermal model presented in section 4.6 shows an excellent agreement with both the reported experimental studies and the manufacturer's data. The heat loss presented by Cagnoli et al. (2018) is deviating from the results of this research when the receiver temperature increases. For instance, the heat loss obtained in this study is 11% lower at 550K.

Furthermore, it is important to note that the Cagnoli et al. (2018) model was based on an evacuated tube manufactured by Archimede Solar Energy (ASE). Therefore, some differences between the results can be expected, even though all the critical thermal parameters used have been the same for both manufacturers. It is important to note the experimental study carried out by the NREL was conducted on a bare evacuated tube without having a CPC. Since this study incorporates a CPC, which acts as a cover that blocks thermal radiation, it is expected that the heat loss to be lower compared to the experimental study, as seen in Figure 4.15 around 650 K.

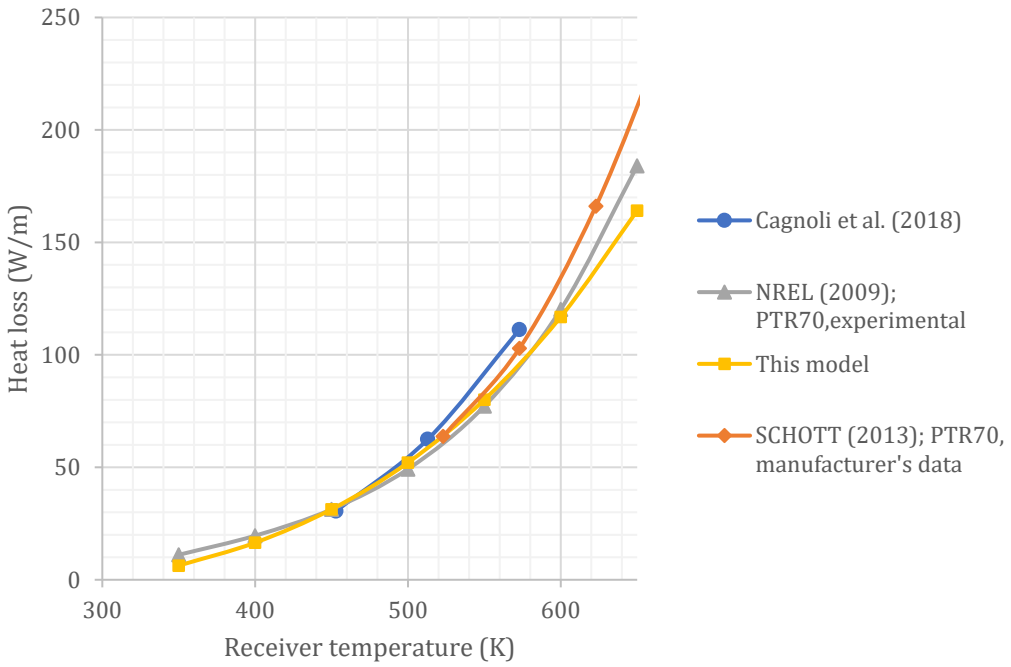


Figure 4.15: A comparison of the thermal model of this research with other work for an evacuated tube with CPC

### 4.11.3 Verification of optical modelling

To check the optical model, an existing design of an LFR plant located in Vallipuram, India (shown in Figure 4.16) was modelled using the modelling methodology described in section 4.5. This Vallipuram system was chosen as the CPC and receiver tube design has been widely reported (Balaji, Reddy, and Sundararajan 2016; Chaitanya Prasad, Reddy, and Sundararajan 2017; Bellos and Tzivanidis 2018). Specifications of the receiver tube used in the plant and these studies are equivalent to that of SCHOTT PTR®70. The LFR

plant was optically modelled using the modelling methods described in section 4.5 and compared against the work of Balaji, Reddy, and Sundararajan (2016) and Chaitanya Prasad, Reddy, and Sundararajan (2017) for optical efficiency and receiver heat flux. Critical design variables and parameters used in the modelling are as same as in Balaji, Reddy, and Sundararajan (2016) and listed in Table 4.4.

Figure 4.16: An LFR system installed at Vallipuram, India; Reprinted from Chaitanya Prasad, Reddy, and Sundararajan (2017), Copyright (2017), with permission from Elsevier

Table 4.4: Critical design variables and parameters used for optical model verification (Balaji, Reddy, and Sundararajan 2016; Chaitanya Prasad, Reddy, and Sundararajan 2017)

| Design variable/parameter | Value |
|---|---|
| Number of mirrors ($n_m$) | 12 |
| Mirror width ($w_m$) | 1.07 m |
| Mirror spacing ($s_m$) | 0.43 m |
| Receiver height ($h_r$) | 7.9 m |
| Absorber diameter | 0.07 m |
| Glass envelope outer diameter | 0.125 m |
| Thickness of glass envelope | 0.003 m |
| Reflectivity of mirrors | 0.94 |
| Reflectivity of CPC | 0.94 |
| Absorptivity of absorber | 0.92 |
| Tracking, slope and specularity errors | 0 mrad |
| Direct Normal Irradiance(DNI) | 1000 W/m$^2$ |
| Curvature of primary mirrors | variable |

Balaji, Reddy, and Sundararajan (2016) obtained an optical efficiency of 62.3%, using a commercial ray tracing tool called Advanced Systems Analysis Program, while this research provides 63.5% for the same LFR system using SolTrace. Therefore, the optical model provides a good agreement with their study and the 1.2% difference present between the studies is most likely due to the minor parameters not reported in the literature and the difference between the ray tracing tools. Furthermore, the work of Balaji, Reddy, and Sundararajan (2016) was extended to obtain a solar flux distribution around the absorber tube of the Vallipuram design (Chaitanya Prasad, Reddy, and Sundararajan 2017). As seen in Figure 4.17, this research also provides a similar flux distribution around the absorber, suggesting a reasonable agreement with their study.

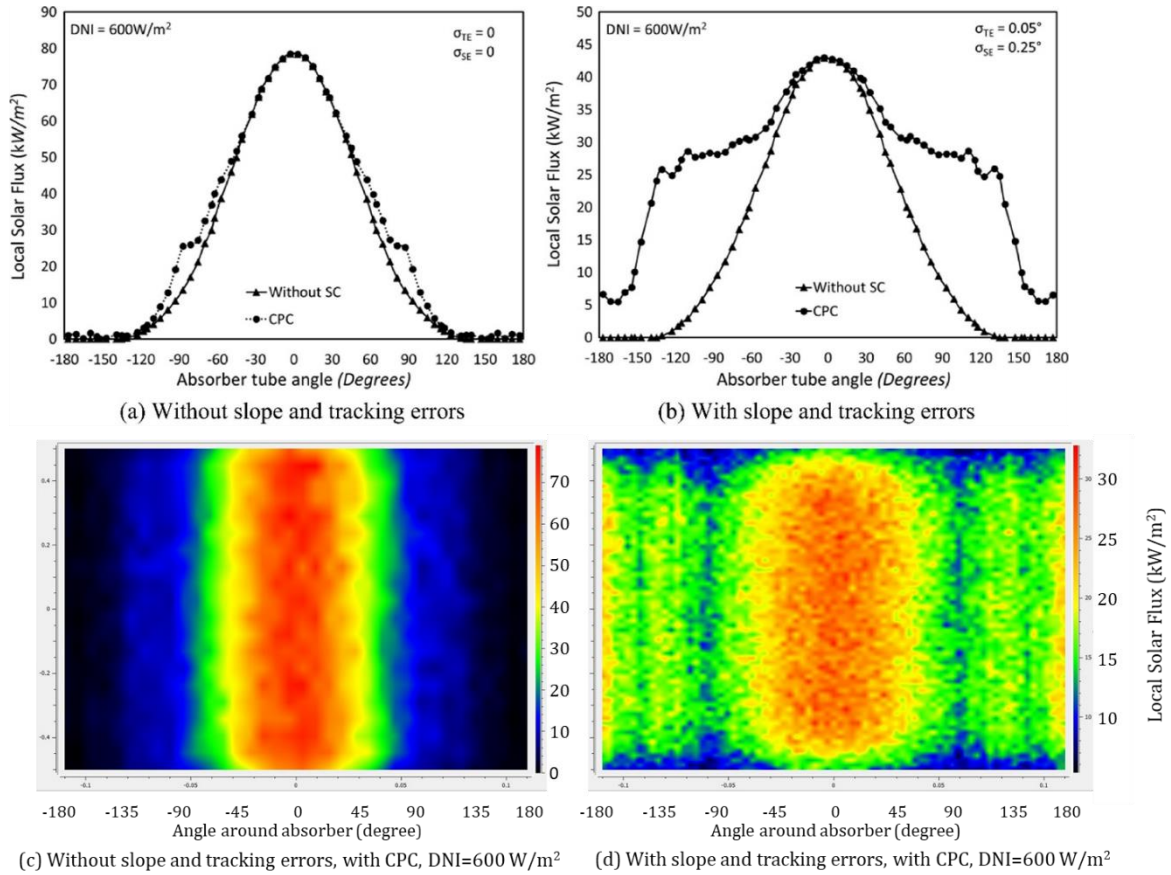


Figure 4.17: A comparison of absorber tube solar flux distribution for different modelling methods (when the mirror focal point lies on the absorber tube): (a) and (b) were obtained by Chaitanya Prasad, Reddy, and Sundararajan (2017) using a commercial ray tracing tool, Copyright (2017), Reprinted with permission from Elsevier; (c) and (d) are obtained in this study using SolTrace

### 4.11.4 A comparison of LFR collector (thermal) efficiency

Once the optical and thermal modelling is completed, plant collector efficiency (referred to as thermal efficiency in some reference), the ratio between the heat output and the solar energy input, can be calculated. Comprehensive studies addressing both optical and thermal simulations are rare. However, Häberle et al. (2002) presented collector efficiency for an LFR based on the Solarmundo power plant using a simple thermal model. Results of this study, obtained for the verified models for PTR®70 and the specified CPC design described, are found to be approximately the same to Häberle et al. (2002). Both studies illustrate a decreasing collector efficiency with receiver temperature. It is important to note that the Solarmundo plant did not have an evacuated tube receiver, which can significantly contribute to efficiency improvements. Furthermore, it had a much larger receiver than PTR®70, which can reduce the thermal efficiency due to higher heat loss. Although, a comparison of collector efficiency is provided in Figure 4.18 to show the trend and ranges of the collector efficiency, there is a significant difference in terms of the receiver designs and modelling methods used in the two studies.

A combination of thermal and optical modelling enables an LFR's collector efficiency to be calculated where the collector efficiency is the ratio between the heat output and the solar energy input. However, comparing different systems and models can be difficult as few publications attempt to combine both optical and thermal models, and each LFR system has variations in the design of receiver types. Häberle et al. (2002) presented a collector efficiency for an LFR based on the Solarmundo power plant. In comparison to this publication, the results for the PTR®70 with the CPC modelled in this study were found to be very similar (see Figure 4.18), with collector efficiency decreasing with receiver temperature.

Although, a comparison of collector efficiency is provided in Figure 4.18 to show the trend and ranges of the collector efficiency, there is a significant difference in terms of the receiver designs and modelling methods used in the two studies. As the Solarmundo plant did not have an evacuated tube receiver (Häberle et al. 2002), the efficiency is lower compared to this study. Furthermore, the Solarmundo had a much larger receiver than PTR®70, which could further reduce the collector efficiency.

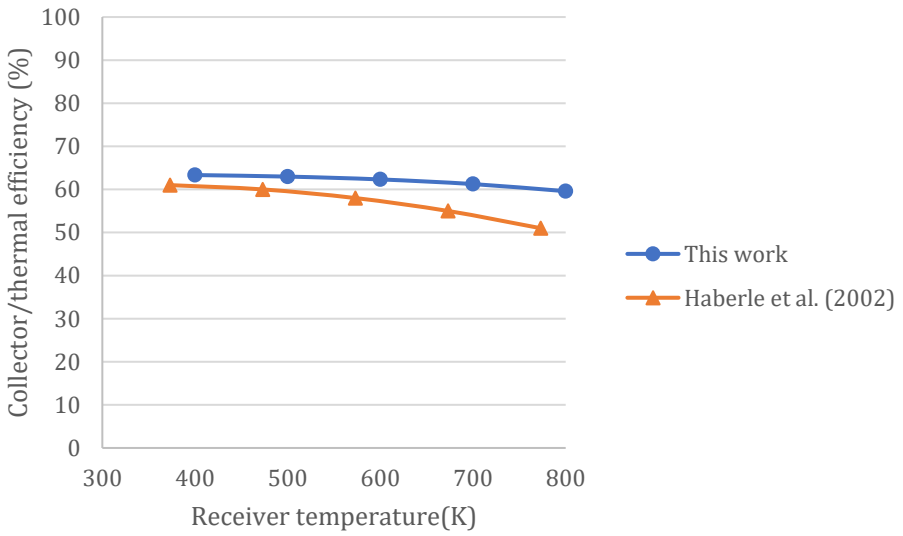


Figure 4.18: Collector (thermal) efficiency variation against receiver temperature of an LFR system

## 4.12 Summary

A coupled optical and thermal modelling approach for typical LFR systems was presented in this chapter. The optical model presented was implemented on the SolTrace ray tracing tool. A geometrical model was initially developed to form mirror and receiver geometries of a typical LFR system on a Cartesian coordinate system. Optical modelling parameters were established and the modelling process was automated through LK scripting to eliminate the manual modelling process. Thermal models were based on analytical equations and empirical correlations. The thermal model for a single tube receiver was developed using heat transfer theory and adapting models from PTC systems. A trapezoidal receiver was modelled adapting a parallel plate approach. Optical and thermal models developed were coupled together to obtain the energy output of the LFR system. The resulting equations were solved iteratively to calculate the unknown receiver and glass cover temperatures. Optical and thermal models were verified using the literature on experimental results, existing LFR systems and other modelling studies. A separate cost model was presented to calculate the LCOE. Using the coupled optical and

thermal models, all the model parameters needed to solve the optimization problems in Chapter 5 were calculated in this chapter.

# 5

# Optimization problem formulation and solver selection

## 5.1 Introduction

This chapter outlines a general formulation of the optimization problems and testing of different optimization methods on LFR systems. A block diagram of the optimization framework that combines the optical and thermal models described in the previous section is shown at the beginning of this chapter. Design variables and different objective functions are defined first. The testing and evaluation of different optimization methods are initiated on a simplified problem and gradually extend to the complete problem. Initially, one optimization variable is tested (1D problem) on a simple trapezoidal receiver and successful optimization methods are then tested on multiple variables and a single tube receiver with CPC. To evaluate the performance of different algorithms, three derivative-based, two derivative-free, one population-based and Simulated Annealing methods are tested. In order to check how accurate the optimized solution (provided by an optimization algorithm) is compared with the actual global solution, an exhaustive search is conducted on selected design variables and the results are compared. The chapter concludes by showing how the Genetic Algorithm (GA) was selected as the best performing optimization method and selection of GA parameters for use in the following chapter.

## 5.2 The optimization framework

The optimization framework that combines the optical and thermal models described in Chapter 4 is shown in Figure 5.1. Optimization and computational platforms are based on Matlab. SolTrace is used as the optical platform. Although Matlab and SolTrace were selected for this work, alternative platforms can also be used instead. In addition to the

optical and thermal models described in Chapter 4, the purpose of the geometrical model shown in the figure was to generate the coordinates needed to create an LFR system in 3D space for each SolTrace simulation.

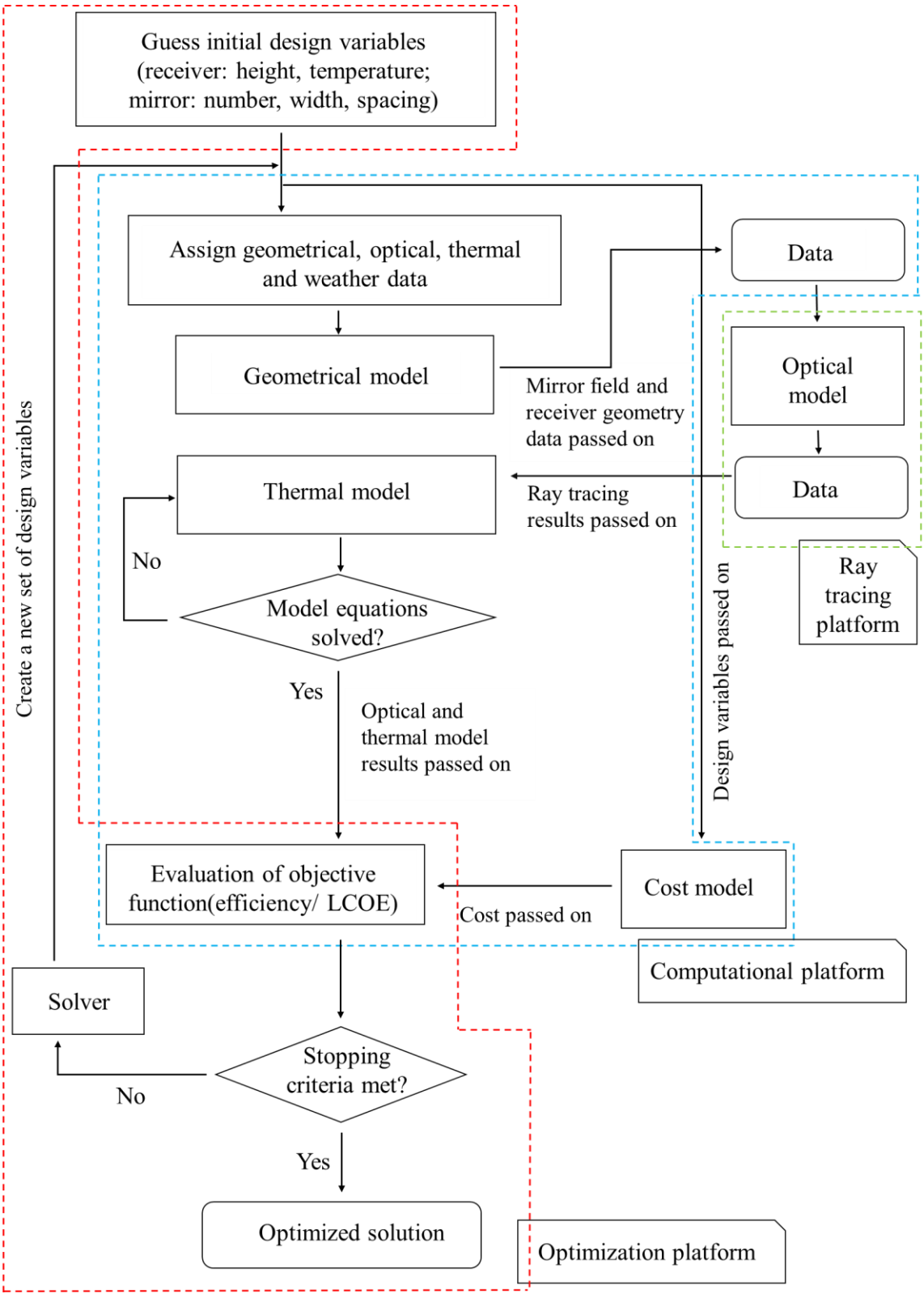


Figure 5.1: Linking of ray tracing (optical model), computational (modelling data, geometrical and thermal models) and optimization platforms in the optimization framework developed

## 5.3 Formulation of the optimization problems

In this research, two main objective functions are considered: total theoretical efficiency and Levelized Cost of Electricity (LCOE). Total theoretical efficiency is evaluated for receivers operating with either a constant or variable temperature. Design variables considered are: number of mirrors ($n_m$), mirror width ($w_m$), mirror spacing ($s_m$), receiver width ($w_r$), receiver height ($h_r$) and receiver temperature ($T_r$). Some of these design variables are kept constant (explicitly mentioned in relevant sections) in the process of identifying a suitable optimization method that can effectively handle all design variables.

The first objective function considered is total theoretical efficiency ( $\eta_{total,th}$) which is the ratio between the maximum power generation potential and solar input power. For *N* number of hours of sunlight $\eta_{total,th}$ of the LFR system is given by,

$$\eta_{total,th} = \frac{\sum_{j=1}^{N} Q_{o,j}\left(1 - \frac{T_a}{T_{r,j}}\right)}{\sum_{j=1}^{N} E_{m,j}} \tag{5.1}$$

where the terms in the denominator are given by equations (5.2).

When an LFR system with *n* mirror elements receives $DNI_j$ during a $j^{th}$ hour of a specific day, $E_{m,j}$ represents the total amount of solar energy received on the effective aperture of all mirror elements.

$$E_{m,j} = \sum_{i=1}^{i=n} DNI_j \, A_{m,i} \cos\theta_i \tag{5.2}$$

The total theoretical efficiency for $j^{th}$ hour of a specific day ($\eta_{total,th,j}$) is calculated assuming a coupled Carnot cycle operating between the receiver temperature ($T_r$) and ambient temperature ($T_a$) (Nixon and Davies 2012; Romero, Gonzalez-Aguilar, and Zarza 2015; Abbas et al. 2016) and (see Chapter 3.3). The heat output of the LFR system ($Q_o$) is obtained as described in Chapter 4.2.

$$\eta_{total,th,j} = \frac{Q_{o,j}\left(1 - \frac{T_a}{T_{r,j}}\right)}{E_{m,j}} \tag{5.3}$$

For a constant receiver temperature operating condition (i.e. a single receiver temperature is maintained throughout the day by controlling the heat transfer fluid flow rate), the objective function becomes:

$$\max_{n_m, w_m, s_m, w_r, h_r, T_r} \eta_{total,th}(n_m, w_m, s_m, w_r, h_r, T_r, P_{thermal}, P_{optical})$$

Subject to

$x \in [x_{min}, x_{max}]^+$

$n_m \in Z^+$

$Q_o \geq 0$

For a variable receiver temperature operating condition, $T_r$ is maintained at a thermodynamically optimum value, $T_{r,opt}$, until it reaches a maximum limit ($T_{lim}$) (e.g. 400°C due to the receiver material and components). See equations (4.38) and (4.39) for more information on the calculation of $T_{r,opt}$ based on the minimum entropy generation principle for different operational hours.

$$\max_{n_m, w_m, s_m, w_r, h_r} \eta_{total,th}(n_m, w_m, s_m, w_r, h_r, T_r, P_{thermal}, P_{optical})$$

Subject to

$x \in [x_{min}, x_{max}]^+$

$n_m \in Z^+$

$Q_o \geq 0$

$$T_r = \begin{cases} T_{r,opt} & when\ T_{r,opt} < T_{lim} \\ T_{lim} & otherwise \end{cases}$$

Solar thermal power generation technologies need to be able to provide low-cost energy. Therefore, LCOE is used as a second objective function, which can be calculated from the ratio between the annual cost of the plant ($C_a$) and electricity yield. Considering a day

with *N* number of hours of sunlight, annual electricity yield can be expressed as shown in equation (5.5) (Rungasamy, Craig, and Meyer 2019).

$$LCOE = \frac{C_a}{Annual\ electricity\ yield} \tag{5.4}$$

$$Annual\ electricity\ yield\ = \sum_{day=1}^{365} \sum_{j=1}^{N} Q_{o,j}\ \eta_{pb} \tag{5.5}$$

The power block efficiency ($\eta_{pb}$) typically varies between 30-40% for a CSP plant (Wang, A. et al. 2019; Yan, H. et al. 2021). For LCOE optimization $\eta_{pb}$ was fixed at 0.33 (Häberle et al. 2002; Rungasamy, Craig, and Meyer 2019). The heat output of the LFR system ($Q_o$) is obtained as described in Chapter 4.3.

$$\min_{n_m, w_m, s_m, h_r} LCOE(n_m, w_m, s_m, w_r, h_r, T_r, P_{thermal}, P_{optical}, P_{cost})$$

Subject to

$x \in [x_{min}, x_{max}]^+$

$n_m \in Z^+$

$Q_o \geq 0$

## 5.4 Selection of an optimization algorithm

### 5.4.1 Establishing optimization parameters for a trapezoidal receiver

This section discusses the testing of different optimization methods for a simplified trapezoidal receiver and how a suitable optimization method has been selected for further work. Figure 5.2 shows a schematic diagram of a simplified trapezoidal cavity receiver with fixed cavity wall inclination ($\varphi$) and cavity depth ($d_{cr}$). To make the receiver solar flux pattern and simulation results smooth, receiver tubes were replaced by a flat plate in the optical model (Boito and Grena 2016). Selected values for the modelling parameters are given in Table 5.1. The Objective function to be optimized was the total theoretical efficiency of power generation ($\eta_{total,th}$) with variable receiver temperature

operating condition. Initially, the optimization was applied to one variable and gradually expanded to four variables except for the number of mirrors ($n_m$), which was maintained at selected values. The other design variables were mirror width ($w_m$), mirror spacing ($s_m$), receiver height ($h_r$) and receiver width ($w_r$), respectively (see Figure 5.3).

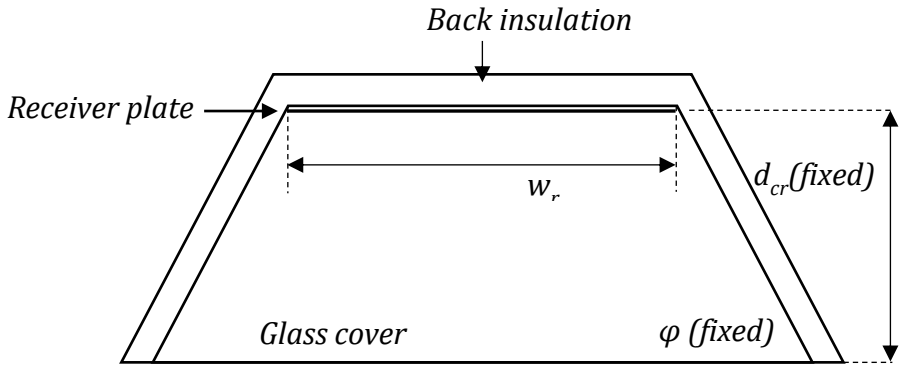


Figure 5.2: Schematic diagram of a simplified trapezoidal cavity receiver with fixed design parameters

Table 5.1: Selected optimization parameters of a trapezoidal cavity receiver

| | |
|---|---|
| $d_{cr}$ | $w_r/3$ (Natarajan, Reddy, and Mallick 2012) |
| φ | $\tan^{-1}\left(\frac{2h_r}{(w_m+s_m)n_m-s_m}\right)$ (based on mirror field width) |
| DNI | 500 W/m$^2$ (the sun is directly above the system) |

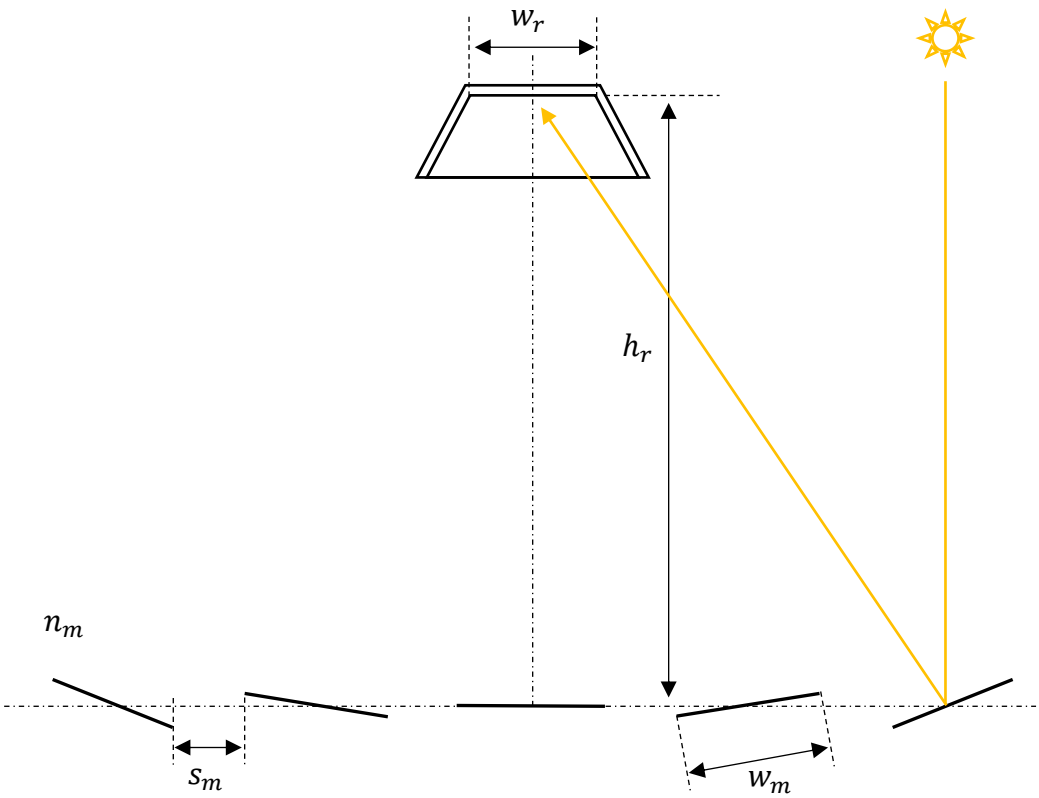


Figure 5.3: Schematic of a 2D view of a simplified LFR system with a trapezoidal cavity receiver

Several optimization methods were verified to identify the best alternatives, which can provide sufficient accuracy with the least computational effort. Three derivative-based methods (Interior-point, SQP and active set), two derivative-free methods (pattern search and fminsearch), one population based optimization method (GA) and Simulated Annealing were tested based on the literature and availability of algorithms in Matlab. Initially, one optimization variable was selected for simplicity and tested using computationally effective methods. The optimization was extended subsequently to four optimization variables, which have been repeated for three different values of number of mirrors ($n_m$). Number of mirrors was not used as an optimization variable at this stage to avoid a mix-integer problem, which typically makes optimization complex.

### 5.4.2 Solving the optimization problem for one variable

Initially, the problem is simplified to a one-dimensional problem (1D problem) by assigning constant values for four design variables and keeping the receiver height ($h_r$) as a variable. Receiver height has a high sensitivity for maximising optical efficiency and

therefore is selected for initial testing of an optimization method (Sirimanna and Nixon 2020). A summary of the optimization problem and values of the constant variables are shown in Table 5.2. Before running the optimization algorithms, an exhaustive search was run for the values mentioned in Table 5.2 to identify the trend and the global maximum of the objective function. For this purpose, the receiver height ($h_r$) was discretised into 1 m segments within a range of 2-30 and optical and thermal models were run to calculate the objective function separately.

Table 5.2: Optimization variables and their values selected for the 1D problem

| | |
|---|---|
| Objective function | $\eta_{total,th}$ |
| Design variable to be optimized | Receiver height ($h_r$) |
| Bounds | $2 \leq h_r \leq 30$ |
| Fixed design variables(parameters) | |
| Number of mirrors ($n_m$) | 54 |
| Mirror width ($w_m$) | 0.6 m |
| Mirror spacing ($s_m$) | 0.15 m |
| Receiver width ($w_r$) | 0.9 m |

#### 5.4.2.1 Candidate derivative-based optimization methods

To begin the optimization, three derivative-based methods, interior-point, SQP and active set were employed to obtain a solution for the optimization problem. As the first step, 60 randomised points were generated as the initial guess within the entire range of $h_r$. Each optimization algorithm was run 60 times to receive the maximum $\eta_{total,th}$ and corresponding optimum $h_r$. Detailed results and starting points are shown in Table Appendix B.1. Matlab optimization solvers were used for these simulations and the stopping criteria was set to default in the solver. Stopping criteria and other settings used in the simulation are shown in Table 5.3. Optimization results for the three algorithms and their comparison with the exhaustive search are shown in Figure 5.4.

Table 5.3: Stopping criteria and other default optimization settings used in Matlab optimization toolbox

| | Interior-point | SQP | Active set |
|---|---|---|---|
| Maximum iterations | $10^3$ | 400 | 400 |
| Maximum function evaluations | $3 \times 10^3$ | 100 | 100 |
| X tolerance | $10^{-10}$ | $10^{-6}$ | $10^{-6}$ |
| Function tolerance | $10^{-6}$ | $10^{-6}$ and$10^{-3}$ | $10^{-3}$ |
| Constraint tolerance | $10^{-6}$ | $10^{-6}$ | $10^{-6}$ |
| Unboundedness threshold | $-10^{20}$ | $-10^{20}$ | NA |
| Derivative types | Forward difference | Forward difference | Forward difference |
| Hessian | BFGS | NA | NA |

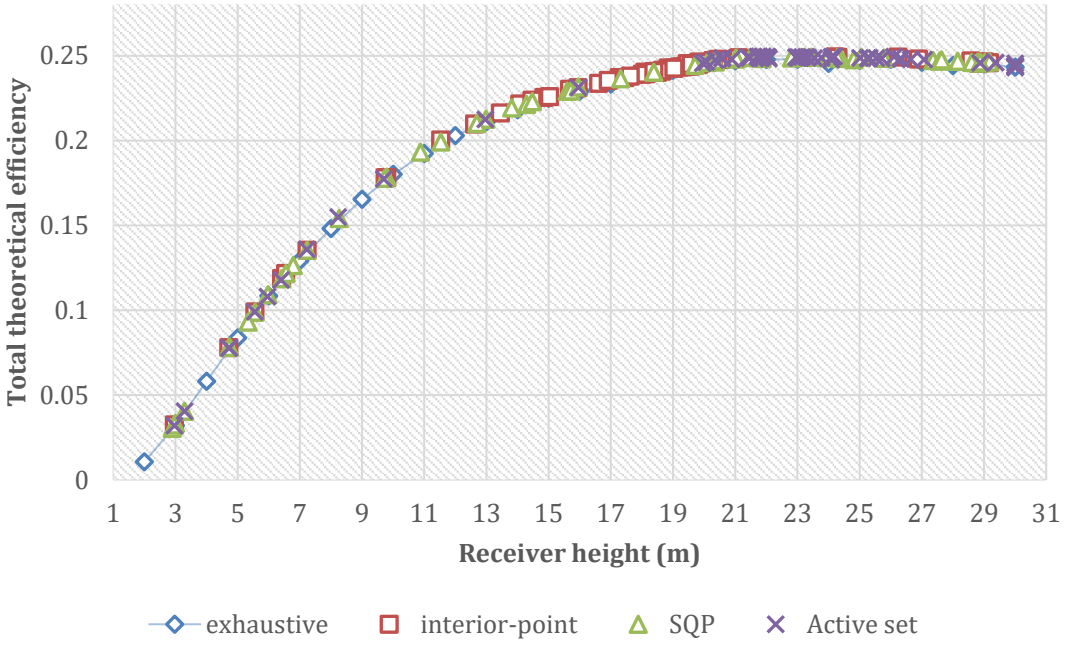


Figure 5.4: Comparison of exhaustive search results against interior-point, SQP and active set algorithms. Distributed results in the receiver height domain indicate that none of the methods has been successful

Based on the results in Figure 5.4, it is seen that no algorithm is providing a satisfactory result. A global maximum of 0.248 is observed for $h_r$=23 by the exhaustive search method. Most of the optimized solutions are gathered between 16 and 21 for the interior point method. For SQP, almost all of the results are trapped at the initial guess (Table Appendix B.1). The result did not improve, even after decreasing the step size (function tolerance)

of the fitness value. The active set algorithm shows better results compared to other algorithms, where many solutions are gathered between 21 and 26(see Table Appendix B.2 for more detail). However, a large number of solutions were still trapped around the initial guess.

Since all derivative-based methods were trapped in local solutions in many cases, an exhaustive search was conducted for a refined grid to check for possible errors and oscillations in the objective function. $h_r$ was discretised into segments of 0.02 and the objective function was calculated for each value. The result of this simulation is shown in Figure 5.5. It is seen that a large number of oscillations exists in the objective function for a refined grid. Several local maximum points are shown in the figure implying that derivative-based local solvers can get trapped in these local maximum points. Followed by this observation, derivative-free and global optimization methods were selected to obtain better results.

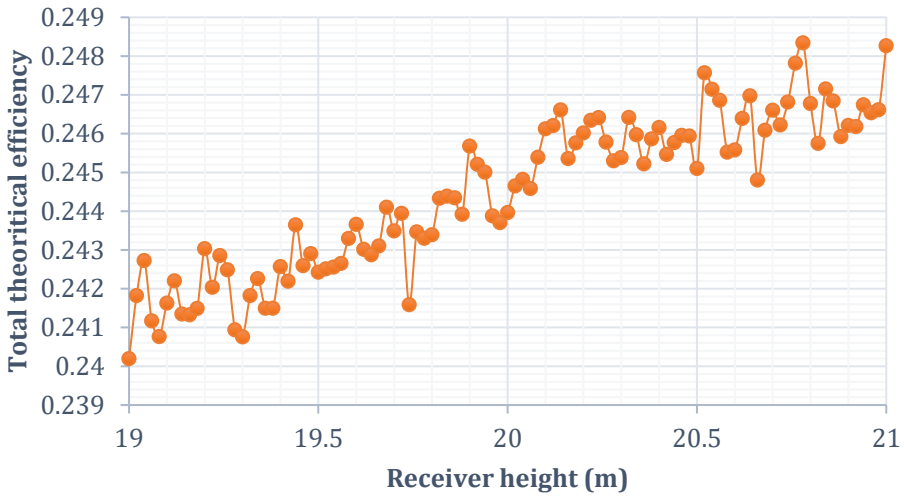


Figure 5.5: Exhaustive search for a refined grid

### 5.4.2.2 Candidate derivative-free and population-based methods

Two derivative-free methods, pattern search and fminsearch solver (this solver uses Nelder-Mead simplex algorithm) in Matlab, were selected and eight simulations were carried out for each method. Figure 5.6 shows that all eight optimization results are gathered around the neighbourhood of the global optimum. These results show a very good agreement with the exhaustive search. Two global optimization methods, Simulated

Annealing and GA, were also used to check their behaviour for the objective function. As seen in Figure 5.7, all these results lay between 22 and 23, and were very close to the global optimum, $h_r$ =23. Detailed results for these simulations are shown in (Table Appendix B.3 and Table Appendix B.4). All simulations were run using default settings except the function tolerance, which was reduced to $10^{-3}$ to minimise the disturbances due to the oscillations found(Figure 5.5) in the fitness value.

Simulated Annealing and GA showed the best results in consecutive runs showing close solutions to each other. In terms of simulation time, GA was roughly seven times more computationally expensive compared to Simulated Annealing, as seen in Figure 5.8. Furthermore, derivative-free methods also showed promising solutions with less computational time. As the next step, the optimization was expanded to four continuous variables to evaluate how the selected algorithms would perform for a 4D problem.

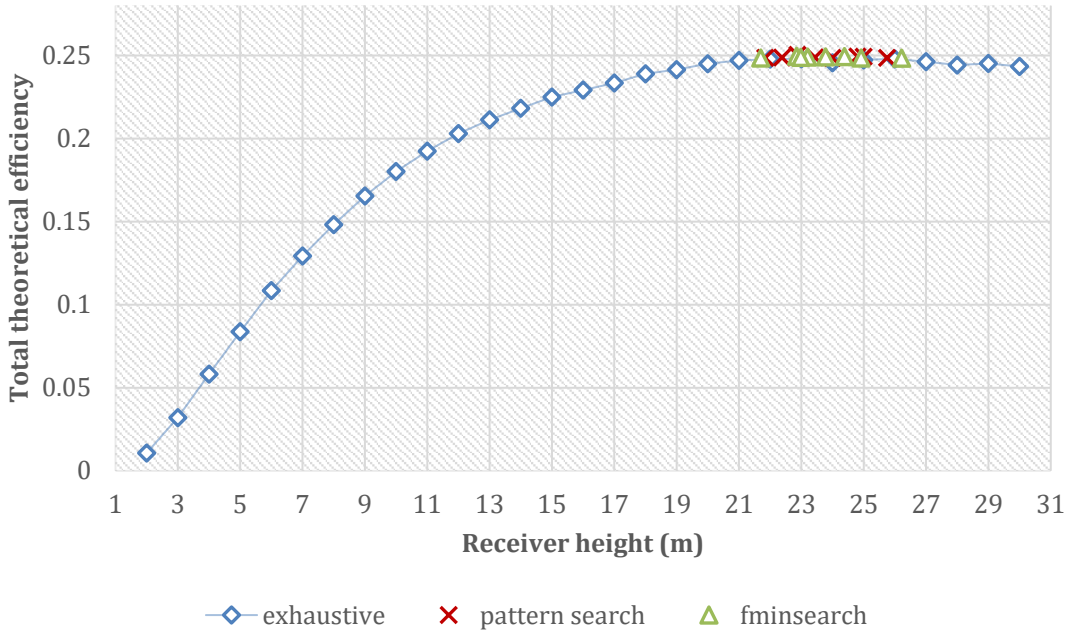


Figure 5.6: Comparison of exhaustive search results against two derivative-free methods

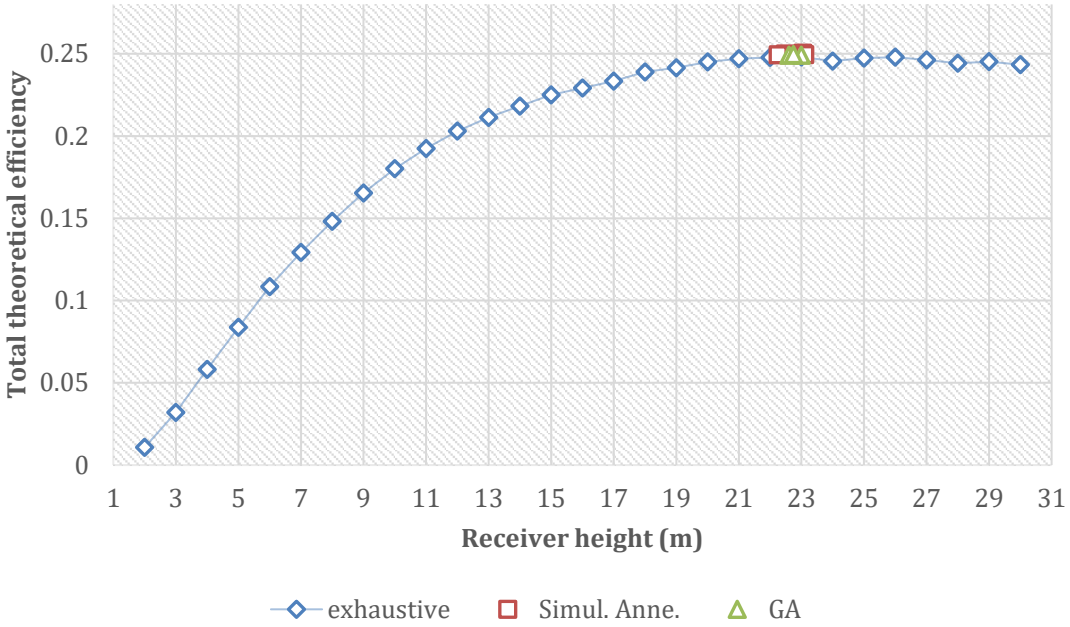


Figure 5.7: Comparison of exhaustive search results against a population-based method (GA) and simulated annealing

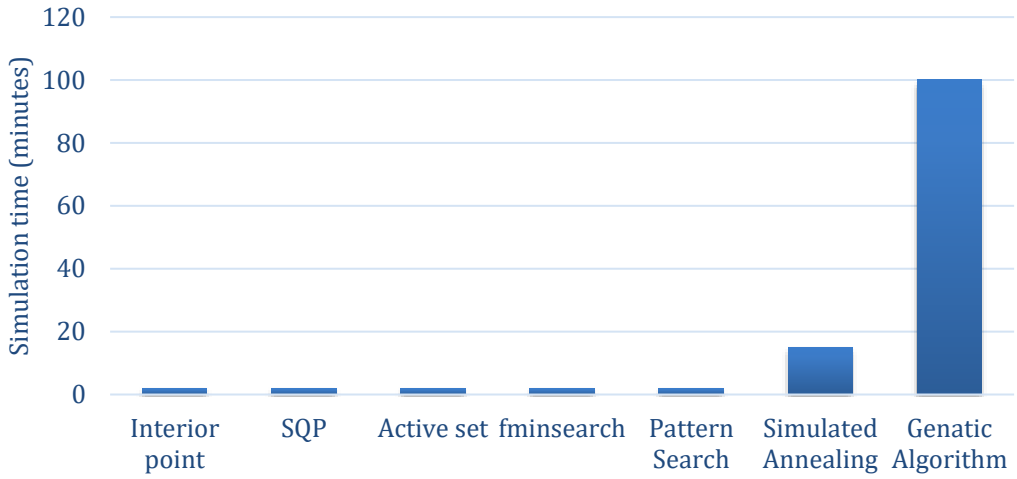


Figure 5.8: Simulation time taken by different algorithms for the one-dimensional problem

### 5.4.3 Approaching a multidimensional problem

Before expanding the optimization problem for multiple variables, it is advantageous to know how the objective function behaves for multiple design variables using an exhaustive search. This supports running the optimization smoothly, getting an idea about the possible solutions and setting up bounds for variables. Figure 5.9 and Figure 5.10 show contour diagrams obtained by changing receiver width, receiver height and mirror number using the exhaustive search approach.

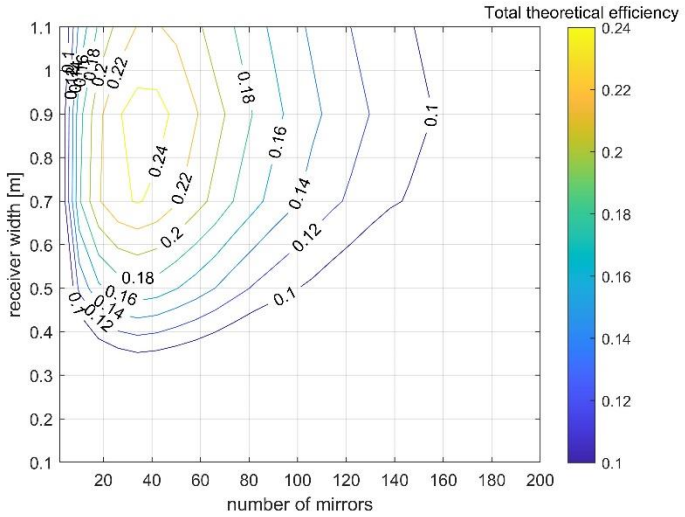


Figure 5.9: Variation of total theoretical efficiency ($\eta_{total,th}$) against $n_m$ and $w_r$ ($h_r$=9m, $w_m$=0.6m and $s_m$=0.25m)

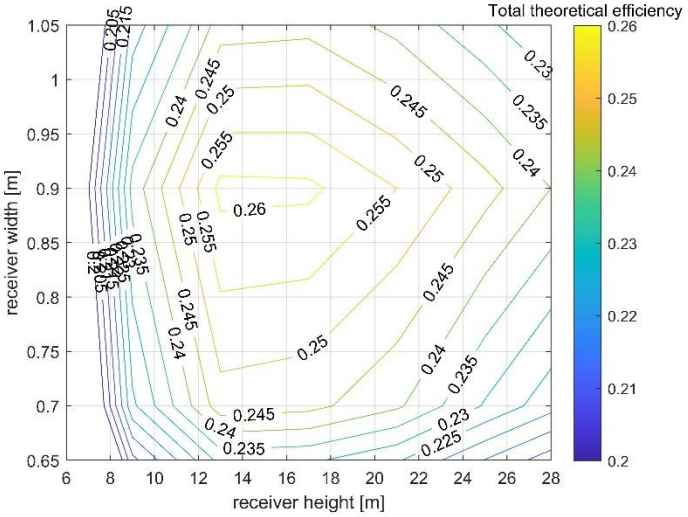


Figure 5.10: Variation of total theoretical efficiency ($\eta_{total,th}$) against $h_r$ and $w_r$ ( $n_m$=50, $w_m$=0.6m and $s_m$=0.25m)

Figure 5.9 and Figure 5.10 show that a single global maximum exists even for a multidimensional problem. Furthermore, setting a large upper bound for the mirror number may not be required, as the efficiency becomes significantly lower at large mirror numbers. In addition to this, potential variable bounds for receiver width and height were identified to be used in further simulations.

### 5.4.4 A candidate optimization method for a multidimensional problem

Based on the analysis of the results in Chapters 5.4.2 and 5.4.3, the optimization was expanded to four continuous variables ($h_r$, $w_m$, $s_m$, $w_r$) while keeping the fifth variable ($n_m$) at selected discrete values. Thus, a four-dimensional continuous optimization problem is solved for each value of $n_m$. Table 5.4 shows a description of the problem to be tested with the optimization algorithms, which had performed well thus far (pattern search, simulated annealing and GA). In order to assess the accuracy of the optimizers, an exhaustive search was performed discretizing all four continuous variables. Table 5.5 shows the ranges and their discretization of these variables, which were used for the exhaustive search.

Table 5.4: A summary of the 4D problem to be solved using an optimization algorithm

| | |
|---|---|
| Objective function | Total theoretical efficiency($\eta_{total,th}$) |
| Design variable to be optimized | $h_r$, $w_m$, $s_m$, $w_r$ |
| Variable bounds | $2 \leq h_r \leq 30$<br>$0.1 \leq w_m \leq 1.2$<br>$0.05 \leq s_m \leq 0.3$<br>$0.1 \leq w_r \leq 1.2$ |
| Fixed design variables (parameters) | $n_m = 10, 30, 54$ ; $n_m \in Z^+$ |

Table 5.5: Design variables and their discretization for exhaustive search

| Variable | Range | Discretization for exhaustive search | |
|---|---|---|---|
| | | Step size | Sample values |
| Receiver height ($h_r$) | $1 \leq h_r \leq 30$ | 4 m | 1, 5, 9,…….21, 25, 29 |
| Mirror width ($w_m$) | $0.1 \leq w_m \leq 1.2$ | 0.2 m | 0.1, 0.3, 0.5……0.9,1.1 |
| Mirror spacing ($s_m$) | $0.05 \leq s_m \leq 0.3$ | 0.05 m | 0.05, 0.1, 0.15……0.25, 0.3 |
| Receiver width ($w_r$) | $0.1 \leq w_r \leq 1.2$ | 0.2 m | 0.1, 0.3, 0.5……0.9,1.1 |
| Number of mirrors ($n_m$), $n_m \in Z^+$ | $2 \leq n_m \leq 78$ | 4 | 2, 6, 10……74, 78 |

The ten best simulation results from the exhaustive search for $n_m$=10 are shown in Table 5.6. These results have been sorted from the largest to the smallest value based on the calculated objective function values. It can be observed that the differences between the total theoretical efficiency of the global optimum and that of neighbouring designs are very small. In fact, the first two solutions may be deemed global maxima if rounding total theoretical efficiency to three decimals. Then, the global maxima would be found at $h_r = 9$, $w_r = 0.9$, $w_m = 0.9$, whilst $s_m$could take either 0.09 m or 0.13 m. However, the design variables have been discretised to obtain these solutions. For the continuous case, the actual global optimum may lie nearby. Therefore, it is possible that a global search algorithm can find even better solutions than the exhaustive search.

The optimal solutions obtained by pattern search, simulated annealing and GA algorithms are shown in Table 5.7. It is seen that all the optimized variables using simulated annealing and genetic algorithm lie within the ranges previously identified by the exhaustive search. Furthermore, it can be observed that all the solvers have maximised $\eta_{total,th}$ to find an optimum between 0.170 and 0.172 (a total theoretical efficiency of 17% -17.2%). Figure 5.11 shows a comparison of these results in terms of the maximised solution.

Table 5.6: Results of the exhaustive search for $n_m$=10

| Receiver height($h_r$) (m) | Receiver width($w_r$) (m) | Mirror width($w_m$) (m) | Mirror spacing( $s_m$) (m) | Max $\eta_{total,th}$ | Max $\eta_{total,th}$ rounded |
|---|---|---|---|---|---|
| 9 | 0.9 | 0.9 | 0.09 | 0.169046 | 0.169 |
| 9 | 0.9 | 0.9 | 0.13 | 0.168863 | 0.169 |
| 13 | 0.9 | 0.9 | 0.29 | 0.168355 | 0.168 |
| 13 | 0.9 | 0.9 | 0.17 | 0.168300 | 0.168 |
| 13 | 0.9 | 0.9 | 0.25 | 0.167729 | 0.168 |
| 9 | 0.9 | 0.9 | 0.05 | 0.167573 | 0.168 |
| 13 | 0.9 | 0.9 | 0.21 | 0.167472 | 0.167 |
| 9 | 0.9 | 0.9 | 0.17 | 0.167419 | 0.167 |
| 13 | 0.9 | 0.9 | 0.09 | 0.167098 | 0.167 |
| 13 | 0.9 | 0.9 | 0.05 | 0.166906 | 0.167 |

Table 5.7: Optimization results of three optimization algorithms for $n_m$ =10

| Number of mirrors ($n_m$)=10 | | Pattern search | | Simulated Annealing | | Genetic Algorithm | |
|---|---|---|---|---|---|---|---|
| | | optimized variables (m) | Max $\eta_{total,th}$ | optimized variables (m) | Max $\eta_{total,th}$ | optimized variables (m) | Max $\eta_{total,th}$ |
| 1st run | $h_r$ | 10.5 | 0.1713 | 9.92 | 0.1715 | 8.92 | 0.1711 |
| | $w_r$ | 0.878 | | 0.852 | | 0.799 | |
| | $w_m$ | 0.89 | | 0.861 | | 0.833 | |
| | $s_m$ | 0.247 | | 0.103 | | 0.115 | |
| 2nd run | $h_r$ | 11 | 0.1701 | 9.9 | 0.1703 | 10.276 | 0.1715 |
| | $w_r$ | 0.8 | | 0.867 | | 0.867 | |
| | $w_m$ | 0.89 | | 0.889 | | 0.885 | |
| | $s_m$ | 0.285 | | 0.076 | | 0.157 | |
| 3rd run | $h_r$ | 10 | 0.1717 | 8.738 | 0.1697 | 9.86 | 0.1719 |
| | $w_r$ | 0.878 | | 0.81 | | 0.873 | |
| | $w_m$ | 0.89 | | 0.788 | | 0.902 | |
| | $s_m$ | 0.193 | | 0.166 | | 0.177 | |

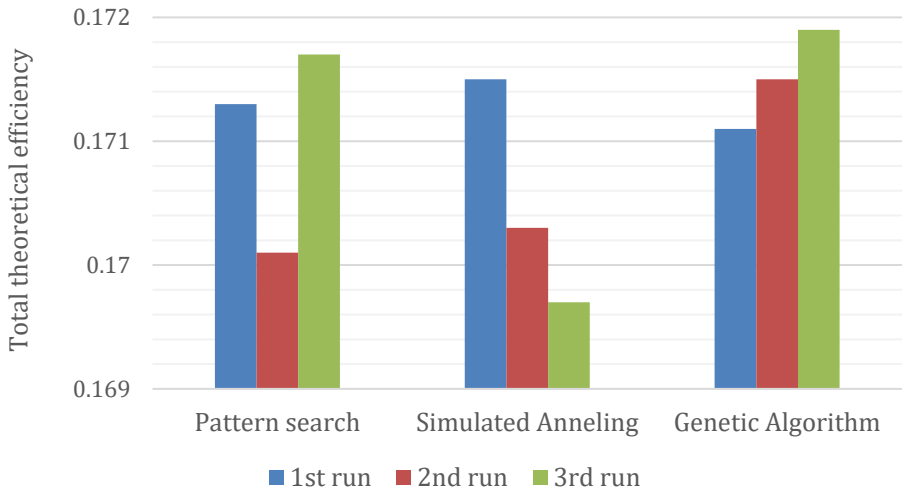


Figure 5.11: Comparison of maximised $\eta_{total,th}$ using three optimization algorithms ($n_m$ =10)

The same process of comparing the exhaustive search and optimized solutions was repeated for a different value range of mirror number, $n_m$ =30 and $n_m$=54 (detailed results are shown in Table Appendix B.6 to Table Appendix B.9), and the results show a similar behaviour to $n_m$ =10. A comparison of the results of these two optimization runs is shown in Figure 5.12. Average simulation times for the three algorithms are shown in Figure 5.13. It can be observed that the three optimization algorithms found better solutions in comparison to the exhaustive search, which was conducted for selected discrete values. This is due to discretising the continuous search space for the exhaustive search. However, this result shows that the three optimization algorithms perform well with manageable computational times.

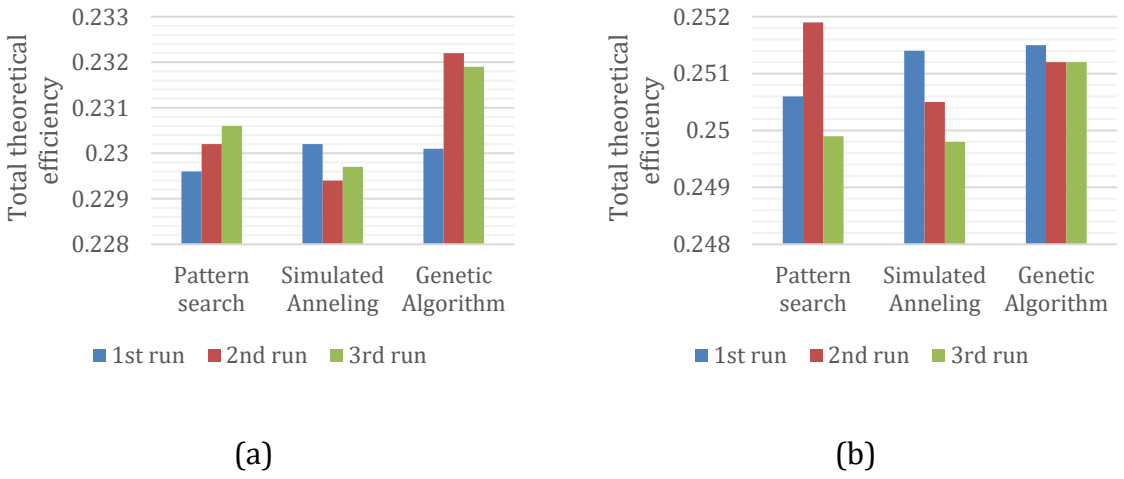


Figure 5.12: A comparison of three optimization algorithms: (a) $n_m$=30; (b) $n_m$=54

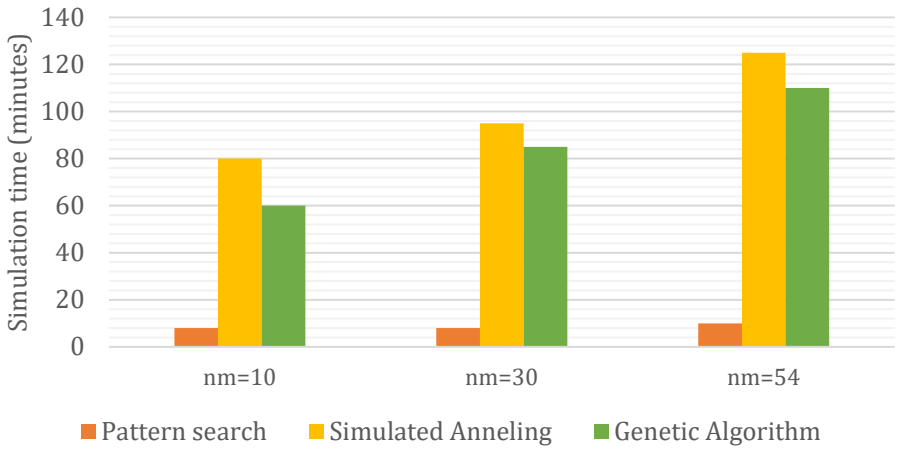


Figure 5.13: Average simulation time for all three optimization algorithms

After considering all the simulation results, it is seen that all three optimization algorithms provided acceptable solutions. The differences between the best and the worst solutions using pattern search, simulated annealing and GA were 0.0012-0.0020, 0.0008-0.0018 and 0.0003-0.0020, respectively. The largest difference found was 0.002, equal to 0.2% of the theoretical efficiency ($\eta_{total,th}$), which is more than enough for many practical applications. Since all algorithms provided acceptable results, the selection of an algorithm for further work can be decided based on the simulation time and the ease of handing the discrete design variable, $n_m$, within the codes.

For the 4D problem of a LFR with a trapezoidal receiver, it is clearly seen that the pattern search is 8-10 times faster than the other two algorithms (Figure 5.13) in terms of computational time. Increasing the simulation time for larger mirror numbers is also significantly lower in comparison. The genetic algorithm seems to be slightly better than simulated annealing taking 10 to 20 minutes less simulation time. However, it is important to note that for population based methods like GA, the initial setup is usually time consuming and adding extra variables is relatively easy.

Although GA was as efficient as pattern search in terms of computational time, there are other benefits for selecting GA for further simulations. In comparison to other algorithms, GA provided the best global maximum in most of the simulations and the solutions were more consistent. In addition to this, there are limitations in implementing the optimization in the Matlab inbuilt toolbox. One of the main limitations is that both continuous and discrete (e.g. mirror number) variables cannot be implemented in most

of the algorithms. However, GA facilitates mixed integer optimization problems. Therefore, GA was selected as the optimization method to be used for further work.

## 5.5 Selecting GA parameters for LFR optimization

After selecting the Genetic Algorithm (GA) to be used for the rest of the work, suitable GA parameters are selected to set up a detailed optimization. Figure 5.14 shows a schematic of an LFR system with slightly curved primary mirrors, PTR®70 receiver tube and CPC combination described in Chapters 4.11.2 and 4.11.3. This is a widely used design in existing power plants and is more optically challenging compared to other LFR designs. Furthermore, this system has been optically and thermally verified in Chapter 4.11. Table 5.8 shows the design variables and constants used to select GA parameters.

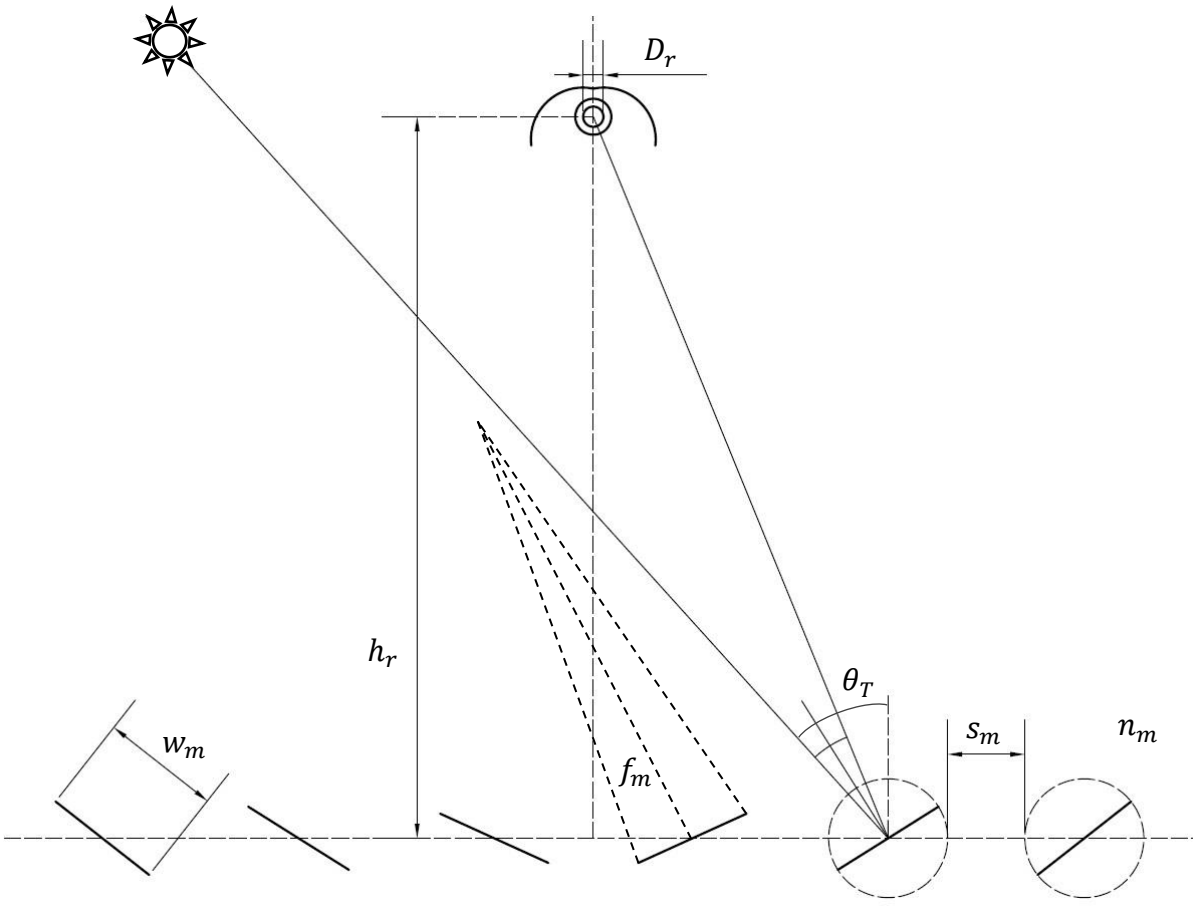


Figure 5.14: A schematic of an LFR system with curved mirrors, CPC and evacuated tube

Table 5.8: Design variables and constants used to select GA parameters for the full problem with five optimization variables

| | |
|---|---|
| Objective function | Total theoretical efficiency($\eta_{total,th}$) |
| Optimization variables | $n_m, w_m, s_m, h_r, T_r$ |
| Bounds | $6 \leq n_m \leq 120$<br>0.05 m $\leq w_m \leq$ 1.2 m<br>0.05 m $\leq s_m \leq$ 1.2 m<br>2 m $\leq h_r \leq$ 30 m<br>$150° \; C \leq T_r \leq 400° \; C$ |
| Constant parameters | |
| DNI | 600 W/m$^2$ (Abbas et al. 2016) |
| Transverse angle ($\theta_T$) | 30° |
| Mirror focal length ($f_m$) | 10.6 m for all mirrors (Qiu et al. 2015) |

GA, categorised under metaheuristics optimization methods, has emerged as an effective optimization technique to determine the global optimum of non-linear problems. GA is an Evolutionary Algorithm (EA), where the evolution of a population is inspired by the mechanisms of biological evolution. GA starts by creating a randomly generated initial population. Then it uses three main mechanisms, selection, cross over and mutation, to create a new generation from the initial population. Selecting suitable values for population size, cross over and mutation parameters support the finding of the global optimum throughout the evolution process. Stopping criteria decide the conditions at which the optimization process should be terminated. In the Matlab GA algorithm, the stopping criteria can be set using a combination of the time limit, generation limit or relative change of the objective function. The most common stopping criteria used are function-tolerance and maximum-stall-generations. In Matlab, these two parameters have been combined to improve the precision of the objective function value (the fitness value).

The proper selection of GA parameters can improve accuracy and save computational time. It is important to note that GA can provide different solutions despite the same settings due to its random generation of individuals (chromosomes) in a population. The selection of the best performing GA parameters highly depends on the problem being addressed. Therefore, the typical approach is to run the optimization for several runs

with different settings for the most significant GA parameters such as population size, cross over and mutation fractions, maximum stall generations and function tolerance (Bastidas-Rodriguez et al. 2017; Hassan et al. 2022). In this study, GA is run 10 times with different population sizes, maximum stall generations (Hassan et al. 2022), and cross over fractions (Bastidas-Rodriguez et al. 2017). These results are indicated in Figure 5.15, Figure 5.16 and Figure 5.17. The figures were generated for a fixed solar radiation level (Bastidas-Rodriguez et al. 2017) by changing one GA parameter at a time while keeping other parameters at default values (Bastidas-Rodriguez et al. 2017; Hassan et al. 2022). Default values for population size, maximum stall generations and cross over fraction are 50, 50 and 0.8 respectively. A function tolerance of $10^{-3}$ was selected for initial simulations to keep the computational time manageable.

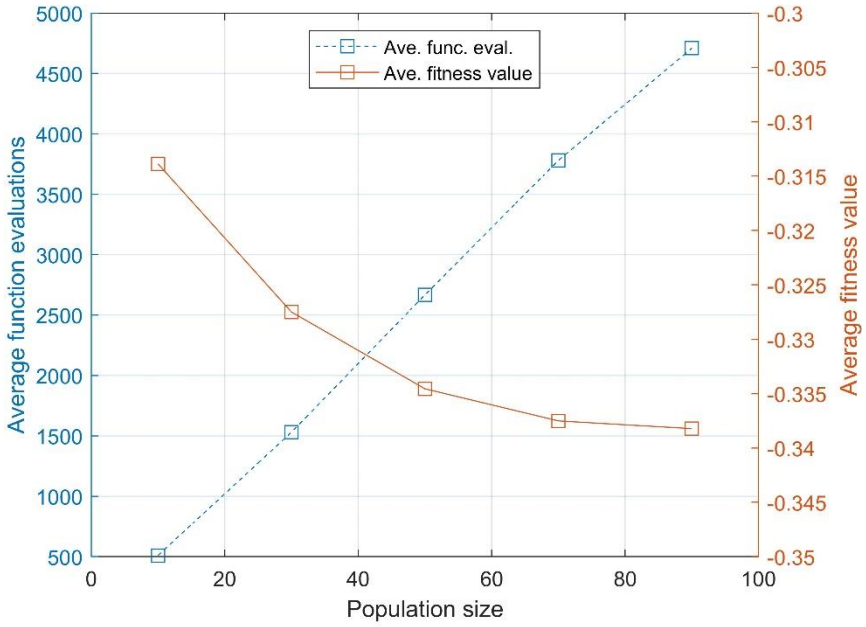


Figure 5.15: Population size vs average function evaluations

According to Figure 5.15, it is seen that the number of function evaluations (also an indication of computational time) is linearly increasing with the population size as expected. However, after about a 50 population size, the rate of improving the accuracy drops while the rate of increasing computational burden remains the same. At a population size of 70, the rate of improving the accuracy is very low. The same trend is seen in Figure 5.16 for stall generations. However, the algorithm has almost found the

best fitness value after 70 stall generations. This suggests that 70 is a suitable number of stall generations to be used for the current problem.

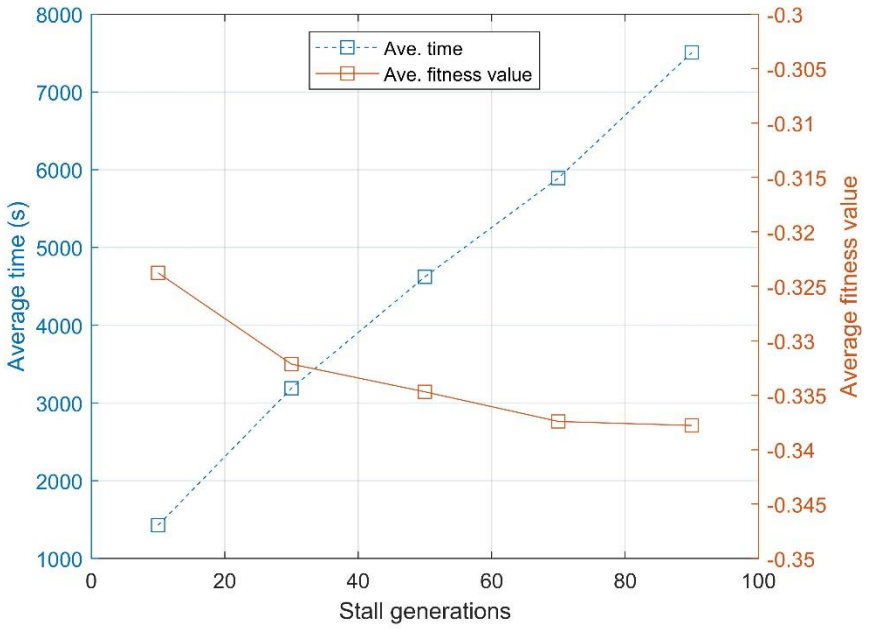


Figure 5.16: Stall generations vs average time

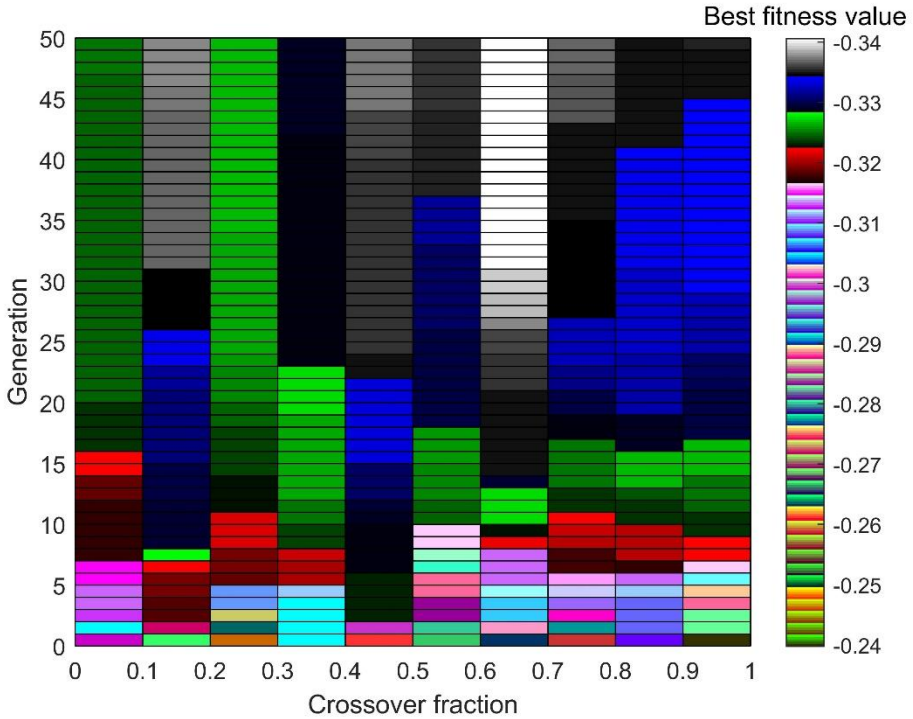


Figure 5.17: Improvement of the best fitness value in each generation for different crossover fractions

Figure 5.17 shows how the best fitness value of each generation changes for different cross over fractions over 50 generations. In the Matlab GA optimization algorithm, the crossover fraction specifies the fraction of each population, except elite children, that are taken to create cross over children. The rest of the population is made up of mutation children. According to the figure, using a crossover fraction of 0.6-0.7 provides the best fitness value. Furthermore, the best fitness value is reached significantly faster, almost after about 30 generations, compared to other cross over fractions.

The optimization results described earlier in this section have been used to select suitable GA parameter values: population size as 70, stall generations as 70 and crossover fraction as 0.65. To check the precession of the best fitness value and convergence of the solution, further optimization simulations were conducted for $10^{-1}$, $10^{-2}$, $10^{-3}$, $10^{-4}$ and $10^{-5}$ function tolerance values. The mean and standard deviation of these simulations were calculated for 10 runs of each "function tolerance" value as given in Table 5.9. Figure 5.18 shows a comparison of the variability of these results in terms of mean and uncertainty (based on one standard deviation from the mean). As seen in the figure, using $10^{-4}$ provides the highest fitness value with an uncertainty of $\pm$ 0.0032. This is equivalent to $\pm$ 0.32 % of the total theoretical efficiency ($\eta_{total,th}$), which can be considered as a very good accuracy. Additionally, a similar "function tolerance" value is also reported in the literature for power and energy optimization of energy systems (Deslauriers et al. 2016; Azad et al. 2021).

Table 5.9: Mean and standard deviation for different function tolerances (based on: 70 population size; 70 stall generations; 0.65 crossover fraction)

| Function tolerance | $10^{-1}$ | $10^{-2}$ | $10^{-3}$ | $10^{-4}$ | $10^{-5}$ |
|---|---|---|---|---|---|
| Mean | -0.33577 | -0.33708 | -0.33305 | -0.33724 | -0.33658 |
| Standard deviation | 0.00274 | 0.00345 | 0.00490 | 0.00318 | 0.00231 |

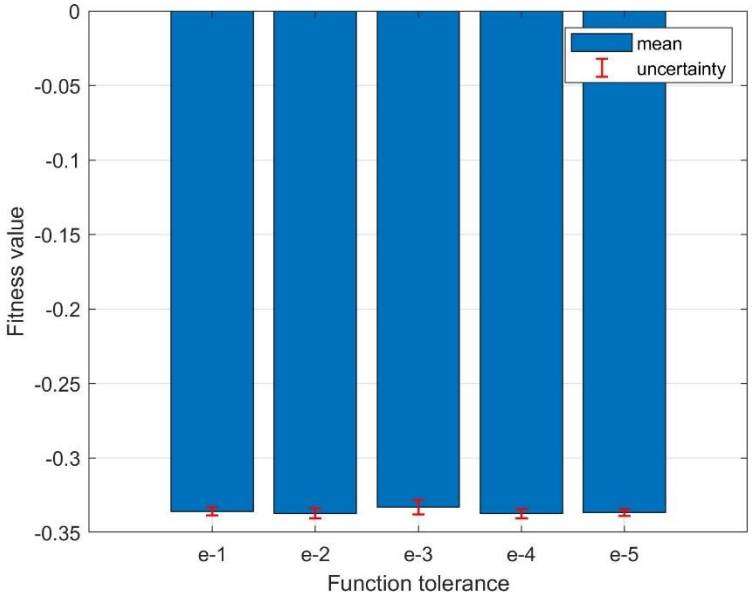


Figure 5.18: A comparison of mean best fitness values with uncertainty

The convergence of the best fitness value using selected GA parameters is shown in Figure 5.19. The best solution is found after about 60 generations and no improvement is made afterwards. Optimization terminates after 85 generations completing about 6000 function evaluations (candidate solutions). Whilst, to the authors' knowledge, no previous studies have used GA for LFR optimization, the trend in convergence is comparable with those reported in the literature for other design optimization problems. The number of generations required to find the best solution can vary from a few generations (Li, Y. et al. 2017) to 30 (Wang, Y. et al. 2011; Hassan et al. 2022) or even more than 100 (Fagan et al. 2017) depending on the problem. However, most studies plot the convergence for 100 or less number of generations (Wang et al. 2011; Li et al. 2017), which is similar to this study.

Table 5.10 summarises the major GA parameters selected for generating detailed optimization results in the next chapter. Although Matlab also provides the flexibility to change these parameters in a more detailed manner, the mixed integer nature of this study only allowed certain options to be used. Other minor parameters were set to defaults where the GA algorithm assigned the best option based on the problem (Debnath, Deb, and Dutta 2013; Deslauriers et al. 2016; Aslambakhsh et al. 2018).

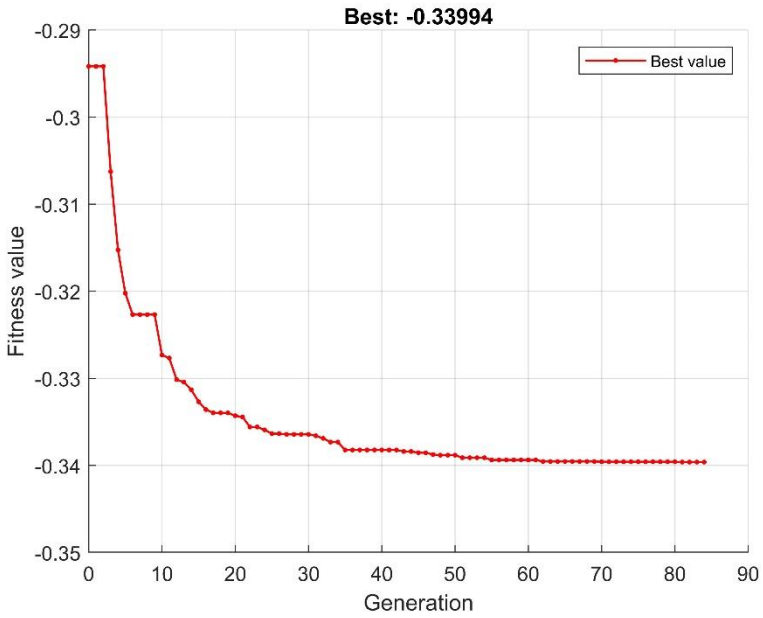


Figure 5.19: Convergence of the best fitness value

Table 5.10: GA parameters selected to be used in further work

| GA parameter | Value/Selection |
|---|---|
| Population type | Double vector |
| Population size | 70 |
| Initial population | Random |
| Scaling function | Rank |
| Selection function | Stochastic uniform |
| Elite count | 2 |
| Mutation function | Constraint dependent |
| Crossover fraction | 0.65 |
| Crossover function | Constraint dependant |
| Stall generations | 70 |
| Function tolerance | e-4 |

## 5.6 Summary

Optimization methods for LFR design have been evaluated along with their accuracy, limitations and computational times. Moreover, GA was selected as the best optimization method for this study and a GA parameter setting that provides an acceptable confidence level for the optimization problem was established. The optimization problem was initially formulated with: total theoretical efficiency and LCOE as the objective functions; number of mirrors, mirror width, mirror spacing, receiver width, receiver height and temperature as design variables; relevant constraints and bounds. The formulated problem was implemented on one design variable using three derivative-based optimization methods, which were found to be not suitable for the current study. Consequently, two derivative-free methods were tested and showed better results. Furthermore, the two global optimization methods tested showed excellent results in identifying near-optimum solutions. Following this result, multiple design variables were tested using three selected algorithms, pattern search, GA and simulated annealing, and GA was selected for further work considering its advantages over the other methods. The complete optimization problem consisting of both discrete and continuous design variables, CPC and evacuated tube receiver was implemented on GA. Following a large number of optimization simulations, suitable GA parameters were established to provide a convergence of the solution with acceptable uncertainty, 0.32 % of the total theoretical efficiency (standard deviation of 0.0032). The GA parameters established were used to generate detailed results for performance and cost based optimization of LFR, described in the next chapter.

# 6

# Performance and cost based optimization of an LFR

## 6.1 Introduction

The objective of this chapter is to answer the second and third research questions mentioned in Chapter 1: how do different parameters (mirror types/operating temperatures/locations) and requirements (maximising performance/minimising energy costs) influence optimal LFR designs? (Research question 2), and how sensitive are the optimal LFR designs to potential changes in costs and design variables? (Research question 3). Initially, LFR mirror and receiver configurations selected to answer the research questions are shown along with modelling parameters. Optimization of the performance-based objective function is then discussed for two receiver temperature operating conditions and three mirror types. Optimized results are compared against other available optimization studies to see the similarity or differences of the methods suggested in this study. Subsequently, optimization of the cost-based objective function, LCOE, is carried out for actual weather data in Spain, China and Australia. The effects of installing the optimized designs in other locations are explored. The sensitivity of the design variables and potential changes in costs are then further examined. The chapter concludes by evaluating the assumptions made and how the results of the performance and cost based optimization work can be used to improve future LFR designs.

## 6.2 LFR configurations and model parameters used

Although different receiver designs exist (Bellos 2019), a single-tube receiver with a secondary Compound Parabolic Concentrator (CPC) is considered in this section to answer the research questions, as it is the most established type in commercial and prototype LFR power plants, such as Puerto Errado, Fresdemo and Augustin Fresnel

(Montes et al. 2014; Islam et al. 2018). This receiver uses the SCHOTT PTR®70, currently known as RIOGLASS PTR®70-4G (RIOGLASS Solar 2020), which is a common off-the-shelf component used in these types of systems. The design of the CPC is taken from Chaitanya Prasad, Reddy, and Sundararajan (2017), which has been used in several other studies (see Chapters 4.11.2 and 4.11.3 for more detail). A schematic of the CPC design and modelled receiver using SolTrace is shown in Figure 6.1. Geometrical, optical and thermal parameters used to model the receiver is shown in Table 6.1.

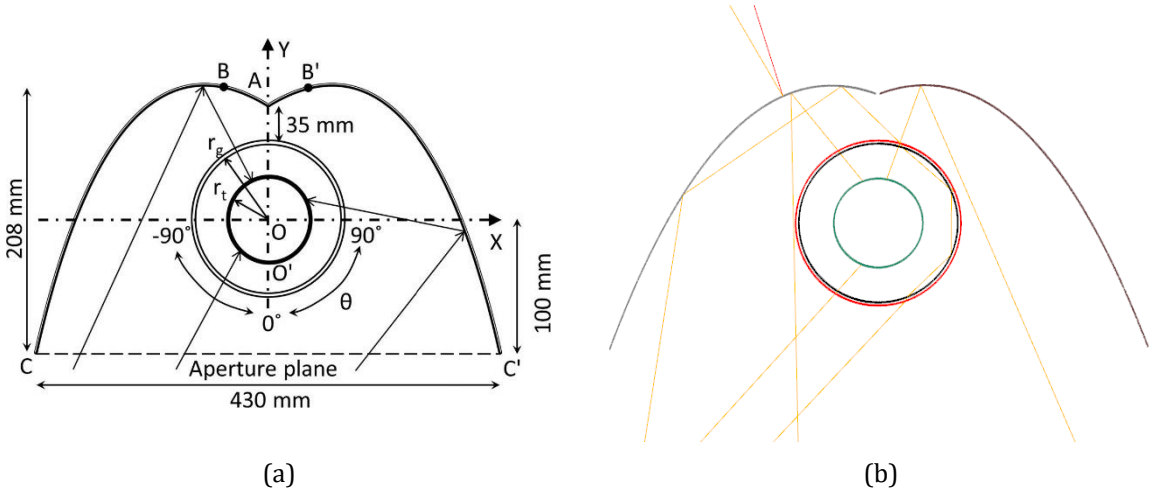


(a) (b)

Figure 6.1: LFR receiver modelled: (a) A schematic (not to scale) of the CPC design used, Reprinted from Chaitanya Prasad, Reddy, and Sundararajan (2017), Copyright (2017), with permission from Elsevier (b) The same CPC and PTR®70 receiver tube modelled in SolTrace showing the interaction of five rays

Table 6.1: Various modelling parameters used (SCHOTT solar 2013; Chaitanya Prasad, Reddy, and Sundararajan 2017)

| | |
|---|---|
| Emissivity of absorber tube | $\varepsilon_r = 0.095$ |
| Diameter of absorber tube | $D_r = 0.07\ m$ |
| Emissivity of glass cover | $\varepsilon_c = 0.9$ |
| Diameter of glass cover | $D_c = 0.125\ m$ |
| Transmissivity of glass cover | 0.97 |
| Refractive index for glass cover | 1.5 |
| Focal length of CPC's parabola | 45 mm |
| Transmissivity of primary mirrors | 0 |
| Ambient temperature | $T_a = 30°C$ |

Figure 6.2 shows a schematic diagram of the geometrical design variables and other important parameters changed in the optimization process. Transverse angle ($\theta_T$) is changed during different hours of operation in a given day as given in section 6.3.1. In addition to this, the longitudinal angle ($\theta_L$) is also changed as described in section 6.4.1. Based on mirror types (flat, slightly curved and fully curved), the mirror focal length ($f_m$) is changed as given in Chapter 4.5.3. In the case of slightly curved mirrors, the focal length is fixed at 10.6 m (Qiu et al. 2015; López-Alvarez et al. 2020). The absorber tube diameter ($D_r$) depends on the receiver used and is fixed based on the PTR®70 (SCHOTT solar 2013).

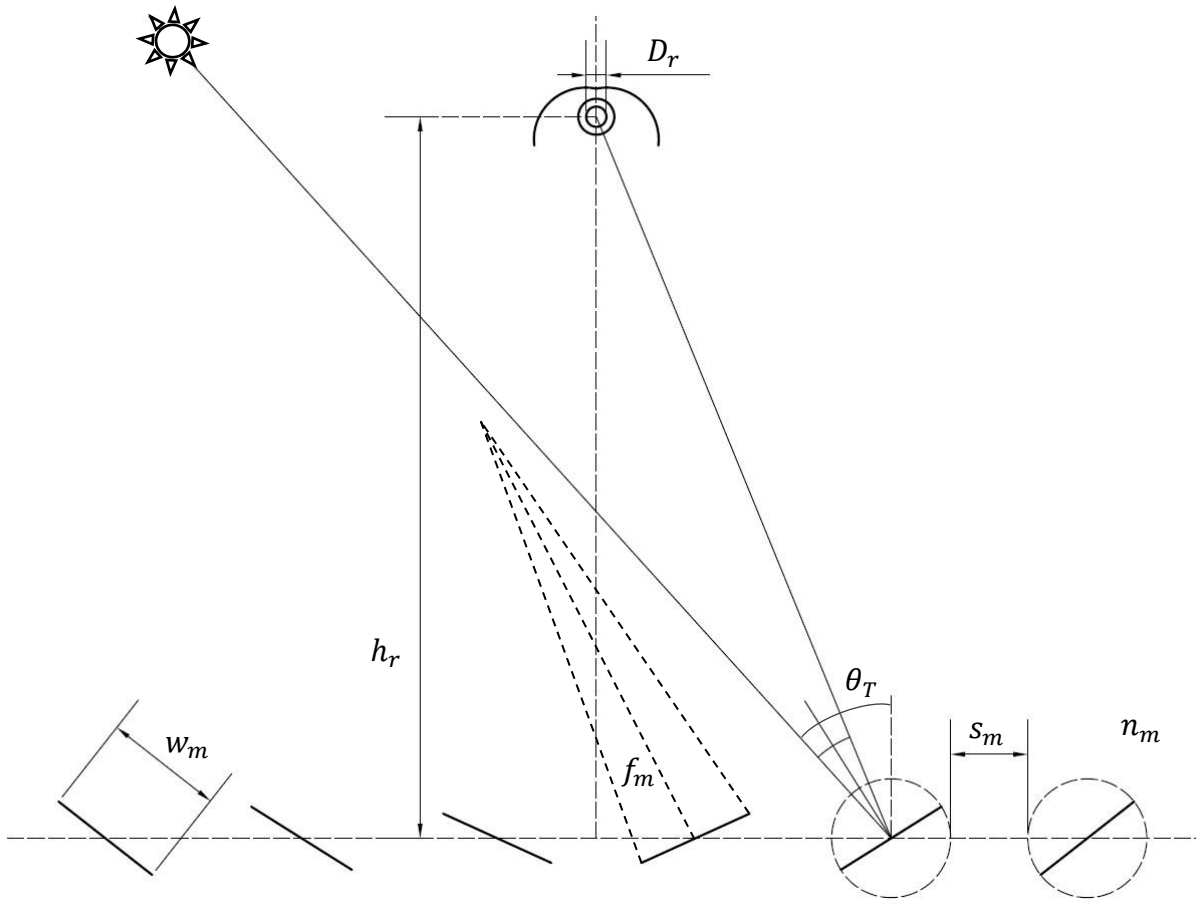


Figure 6.2: A schematic diagram of the geometrical design variables and other important parameters changed for optimization

Several modelling parameters are used to evaluate the optimized LFR systems using the Rankine cycle to support the performance and LCOE based results. The high pressure side

of the Rankine cycle is taken as 55 bar as several other CSP power plants such as Puerto Errado (NREL 2021). As these power plants use dry cooling, a significant temperature difference (30-50 Fahrenheit) is needed compared to ambient air (U.S. Department of Energy 2010). Therefore, a condenser temperature is selected at around 60°C (Han et al. 2021) by taking the condenser pressure as 20 kPA (U.S. Department of Energy 2010). The combined efficiency of the gearbox and generator is taken as 95% (Astolfi, Martelli, and Pierobon 2017; Arabkoohsar 2020) and the fraction of auxiliary power needed to run the power plant is assumed to be not significant.

Additional parameters are used to compare the optimized designs: concentration ratio and land area. Optical concentration ratio ($CR_{optical}$) is defined as the ratio of solar flux entering the collector to solar flux received by the absorber. Geometrical concentration ratio ($CR_{geometrical}$) is defined as the ratio of the entrance aperture area to the receiver area (Kandpal and Mathur 1985; Zheng 2017).

$$CR_{optical} = \frac{I_r}{DNI} \tag{6.1}$$

$$CR_{geometrical} = \frac{A_m}{A_r} \tag{6.2}$$

The total area of all mirrors is found using equation (6.3) and the land area occupied by the collector is calculated using equation (6.4). These parameters have been expressed per meter length of the plant.

$$A_m = w_m n_m \tag{6.3}$$

$$A_L = (w_m + s_m)(n_m - 1) + w_m \tag{6.4}$$

## 6.3 Performance-based optimization

### 6.3.1 Problem description, modelling scenarios and parameters

The objective function used for the performance-based optimization was total theoretical efficiency of power generation ($\eta_{total,th}$). The formulation of the optimization problem is shown in Chapter 5.3 for the two receiver temperature operating conditions used; the upper and lower bounds of the design variables are shown in section 6.3.2. Nine scenarios were formed when the two operating conditions, two maximum receiver temperature limits and three mirror types were combined. Therefore, to avoid excessive computational times, the longitudinal plane of the LFR system was not considered (Sánchez, Clifford, and Nixon 2018; Roostaee and Ameri 2019) such that the daily and annual variations of solar irradiance and angles only occur in the transversal plane. Furthermore, changes in the daily variation in sun position and irradiance were approximated considering the number of daylight hours at five sun positions (see Table 6.2 ).

Table 6.2: Solar radiation profile used for performance-based optimization

| transverse angle ($\theta_T$) (deg.) | Solar irradiance (W/m$^2$) | Number of hours of sunshine |
|---|---|---|
| -60 | 300 | 2 |
| -30 | 600 | 2 |
| 0 | 700 | 1 |
| +30 | 600 | 2 |
| +60 | 300 | 2 |

### 6.3.2 Variable bounds

Table 6.3 shows the variable bounds used for the optimization. Furthermore, two $T_{lim}$ values were assumed for a variable temperature operating condition. The SCHOTT PTR®70 has been designed to withstand temperatures up to 400°C (SCHOTT solar 2013). A lower temperature limit of 250°C was also used to check how the system would perform when limited for lower temperature applications.

Table 6.3: Variable bounds used in the optimization

| Design variable | Lower bound ($x_{min}$) | Upper bound ($x_{max}$) |
|---|---|---|
| $h_r$(m) | 2 | 30 |
| $n_m$[a] | 6 | 200 |
| $w_m$(m) | 0.05 | 1.2 |
| $s_m$(m) | 0.05 | 1.5 |
| $T_r$(°C)[b] | 200 | 400 |

[a] note that the number of mirrors is a discreet variable whereas the others are continuous

[b] $T_r$ become a dependant variable with 250°C and 400°C maximum limits under variable receiver temperature operating condition

### 6.3.3 Optimization results

Optimized results for the different primary mirrors (flat, slightly curved and fully curved) under the constant temperature operating condition (see Chapter 5.3) show that all three mirror types can achieve a similar performance, expressed in terms of total theoretical efficiency. However, the resulting design variables and power outputs are significantly different. Table 6.4 shows that a maximum total efficiency of 30.2% can be obtained using fully curved mirrors, which is only slightly higher than the 28.9% value achieved by employing flat mirrors. The optimized design variables were significantly different, especially mirror widths and the number of mirrors, to achieve these efficiency values. An LFR with fully curved mirrors benefits from reduced receiver height and mirror number by utilising wider mirrors and gaps. When fully curved mirrors are used, a 35% and 29% reduction in land and mirror area is achieved in comparison to an LFR with flat mirrors, which could significantly reduce system costs. An LFR using slightly curved mirrors provides a compromise between flat and curved configurations for all design variables. The optimized design for each configuration is shown to scale in Figure 6.3. Interestingly, the power output of the curved mirrors is the lowest even if the efficiency is the highest. This is also reflected in optical and geometrical concentration ratios showing lower values. The results highlight that an optimized fully curved mirror system results in an efficient and compact design, whereas an optimized flat mirror LFR results in a larger less efficient system.

Table 6.4: Optimized results for considering total theoretical efficiency of power generation for three primary mirror types and five design variables

| Primary mirror type | | Fully curved | Slightly curved | Flat |
|---|---|---|---|---|
| Objective function maximized | $\eta_{total,th}$ | 0.3017 | 0.2970 | 0.2887 |
| Optimized design variables | $h_r$(m) | 3.260 | 3.920 | 4.958 |
| | $n_m$ | 24 | 60 | 78 |
| | $w_m$(m) | 0.1562 | 0.0762 | 0.0677 |
| | $s_m$(m) | 0.1017 | 0.0578 | 0.0535 |
| | $T_r$(°C) | 363 | 371 | 388 |
| Other parameters | Power output (kWh/m/d) | 4.5 | 5.6 | 6.3 |
| | $CR_{optical}$ | 10.0-11.4 | 12-13.5 | 13.4-15.1 |
| | $CR_{geometrical}$ | 17.0 | 20.8 | 24 |
| | $A_m$(m$^2$) | 3.75 | 4.57 | 5.28 |
| | $A_L$(m$^2$) | 6.09 | 7.98 | 9.52 |

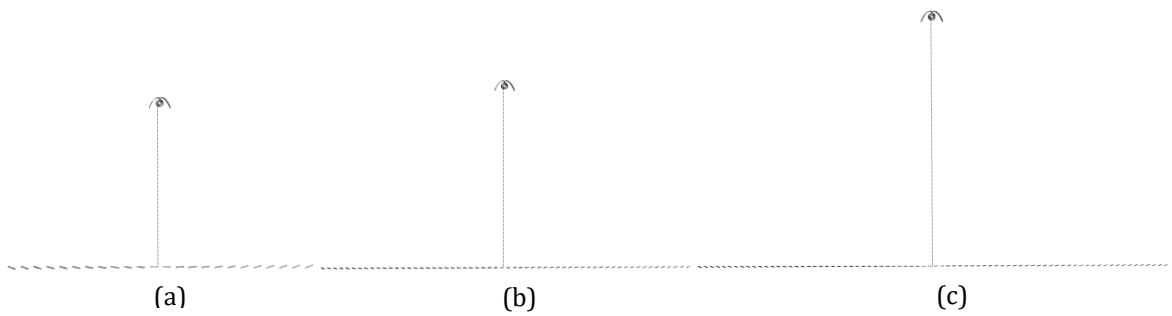


Figure 6.3: Optimized LFR designs using (a) fully curved, (b) slightly curved, and (c) flat mirrors

The optimized receiver temperature was nearly the same for all configurations (around 360 – 390 °C), which is below the maximum possible temperature of the PTR®70. As LFR systems have been deployed for a range of applications, at different operational temperatures, the influence of a targeted operational temperature on the optimized design was modelled by considering temperatures of <400°C or <250°C. Results from the two variable temperature limits for the three mirror configurations, fully curved, slightly curved and flat, are shown in Table 6.5-Table 6.7. Limiting the temperature to a maximum

value of 400°C resulted in a similar performance being achieved, which is to be expected as the optimized temperatures were close to 400°C. Enabling an optimum temperature for different times of the day, up to a maximum limit of 250°C, reduced the total theoretical efficiency to 24.9% for a flat mirror configuration. This is a 13.6% decrease compared to a constant optimized temperature of 388°C. However, limiting the operating temperature to 250°C also significantly reduced the mirror aperture area and land area. The cost savings on the mirror elements, tracking mechanisms and structural requirements could therefore make smaller less efficient systems for lower power applications more attractive.

Table 6.5: Optimized results for an LFR using fully curved mirrors operating with different receiver temperature limits: 250°C and 400°C

| Temperature limit | $T_r$ (°C) | $\leq 250$ | $\leq 400$ |
|---|---|---|---|
| Objective function maximized | $\eta_{total,th}$ | 0.2826 | 0.3065 |
| Optimized design variables | $h_r$(m) | 2.341 | 2.645 |
| | $n_m$ | 38 | 44 |
| | $w_m$(m) | 0.0666 | 0.0838 |
| | $s_m$(m) | 0.0574 | 0.0504 |
| Other parameters | Power output (kWh/m/d) | 2.8 | 4.5 |
| | $CR_{optical}$ | 7.5-8.0 | 9.8-11.5 |
| | $CR_{geometrical}$ | 11.5 | 16.8 |
| | $A_m$(m$^2$) | 2.53 | 3.69 |
| | $A_L$(m$^2$) | 4.65 | 5.85 |

Table 6.6: Optimized results for an LFR using slightly curved mirrors operating with different receiver temperature limits: 250°C and 400°C

| Temperature limit | $T_r$ (°C) | ≤ 250 | ≤ 400 |
|---|---|---|---|
| Objective function maximized | $\eta_{total,th}$ | 0.2788 | 0.2996 |
| Optimized design variables | $h_r$(m) | 2.004 | 2.109 |
| | $n_m$ | 56 | 62 |
| | $w_m$(m) | 0.0500 | 0.0599 |
| | $s_m$(m) | 0.0503 | 0.0501 |
| Other parameters | Power output (kWh/m/d) | 3.0 | 4.4 |
| | $CR_{optical}$ | 8.2-8.7 | 9.9-11.1 |
| | $CR_{geometrical}$ | 12.7 | 16.9 |
| | $A_m$(m²) | 2.8 | 3.71 |
| | $A_L$(m²) | 5.57 | 6.76 |

Table 6.7: Optimized results for an LFR using flat mirrors operating with different receiver temperature limits: 250°C and 400°C

| Temperature limit | $T_r$ (°C) | ≤ 250 | ≤ 400 |
|---|---|---|---|
| Objective function maximized | $\eta_{total,th}$ | 0.2493 | 0.2792 |
| Optimized design variables | $h_r$(m) | 4.396 | 5.505 |
| | $n_m$ | 36 | 60 |
| | $w_m$(m) | 0.1004 | 0.1045 |
| | $s_m$(m) | 0.0566 | 0.0581 |
| Other parameters | Power output (kWh/m/d) | 3.5 | 7.3 |
| | $CR_{optical}$ | 8.8-10.2 | 14.2-17.4 |
| | $CR_{geometrical}$ | 16.4 | 28.5 |
| | $A_m$(m²) | 3.61 | 6.27 |
| | $A_L$(m²) | 5.60 | 9.65 |

A comparison of the two receiver temperature operating conditions is explicitly shown in Table 6.8. In the first operating condition, a constant receiver temperature was maintained in the system. In the second operating condition (variable), the receiver temperature was allowed to change at an optimum value (see Chapter 5.3), not exceeding a maximum possible limit demanded by the receiver material and application. Although

it was expected that the variable receiver temperature condition would provide a higher efficiency compared to the constant condition as it can maintain an optimum temperature at all times, the difference observed was negligible. Therefore, the selection of the best operating condition can be solely based on practical considerations. Since designing a system for a fixed receiver temperature is much more convenient, a constant receiver temperature is likely to be the preferable alternative in most situations.

Table 6.8: A comparison of $\eta_{total,th}$ for constant and variable receiver temperature operating conditions

| Operating condition | Optimized/ maintained $T_r$ ($^{o}$C) | Fully curved | Slightly curved | Flat |
|---|---|---|---|---|
| Constant | 360 – 390 | 0.3017 | 0.2970 | 0.2887 |
| Variable | $\leq 400$ | 0.3065 | 0.2996 | 0.2792 |
| | $\leq 250$ | 0.2826 | 0.2788 | 0.2493 |

Both fully curved and slightly curved mirror configurations improve collector efficiencies and reduce receiver heights, and land and mirror area requirements (Figure 6.4 and Figure 6.5). Figure 6.4 compares changes in the optimized results of curved and slightly curved mirror configurations in comparison to flat mirrors; results are shown for the constant receiver temperature operating condition. Fully curved and slightly curved mirrors increased the total theoretical efficiency by 4.5% and 2.9%, respectively, and decreased the receiver height, mirror area and land area at least by 29% and 13%. Figure 6.5 shows the same results based on fully curved mirrors and indicates that flat mirrors are not attractive compared to curved mirrors unless a significant cost saving can be achieved due to not having a curvature. The influence of cost savings due to different mirror curvatures has to be identified by a cost-based objective function. As a slightly curved mirror design uses mirrors that all have the same curvature, a fully curved mirror design will only be preferable if the cost savings from reduced land coverage and mirror element driving mechanisms outweigh the additional cost and complexity of using curved mirrors with high manufacturing and replacement costs.

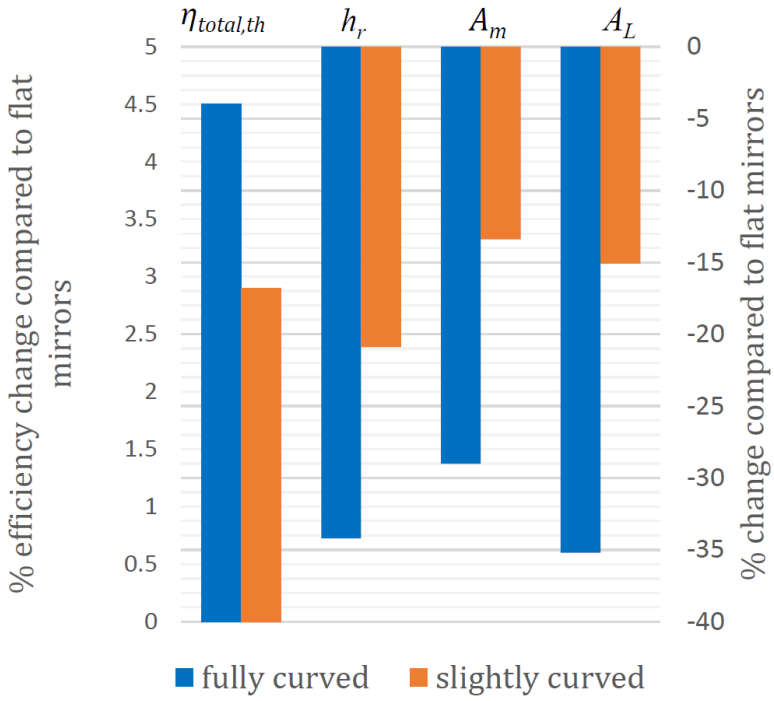


Figure 6.4: A comparison of fully curved and slightly curved mirror designs with a flat mirror design taken as a base case

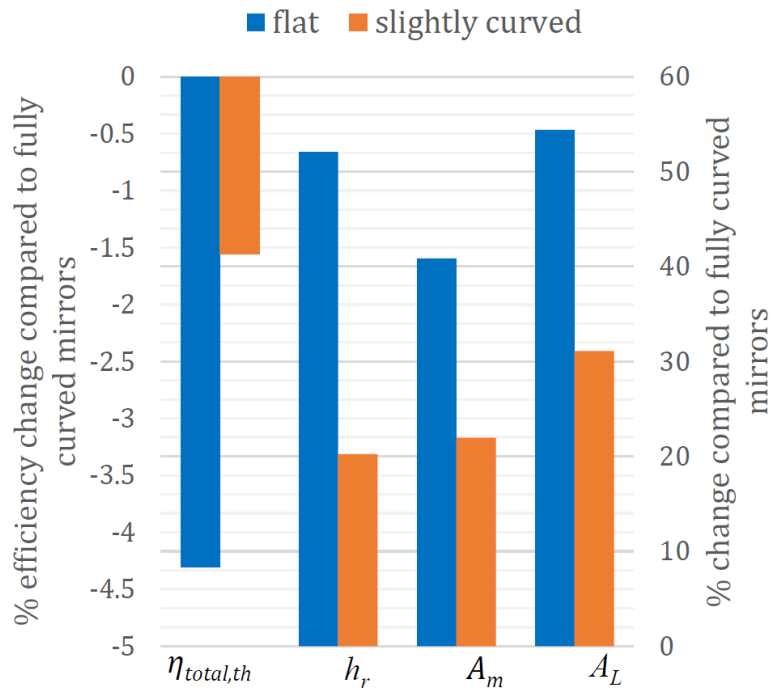


Figure 6.5: A comparison of flat and slightly curved mirror designs with a fully curved mirror design taken as a base case

The ratio between the power generation potential and solar input power ($\eta_{total}$) was evaluated considering the ideal Rankine cycle in addition to the Carnot cycle as seen in Table 6.9. As the Carnot cycle provides a theoretical maximum, $\eta_{total,th}$ is conversably higher than $\eta_{total}$ given by coupling the Rankine cycle as expected. Plant peak efficiency in actual LFR power plants is reported as around 18% (Liu et al. 2016; Islam et al. 2018) showing a good agreement with the Rankine cycle based calculations. However, it is important to note that this comparison has been made assuming optimized LFR design parameters in this work would not change considerably under a Rankine cycle based LFR optimization.

Table 6.9: A comparison of solar energy conversion rates under Carnot and Rankine cycles

| | Fully curved | Slightly curved | Flat |
|---|---|---|---|
| Optimized $T_r$ (°C) | 363 | 371 | 388 |
| $\eta_{total,th}$ (Carnot) | 0.3017 | 0.2970 | 0.2887 |
| $\eta_{total}$ (Rankine) | 0.1859 | 0.1815 | 0.1737 |

### 6.3.4 Sensitivity analysis of design variables

A sensitivity analysis was carried out to identify the effects of design variables on the total theoretical efficiency when the variables were at non-optimal values. The analysis was performed by changing one variable at a time while keeping all other variables at the identified optimum values detailed in Table 6.4. The results have been categorised based on mirror types (Figure 6.6) and design variables (Figure 6.7) for ease of comparison.

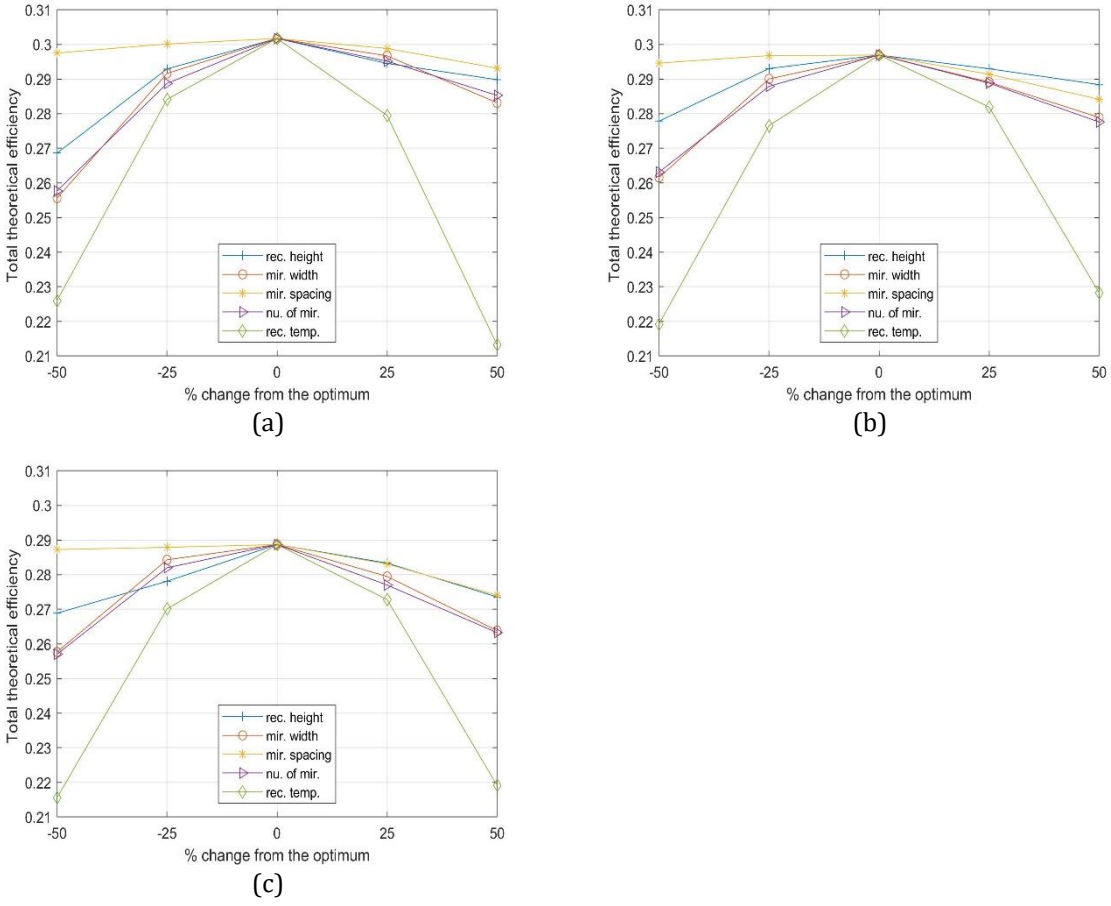


Figure 6.6: Sensitivity of number of mirrors($n_m$), receiver height($h_r$), mirror width($w_m$), mirror spacing($s_m$), receiver temperature($T_r$) for: (a) fully curved mirrors, (b) slightly curved mirrors, (c) flat mirrors

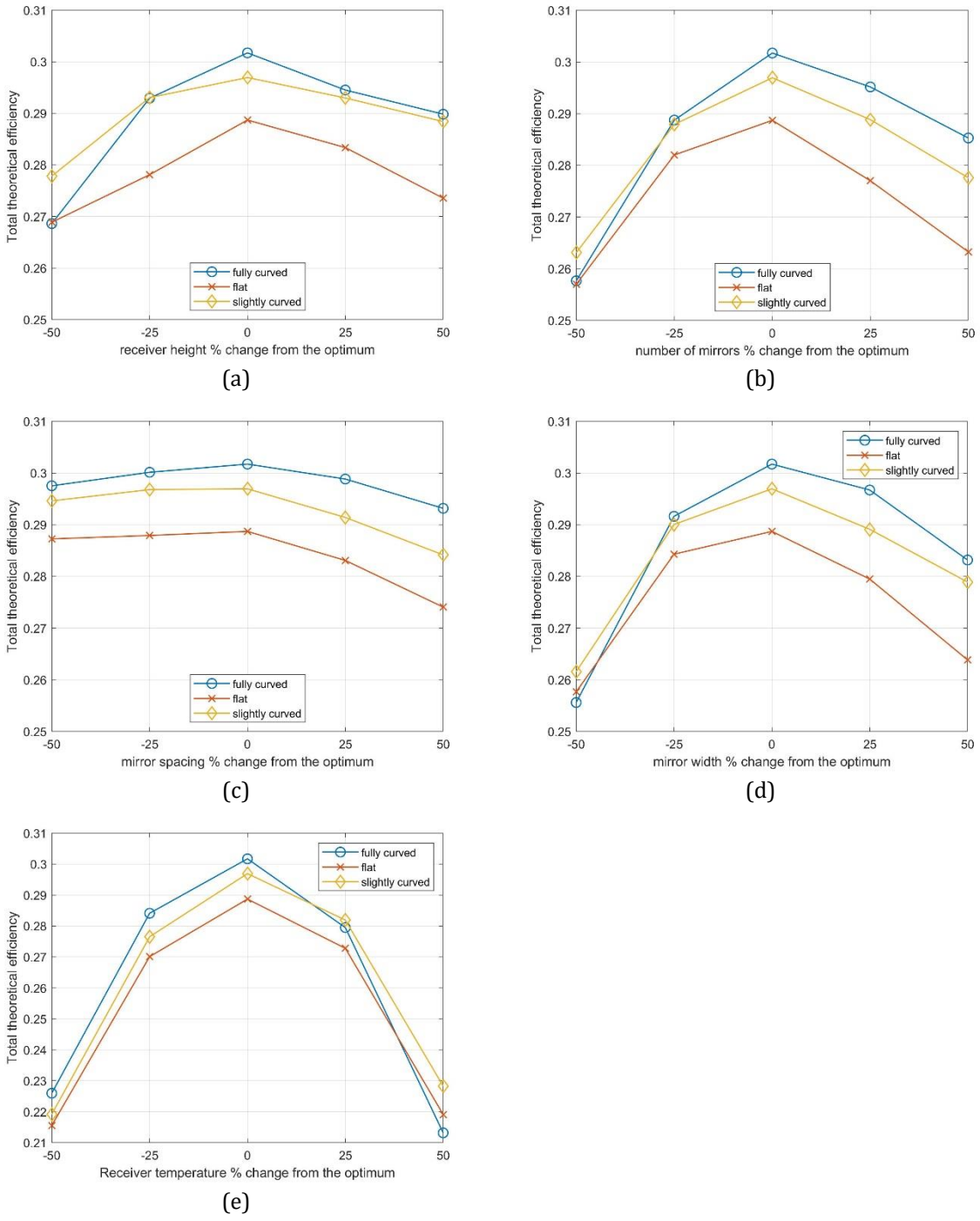


Figure 6.7: Sensitivity of fully curved, slightly curved and flat mirrors for each of the design variable: (a) receiver height($h_r$), (b) number of mirrors($n_m$), (c) mirror spacing($s_m$), (d) mirror width($w_m$), (e) receiver temperature($T_r$)

Regardless of the mirror configuration, an LFR's performance has a low sensitivity to mirror spacing and high sensitivity to deviations from the ideal operating temperature. A 50% increase or decrease in the target temperature would decrease the total efficiency from around 30% to 21% for all three mirror configurations. In comparison, the total

efficiency only drops to around 27.5-29.5% when the mirror spacing is increased by 50%. A decrease of 50% in the mirror spacing is negligible suggesting that blocking and shading of adjacent rows is not significant within the design variable ranges considered in the sensitivity analysis. Thus, increasing the mirror spacing has a much higher sensitivity than decreasing it. The same behaviour can be observed with the number of mirrors and mirror width, shown more clearly in Figure 6.7. Furthermore, different mirror configurations have a clear effect on these two design variables, especially at higher off-optimal values. Receiver height has a high sensitivity for decreasing values from the optimum, as blocking and shading start to have a greater effect. Thus, designing LFRs around the receiver temperature is critical, while mirror number, width and receiver height should be given greater priority than mirror spacing requirements.

## 6.4 Cost-based optimization

This section explores a cost objective function based on LCOE and installation of LFR systems in different locations. Whereas the mirror types were compared using a performance-based objective function with ray angle changes in only the transversal plane, the model is extended to incorporate longitudinal changes based on the Incident Angle Modifier, described in Chapter 4.3. Formulation of the optimization problem for LCOE is defined in Chapter 5.3. The optimization model has been applied to an LFR design using slightly curved mirrors as this mirror type is typical for commercial systems. As a power block is usually designed to run at a fixed temperature, the receiver temperature was assumed to be fixed at 300°C based on existing LFR designs (NREL 2021). Other than this temperature, the same variable bounds mentioned in section 6.3.2 were used for the optimization.

### 6.4.1 Case study locations and weather data

Weather data for Spain, China and Australia, taken from TMY data sets (EU Science Hub 2019), have been used to compare optimized results for different locations. Direct Normal solar Irradiance (DNI) is the most significant weather data that affects the CSP system design. In simulations, which require annual insolation data, it is common to consider a selected day of a month to avoid excessive computational time. Four days were selected for this work, two equinoxes and two solstices, to represent the annual variation

of the solar radiation profile (Li et al. 2018; Xie et al. 2021). Based on hourly TMY data, changes in the daily variation in the sun's position were approximated considering the number of daylight hours at five sun positions (see Table 6.10). Table 6.11 shows the averaged DNI values around the five sun positions for the equinox and solstice dates at Plataforma Solar de Almería(PSA) (37.0947° N, 2.3584° W), Spain. Solar radiation profiles considered for Dunhuang, China (40.084° N, 94.421° E) and Perth, Australia (32.376° S 115.980° E) are shown in Table 6.12. Transverse and longitudinal angles were calculated based on solar altitude and azimuth angles as described by Morin et al. (2012).

Table 6.10: Solar radiation profile used for the cost-based optimization model

| Transverse angle($\theta_T$)(deg.) | Number of sunshine hours in summer months | Number of sunshine hours in winter months |
|---|---|---|
| -60 | 2 | 2 |
| -30 | 3 | 2 |
| 0 | 1 | 1 |
| +30 | 3 | 2 |
| +60 | 2 | 2 |

Table 6.11: Annual solar radiation profile for Spain based on hourly TMY data for PSA

| Date | Transverse angle ($\theta_T$) (deg.)[a] | Longitudinal angle ($\theta_L$) (deg.)[b] | DNI(W/m$^2$) |
|---|---|---|---|
| 21st of March | 0 | -31 | 950 |
| | 30 | -28 | 759 |
| | 60 | -18 | 620 |
| 21st of June | 0 | -13 | 882 |
| | 30 | -8 | 821 |
| | 60 | 8 | 607 |
| 21st of September | 0 | -31 | 663 |
| | 30 | -27 | 158 |
| | 60 | -16 | 249 |
| 21st of December | 0 | -41 | 863 |
| | 30 | -40 | 849 |
| | 60 | -36 | 435 |

[a]change of the longitudinal angle is symmetric around zero transverse angle assuming an LFR is aligned to a north-south axis; [b]usual sign convention applies (angles measured towards north is positive)

Table 6.12: Annual solar radiation profiles for Dunhuang, China and Perth, Australia

| | | Dunhuang, China | | Perth, Australia | |
|---|---|---|---|---|---|
| Date | Transverse angle ($\theta_T$) (deg.)[c] | Longitudinal angle ($\theta_L$) (deg.)[d] | DNI(W/m$^2$) | Longitudinal angle ($\theta_L$) (deg.)[d] | DNI(W/m$^2$) |
| 21st of March | 0 | -32 | 932 | 28 | 960 |
| | 30 | -29 | 874 | 26 | 818 |
| | 60 | -18 | 579 | 17 | 526 |
| 21st of June | 0 | -16 | 803 | 40 | 756 |
| | 30 | -10 | 810 | 38 | 599 |
| | 60 | -6 | 573 | 35 | 250 |
| 21st of September | 0 | -32 | 802 | 28 | 891 |
| | 30 | -30 | 765 | 25 | 774 |
| | 60 | -20 | 510 | 16 | 711 |
| 21st of December | 0 | -42 | 622 | 9 | 992 |
| | 30 | -41 | 692 | 4 | 979 |
| | 60 | -38 | 392 | -10 | 820 |

[c]change of the longitudinal angle is symmetric around zero transverse angle assuming an LFR is aligned to a north-south axis; [d]usual sign convention applies (angles measured towards north is positive)

Following the optimization conducted for selected transverse angles and the number of hours per day, a detailed evaluation for 365 days was conducted on the optimized systems. Table 6.13 shows hourly transverse and longitudinal angles for a selected day in PSA, Spain. The same angles were calculated for all 356 days and the other locations in China and Australia using TMY data. Hourly solar geometry calculations were carried out using a solar calculator available at Global Monitoring Laboratory (2021).

Table 6.13: Solar radiation profile based on hourly TMY data for PSA, Spain for the 1st of July

| UTC (Coordinated Universal Time) | Transverse angle ($\theta_T$) (deg.)[e] | Longitudinal angle ($\theta_L$) (deg.)[e] | DNI($W/m^2$) |
|---|---|---|---|
| 0000 | NA | NA | 0 |
| 0100 | NA | NA | 0 |
| 0200 | NA | NA | 0 |
| 0300 | NA | NA | 0 |
| 0400 | NA | NA | 0 |
| 0500 | NA | NA | 0 |
| 0600 | -78.1 | 19.1 | 428 |
| 0700 | -66.9 | 11.4 | 600 |
| 0800 | -55.5 | 3.7 | 745 |
| 0900 | -43.5 | -3.2 | 818 |
| 1000 | -30.8 | -8.5 | 864 |
| 1100 | -17.2 | -12 | 889 |
| 1200 | -3.2 | -13.5 | 913 |
| 1300 | 11 | -12.9 | 890 |
| 1400 | 24.8 | -10.3 | 852 |
| 1500 | 37.9 | -5.8 | 823 |
| 1600 | 50.2 | 0.5 | 741 |
| 1700 | 61.8 | 7.9 | 635 |
| 1800 | 73.1 | 15.7 | 458 |
| 1900 | 84.4 | 23 | 142 |
| 2000 | NA | NA | 0 |
| 2100 | NA | NA | 0 |
| 2200 | NA | NA | 0 |
| 2300 | NA | NA | 0 |

[e]usual sign convention applies (angles measured towards north and west are positive)

### 6.4.2 LCOE optimization for different locations

The location-specific optimized LFR designs produced minimised LCOE values ranging from 0.064 to 0.072 €/kWh. The difference in results was largely a result of the different irradiance profiles rather than significant variations in LFR designs. The annual average DNI ($W/m^2$) for the hours of operation of the plants was calculated as 590, 660 and 760 for Spain, China and Australia, respectively. A recently completed (in 2019) LFR system located in Dunhuang, China reported a LCOE of 0.087(€/kWh) (NREL 2021). The optimized LCOE for the same location in this research suggested that a 23% improvement in LCOE could be achieved. The location of the installation did not show a significant effect on the optimized design variables.

Table 6.14: A comparison of optimized results for different locations around the world

| | $h_r$(m) | $n_m$ | $w_m$(m) | $s_m$(m) | A($m^2$) | Min. LCOE (€/kWh) |
|---|---|---|---|---|---|---|
| PSA, Spain | 8.86 | 22 | 0.628 | 0.101 | 13.82 | 0.072 |
| Dunhuang, China | 9.05 | 18 | 0.815 | 0.098 | 14.67 | 0.067 |
| Perth, Australia | 9.2 | 18 | 0.772 | 0.131 | 13.9 | 0.064 |

To examine the impact on the LCOE of having a single design installed in each location (rather than a unique design for each location), Table 6.15 shows each optimized LFR system installed in the other locations. Although different optimized designs provided slightly different LCOE if installed in the same location, the difference between the results was negligible.

Table 6.15: Effects on LCOE (€/kWh) due to installing optimized designs in other locations

| | | When installed in: | | |
|---|---|---|---|---|
| | | PSA, Spain | Dunhuang, China | Perth, Australia |
| Designed and optimized for: | PSA, Spain | 0.0722 | 0.0671 | 0.0638 |
| | Dunhuang, China | 0.0723 | 0.0670 | 0.0637 |
| | Perth, Australia | 0.0725 | 0.0671 | 0.0637 |

### 6.4.3 Year-round modelling of optimized systems

A detailed cost evaluation using 365 days of TMY data combined with power generation through the Rankine cycle was conducted on the optimized systems and the results are shown in Table 6.16.

Table 6.16: Minimum LCOE (€/kWh) obtained using different modelling approaches

| | PSA, Spain | Dunhuang, China | Perth, Australia |
|---|---|---|---|
| Optimized | 0.072 | 0.067 | 0.064 |
| Calculated for yearly TMY data coupled with Rankine cycle | 0.077 | 0.073 | 0.068 |

Calculated LCOE values based on year-round modelling are higher than the optimized values. LCOE increase for Spain, China and Australia were 7%, 8% and 6%, respectively, in comparison to four days of modelling and a fixed power block efficiency assumption. The LCOE increase can be explained by an overestimation of the solar irradiance due to the four days of modelling and low power block efficiency. The power block efficiency had dropped from a 33% fixed value to 31.6 % for the Rankine cycle calculation. However, as the power block efficiency of a CSP plant typically varies between 30-40% (Wang et al. 2019; Yan et al. 2021), changes from the optimized LCOE values can still be minimal under a more advanced and efficient power block.

### 6.4.4 Sensitivity analysis of design variables and cost parameters

A sensitivity analysis was carried out to identify the effects of design variables on the LCOE when the variables were at non-optimal values. The analysis was performed by changing one variable at a time while keeping all other variables at the optimum values based on the design for Spain (see Table 6.14). As seen in Figure 6.8, the LCOE was most sensitive to changes in receiver height, while mirror spacing had the least effect. Mirror width and the number of mirrors were equally important to get the desired LCOE. Figure 6.9 shows a percentage cost breakdown for the optimized design. It is interesting to note the significant effect that the receiver height has on the design, even though the cost involved is only 5% of the total. This is because of mirror defocussing when the height is considerably changed. Consequently, the optical efficiency significantly drops, reducing

the energy output. The same effect exists in the performance-based optimization; however, it was not so pronounced due to low optimized height values.

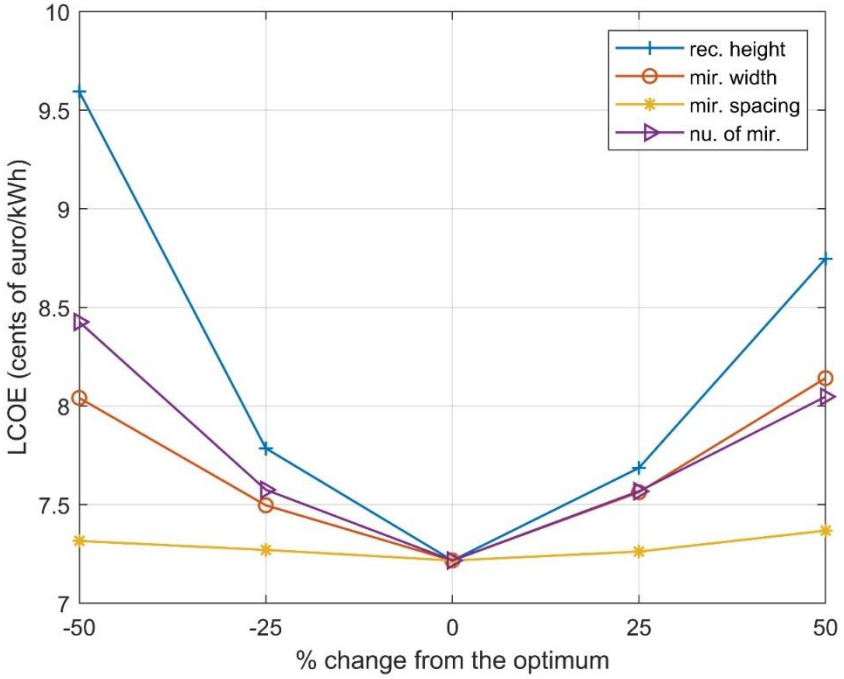


Figure 6.8: Sensitivity of design variables for LCOE

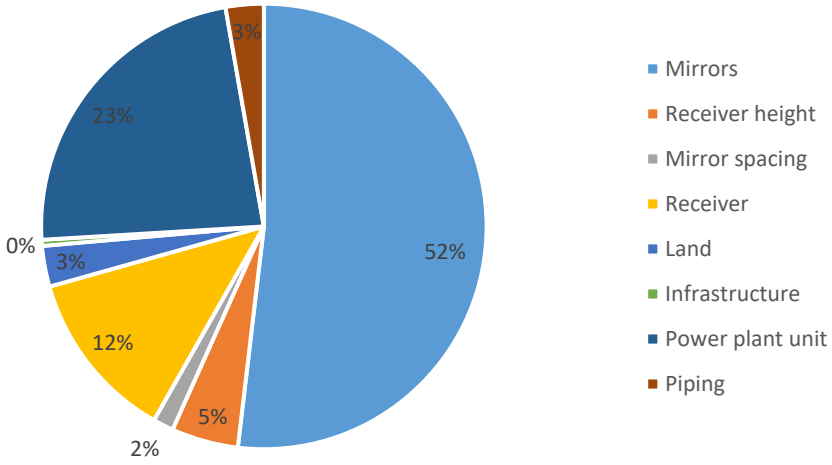


Figure 6.9: Cost breakdown of the optimized design for PSA, Spain

According to the cost breakdown, the mirror costs were the highest contributor to the total cost. Furthermore, due to large volume manufacturing, the possibilities for cost

savings are more likely in comparison to other component costs. In order to observe the effects of optimized design variables for potential mirror cost changes, four optimization simulations were carried out reducing the mirror cost by 20% to 80% (see Figure 6.10, tabulated data is shown in Table Appendix C.1). Weather data for PSA, Spain were used for the optimizations.

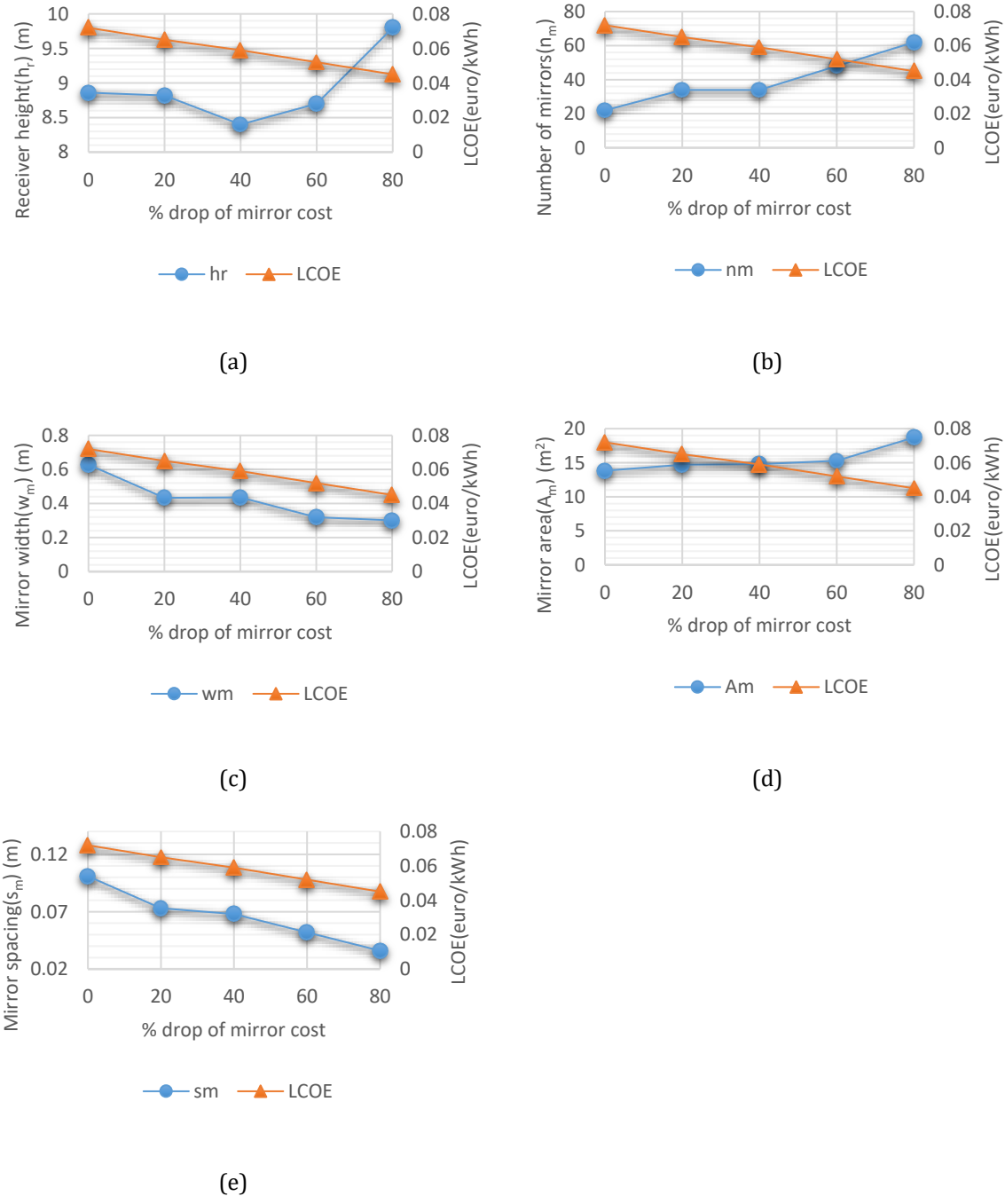


Figure 6.10: Optimized LCOE and design variables at different percentage reductions in mirror cost: (a) receiver height, (b) number of mirrors, (c) mirror width, (d) mirror area, (e) mirror spacing

It is seen that a considerable LCOE reduction can be obtained for an optimized LFR system with reduced mirror costs. For instance, a 40% mirror cost reduction would result in an 18% lower LCOE. The behaviour of optimized design variables for the reduced costs was dependent on the design variable considered. The mirror area, which combined the number of mirrors and mirror width, was almost constant until an 80% drop in the mirror cost. When the mirror costs were reduced, the number of mirrors was increased and the mirror width became lower, resulting in a reduced mirror spacing. As identified in several previous simulations, the change of receiver height was highly sensitive and complex. When the effect of the mirror costs is reduced, the effect of energy performance becomes more significant (see section 6.3.3 for performance based results) and the system is transforming towards narrow mirrors. Therefore, as LFR component costs change (i.e. such as the mirror cost reduction scenario examined in this section), these results highlight the importance of conducting new optimization studies to revise system designs.

## 6.5 A discussion on performance and cost based optimization

This section discusses the performance and cost based optimization of LFRs. Optimized results are compared against other available studies for commercial and existing LFR plants. Furthermore, the results of the two objective functions are compared and the effects of the main model assumptions are discussed.

### 6.5.1 Performance-based optimization: comparison of results against other studies

As the coupled optical and thermal modelling approach used in this study is different to other optimization studies, a direct comparison between the results is not possible. Table 6.17 summarise the results of the most relevant literature and makes a comparison with this study's results for an LFR using slightly curved mirrors.

Table 6.17: Comparison of performance-based optimization results with other studies

| Author | Receiver Type | Rec. aperture (m) | $h_r$ (m) | $n_m$ | $w_m$ (m) | $s_m$ (m) | $T_r$ (°C) | Basis of the Optimization |
|---|---|---|---|---|---|---|---|---|
| (Roostaee and Ameri 2019) | Trapezoidal cover, multi-tube | 0.38-0.42 | 8* | 24-26 | 0.55-0.6 | 0.25* | 127-227* | Optical |
| (Pulido-Iparraguirre et al. 2019) | Multi-tube, no secondary concentrator | 0.12* | 2.3 | 12 | 0.28 | - | - | Optical |
| (Moghimi, Craig, and Meyer 2017) | Trapezoidal cover, multi-tube | 0.33 | 18.6 | 38 | 0.68 | 0.02 | - | Optical and cost |
| (Boito and Grena 2016) | Flat surface | 0.4* | 10* | 25* | 1 | 0.21 | - | Optical and cost |
| This study | Single tube , CPC | 0.42* | 3.9 | 60 | 0.076 | 0.058 | 371 | Optical thermal coupled |

*Fixed values (not optimized)

In comparison to other studies, this study modelled a more complex receiver with several design variables. Other studies have modelled a flat surface, bare tubes or a trapezoidal cavity with multi-tubes as receivers. This study considered a parabolic concentrator and a glass tube encapsulating the absorber, making the modelling and optimization more challenging. Furthermore, only Roostaee and Ameri (2019) have considered the effect of the receiver temperature, which was used to verify the optimized results and not as a design variable. Most studies have optimized the system around fixed design variables such as receiver height to avoid complexity and save simulation time. However, fixing such critical design variables significantly limits the search space and misses the global optimum, if it lies elsewhere. Due to the differences in receiver types, fixed design variables and various modelling approaches, design variables reported in the literature are highly diverse. It is seen that the mirror widths of trapezoidal receiver designs are

optimized around the receiver aperture while the mirror width of this study is optimized around the absorber tube diameter (0.07 m) resulting in narrow mirrors. However, this study addresses most of the aforementioned limitations in other studies and provides results that are close to those reported in the literature.

Although optimized industrial designs have not been widely reported, the latest developments show several similarities to the optimized designs shown in this work. For example, Industrial Solar GmbH (2021) have designed an LFR system using an evacuated tube receiver with a temperature limit of 400°C at a 4 m height and with a 5.5 $m^2$ mirror area per meter length. For the same receiver type with a constant temperature operating condition and slightly curved mirrors, this research proposed a receiver height of 3.9 m and a mirror area of 4.6 $m^2$. However, the Industrial Solar system has only 11 mirrors with a width of 0.5 m, which could be due to the cost of additional mirrors and tracking mechanisms.

### 6.5.2 Performance-based optimization: multiple simulations and computational time

Each optimized design was run three times to investigate possible variations in converged solutions due to the nature of GA combined with SolTrace's MCRT methodology. Different mirror widths and mirror number combinations resulted in designs with similar mirror areas and total efficiencies, suggesting that there could be multiple near-optimal solutions. A similar behaviour has been previously identified by Boito and Grena (2016) for a much simpler LFR design. In addition to this, the error between the best and the worst values of their solutions was 0.7%, while this study reports less variation in the optimized results as seen in Table 6.18. Detailed results of all optimization runs carried out are given in Table Appendix C.2.

It was noted that obtaining a consistent solution is easier for fully curved and flat mirror configurations, due to having less variation in solar flux on the receiver against design changes. In slightly curved mirrors, as all mirrors have a single focal length, the focal points of almost all the mirrors lie either below or above the receiver. When the receiver height changes, the receiver moves away from some mirror focal points while getting closer to others. This phenomenon results in a complex receiver solar flux pattern.

Therefore, the variation of the optimized results of slightly curved mirrors is higher compared to other primary mirror types.

Table 6.18: Variation of multiple simulation runs

| | Receiver temperature condition | Mean of total theoretical efficiency (%) | Standard deviation |
|---|---|---|---|
| Fully Curved | $T_r \leq 250$ °C | 28.24 | 0.03 |
| | $T_r \leq 400$ °C | 30.42 | 0.21 |
| | Constant | 30.12 | 0.07 |
| Slightly curved | $T_r \leq 250$ °C | 27.85 | 0.03 |
| | $T_r \leq 400$ °C | 29.06 | 0.79 |
| | Constant | 29.43 | 0.45 |
| Flat | $T_r \leq 250$ °C | 24.94 | 0.03 |
| | $T_r \leq 400$ °C | 27.63 | 0.46 |
| | Constant | 28.75 | 0.11 |

The computational time for each simulation was around seven hours using a computer with Core™ i5 @ 3.3 GHz (4 CPUs) processor and 8GB RAM. This computational time is explained by 4000-4500 candidate solution checks, where each optical simulation takes a few seconds to run and several different sun positions. The computational time taken by the thermal simulation was not significant in comparison to optical simulation.

### 6.5.3 Cost-based optimization: comparison of results with existing plants and studies

The optimized design, obtained using the parameters mentioned in the section 6.4.1 and for Spain, is shown against existing plants and studies in Table 6.19. It is important to note that, to the best of the author's knowledge, designs and other studies reported in this table have not been optimized for LCOE.

Table 6.19: Comparison of LCOE optimization results with other studies and LFR power plants (Chaitanya Prasad, Reddy, and Sundararajan 2017; Bellos 2019; SUNCNIM 2019; CSP Focus 2021; NREL 2021)

| Name | Type/ Capacity(MW) | Year Completed | Rec. Type | $h_r$ (m) | $n_m$ | $w_m$ (m) | $s_m$ (m) | LCOE (€/kWh) |
|---|---|---|---|---|---|---|---|---|
| Alba Nova 1/ France | Demonstration/ 12 | - | Single tube , CPC | - | 12 | ~0.7 | - | - |
| Llo/France | Commercial/ 9 | 2019 | Single tube, CPC | ~8.5 | 14 | ~1 | ~0.3 | - |
| Puerto Errado 2/Spain | Commercial/ 30 | 2012 | Single tube , CPC | - | 16 | ~0.7 | - | 0.26 |
| Dhursar (CLFR)/ India | Commercial/ 125 | 2014 | - | - | - | - | - | 0.095 |
| Huaqiang TeraSolar/ China | -/ 15 | 2018 | - | - | - | - | - | 0.1 |
| Dacheng Dunhuang/ China | Commercial/ 50 | 2019 | - | - | 20 | ~0.7 | - | 0.087 |
| FRESDEMO | Pilot/- | 2009 | Single tube , CPC | 8 | 25 | 0.6 | 0.25 | - |
| Vallipuram | Demonstration/ - | - | Single tube , CPC | 7.9 | 12 | 1.07 | 0.43 | - |
| Study(not optimized) (Morin et al. 2006) | -/ 50 | - | Single tube , CPC | 7.5 | 34 | 0.5 | 0.25 | 0.125 |
| Study (not optimized) (Rungasamy, Craig, | -/ 50 | - | Single tube , CPC | 9 | 48 | 0.5 | 0.01 | 0.167 |

| | | | | | | | | |
|---|---|---|---|---|---|---|---|---|
| and Meyer 2019) | | | | | | | | |
| This study/ PSA, Spain | -/50 | - | Single tube , CPC | 8.86 | 22 | 0.628 | 0.10 | 0.072 |

The optimized LCOE is considerably lower compared to values reported in other studies and commercial power plants. The studies of Morin et al. (2006) and Rungasamy, Craig, and Meyer (2019) presented LCOE for two LFR designs. Rungasamy, Craig, and Meyer (2019) considered a larger receiver, which increased both the receiver cost and energy capture. Morin et al.'s (2006) work was based on a receiver with a 0.075 m diameter, which is very close to the PTR®70, and they reported an LCOE of 0.125 €/kWh. However, they did not provide any detailed information on cost coefficients or energy calculations. The latest LCOE figures of commercial level plants are considerably lower compared to early designs such as Puerto Errado, confirming the rapid drop in CSP energy costs over the years. The latest LCOE figure available for a commercial plant is reported as 0.087(€/kWh) for the Dunhuang LFR system, China. Furthermore, the existing system has 20 mirrors of approximately 0.7 m width. An optimized design for the same location provided 18 slightly wider mirrors of 0.815 m (shown in Table 6.14) indicating that minor design changes from existing industrial designs can significantly improve the LCOE.

Optimized design variables were in close range with the values reported for existing commercial and demonstration LFR plants. The mirror width was around 0.7 m in most of the plants and the optimized design suggested a slightly narrow mirror of 0.63 m. The number of mirrors was found to vary from 12-20, and the optimized design suggested 22 mirrors. Llo LFR in France provided a more complete set of design variables and closely resembled the optimized design. The mirror area of Llo is 14 $m^2$, which is very close to the optimized mirror area of 13.8 $m^2$, made out of 22 mirrors with a 0.63 m width. Moreover, the optimized design indicated a considerable mirror spacing saving while showing a similar receiver height against Llo. A detailed comparison was not possible due to the unavailability of design data of existing LFR systems. However, it is seen that the optimized design resulted in lower mirror costs due to reduced mirror area. Compared

to the existing industrial LFR systems, the optimized design showed possibilities of LCOE savings from optimum mirror number-width combinations, slight changes in receiver heights and reduced mirror spacing.

### 6.5.4 Cost-based optimization: convergence and computational time

For the cost-based optimization, only slightly curved mirrors were used with a fixed receiver temperature producing one optimization scenario. Seven optimization runs conducted for PSA, Spain resulted in a mean LCOE (€/kWh) of 0.07192 with a standard deviation of 0.00023 showing an acceptable uncertainty level (See Table Appendix C.3 for more detail). It is important to note that a lower uncertainty level can be achieved at the expense of computational time.

Around 15 hours of simulation time was observed using a computer with Core™ i5 @ 3.3 GHz (4 CPUs) processor and 8GB RAM for each optimization run. In comparison to performance based-optimization, using solar irradiance data for four different days in the cost-based simulation drastically increases the computational times. If the receiver temperature was included as an optimization variable, it would further increase the computational time. Figure 6.11 shows how the LCOE changes with the progression of the optimization. It shows the possibility of making further savings in computational times by using improved stopping criteria to terminate the optimization at an early generation.

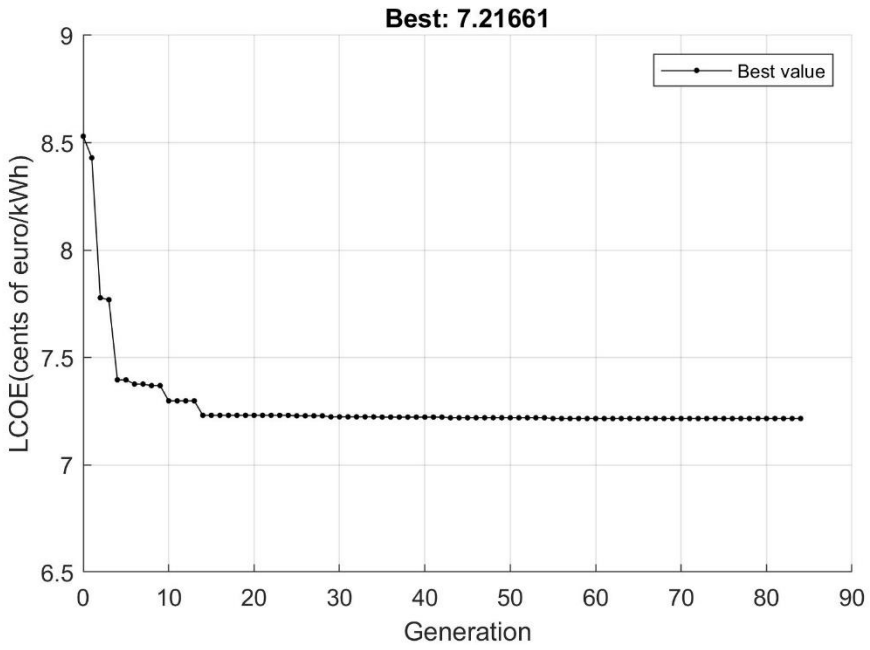


Figure 6.11: Convergence of LCOE in the optimization

### 6.5.5 A comparison of performance and cost based optimizations

Despite the optimization results being very close to those of existing commercial LFR designs, the findings show that significant improvements can still be made. Whilst it is difficult to say how much the LCOE can be improved through optimization as cost values are not widely reported for commercial systems, the findings in this research suggest that LCOE savings of around 25% can be achieved with only minor modifications to the designs. The performance-based optimization work resulted in compact designs with low mirror heights, widths and spacing. Optimized widths of slightly curved and flat mirrors were close to the absorber tube diameter. Conversely, cost-based optimization resulted in higher receiver heights, mirror widths and spacing. Although there are some commercial designs that are similar to the performance-based optimized design, most existing ones are very close to a cost-based optimized design.

As observed in the performance based optimization, different mirror widths and mirror number combinations resulted in designs with similar mirror areas and total efficiencies. This suggests that there could be multiple near-optimal solutions. This behaviour is observed more easily in slightly curved mirrors, due to their complex interaction of mirror focal points with the receiver. However, receiving multiple solutions was not

significant in cost-based optimization due to two reasons: LCOE is largely dominated by costs; selecting the solution with the least mirror number saves the costs of additional tracking mechanisms.

### 6.5.6 Important model assumptions

The presented results depend on the assumptions made to reduce computational time and model complexity. Although actual weather data based on the TMY dataset was used and up to 11 hours of sunshine hours were included in the simulation, only five sun positions were used to represent each day and four days to represent a year in the cost-based optimization. Furthermore, due to the large number of scenarios present in the performance-based optimization, a generic solar radiation profile on the transverse plane was considered. To justify these assumptions further, annual TMY data (24 hours and 365 days) was used to evaluate the performance of optimized systems and the results showed a 6%-8% increase in LCOE. However, the assumptions have a minimal effect on the results based on comparisons, such as in different mirror types, locations and variable sensitivity.

Several assumptions have been made in this research to develop the optical model. The aim point of reflected solar rays from the LFR mirrors was taken as the centre of the absorber tube. Considering different aim point/points of mirrors for improved efficiency or uniform solar flux is an interesting topic but not addressed in this work. Optical errors (e.g. tracking error and slope error) have been considered and appropriate values have been assigned based on the literature. However, the eccentric error due to the difference between the actual mirror pivoting points and geometrical centres has not been included in this study. Furthermore, the north-south mirror-tracking axis has been selected for this study, as it is the most common LFR configuration and is reported to provide slightly higher annual energy collection compared to east-west tracking.

Based on the modelling approach used in this study, fluid flow parameters inside the receiver tubes have not been considered. Although this modelling approach has been widely used to decouple the fluid flow and thermal models, a relevant heat exchanger analysis has to be conducted if bulk fluid temperature and flow parameters are used for further analysis (e.g. power cycle modelling). However, these parameters were not

required for this study as the performance analysis has been based on maximum power generation potential, but could be an interesting area for further research.

Recent reports on the cost of LFR systems suggest considerably lower LCOE values in comparison to early designs such as Puerto Errado 2. This implies that manufacturing and other related costs have dropped over the years. Although the LFR cost model used in this study has been the most detailed and reliable source reported so far, the model can be improved further. For instance, fixed operation and maintenance costs over the lifetime of the project have been assumed in the current model and a more detailed LCOE model can be implemented in further work. Furthermore, despite the detailed cost breakdown of receiver elements, the receiver costs were assumed to be proportional to an exponent of the receiver diameter. Such model assumptions can be further improved once the cost data of the recent LFR developments become more widely available.

# 7

# Conclusions and recommendations

## 7.1 Conclusions

This section summarises the work that has been carried out to answer the research questions and how well the research questions have been answered. The novelty and contribution to the knowledge are highlighted in response to each research question. The overarching conclusions finally summarise whether the aim of this research has been achieved.

### 7.1.1 Research question 1

- Can thermal and ray tracing models be coupled together and optimized for designing LFR systems?

The work detailed in Chapters 4 and 5 answers the above research question. Studies on LFR system design through optimization methods are rare. There have been some efforts to optimize LFR designs through optical modelling alone. However, there is a research gap for a comprehensive LFR design process to be carried out considering both optical and thermal aspects simultaneously through an optimization algorithm. As shown in this study, it is possible to couple optical models, through ray tracing, and thermal models together to be solved with an optimization algorithm for designing LFR systems. However, appropriate assumptions and modelling methods have to be used to maintain the computational time manageable.

Instead of taking an analytical approach or developing MCRT based in-house ray tracing codes, optical modelling was implemented on the SolTrace ray tracing tool. Being a specially designed tool for CSP optical design, SolTrace enabled optical modelling with high accuracy and detail such as non-parallel solar rays, multiple reflections and

directional dependant surface optical properties. Furthermore, it enabled the modelling of an optically challenging and frequently overlooked, but highly relevant, receiver consisting of a CPC and a glass tube to be undertaken. Suggested optical modelling provided excellent accuracy, with only a 1.2% difference in optical efficiency compared against the literature. Optical modelling and performance improvements of an LFR prototype using SolTrace have been published at an early stage of this work (Sirimanna and Nixon 2020).

Thermal models were based on analytical equations and empirical correlations. Analytical thermal modelling under steady state conditions is typically highly computationally effective against the other alternatives such as CFD. Nevertheless, while having a very low computational weight, the thermal model has to provide an accurate result for any design variable in the search space to be employed in an optimization algorithm effectively. To achieve this, suitable modelling methods and assumptions were made while considering all the important parameters to develop a comprehensive thermal model. A comparison of the thermal modelling results against the experimental results and other studies confirmed the suitability of the thermal models developed for this work.

The optical and thermal models were effectively coupled together to be solved by an optimization method with reasonable computational power (several hours of simulation on an ordinary computer). Optimizations were carried out for performance and cost based objective functions: total theoretical efficiency and LCOE, and to examine five design variables: mirror number, width and spacing; receiver height and operating temperature. The computational weight of the thermal simulation in comparison to the optical simulation, which was a few seconds for a set of design variables and one sun position, was found to be negligible. The total time taken for the optimization is highly dependent on several factors including the optimization method, objective functions and the accuracy expected. Out of the derivative-based, derivate free and population-based optimization methods tested, pattern search, simulated annealing and GA provided very good solutions (Some of these findings have been published as Sirimanna, Nixon, and Innocente (2022)). Although GA was selected for further work, other derivative-free and population-based methods, which were not tested, may respond well to a similar

problem. In the same way, an alternative ray tracing tool may be used in place of SolTrace. Such investigations are worthy of further study.

This research provided a framework that enables a more improved and cost-efficient LFR system to be designed for power generation. The process outlined in this research can be modified to investigate alternative objective functions, novel receiver designs and other LFR configurations. Optimized designs provided improved results, in terms of design variables and fitness values (e.g. LCOE), to what has been reported in the literature. For instance, a recently completed LFR system located in Dunhuang, China reports a LCOE of 0.087(€/kWh) (NREL 2021). Optimized LCOE for the same location shows a significant LCOE improvement of 23%; however, further work remains to validate this finding using the same cost values and LCOE methodology used by the company to report their LCOE, which currently remain unknown.

### 7.1.2 Research question 2

- How do different parameters (mirror types/operating temperatures/locations) and requirements (maximising performance/minimising energy costs) influence optimal LFR designs?

The work outlined in Chapter 6 answers the above research question. Answering this research question provides new knowledge on the understanding of how an optimum LFR design changes based on different design configurations, operating conditions, locations and design requirements.

Out of the primary mirror types in practice, both slightly curved and fully curved mirrors can achieve nearly the same performance, measured in terms of total theoretical efficiency. Furthermore, they also provide a slightly higher (2.5-4.5%) efficiency and savings in terms of design variables compared to flat mirrors. For instance, fully curved mirrors reduced the land area, mirror area and receiver height by 35%, 29% and 34%, respectively. The results highlight that an optimized fully curved mirror system results in an efficient and compact design, whereas an optimized flat mirror LFR results in a larger less efficient system. The compact design consists of a reduced number of wider mirrors, while the larger system consists of more narrow mirrors. Slightly curved mirrors

acted as a compromise between the two mirror types. These results bring up new interesting research questions. For instance, how will these designs change if optimized under constrained land requirements in different applications?

The receiver temperature, as a design variable, provided interesting insights. The optimized results clearly showed that an optimum operating temperature exists, and it's not the highest possible temperature as anticipated. For instance, fully curved mirrors showed an optimum temperature of 363°C, while 400°C was the maximum possible value based on material limits. Although a higher efficiency employing different hourly temperatures (variable temperature operating condition) was expected to be observed, a similar performance can be achieved by a constant optimum temperature, which has to be found through a relevant design optimization.

Performance-based optimization shows traces of multimodality. Different mirror widths and mirror number combinations resulted in designs with similar mirror areas and total efficiencies, suggesting that there could be multiple near-optimal solutions. This behaviour is more apparent in slightly curved mirrors, where the focal points of almost all of the mirrors lie either below or above the receiver creating complex solar flux patterns. However, the variation of the optimized solutions was much lower for fully curved and flat mirror configurations, due to there being less variation in solar flux on the receiver with design changes.

The optimizing framework suggested that significant improvements can be achieved by cost-based optimization. Optimized results show much lower LCOE and, design variables at a close range with the values reported in commercial and demonstration LFR plants. For instance, LCOE savings of up to 23% were observed in comparison to commercial level plants. It was seen that minor design changes in terms of receiver height, mirror number and widths from existing industrial designs can significantly improve the LCOE. Mirror spacing showed considerable reductions compared to existing designs, which can save energy costs under an expensive or size limited land setting.

Investigating different locations resulted in interesting conclusions in terms of LCOE and design variables. Optimized LCOE shows a clear distinction based on the locations considered. For instance, LCOE obtained for Australia was 11% lower than that of Spain. Although a higher annual average DNI results in a lower LCOE as expected, the exact

amount of LCOE drop highly depends on the solar radiation profile of the location. Moreover, it was interesting to note that the location of the installation does not show a significant effect on the optimized design variables. This would result in one optimum design to be used in different locations around the world without affecting LCOE significantly.

### 7.1.3 Research question 3

- How sensitive are the optimal LFR designs to potential changes in costs and design variables?

Receiver temperature and receiver height are the most important design variables to get right in an LFR design. Performance based-optimization showed that regardless of the mirror configuration, an LFR's performance has a high sensitivity to deviations from the ideal operating temperature. However, LCOE is most sensitive to changes in receiver height. Interestingly, mirror spacing has the least effect on performance and LCOE.

Cost reductions due to mass-scale manufacturing of LFR components would reduce the cost of electricity significantly. For instance, a 20% drop in mirror cost would result in a 9.7% drop in LCOE. The results implied that the current industrial developments are largely dominated by costs rather than performance. When the costs of the components such as mirrors become cheaper, the effect of efficiency improvements becomes more significant in future designs.

This research provided a framework that enabled more improved and cost-efficient LFR systems to be designed. A novel coupled optical and thermal modelling approach combined with GA optimization was found to be highly effective for this purpose. The results led to an understanding of how different design parameters, setups, applications, component costs and their changes will influence the performance and cost-efficiency of LFR systems. Therefore, the aim highlighted at the beginning of the research has been achieved.

## 7.2 Recommendations for future work

The design framework provided in this work easily facilitates several further improvements such as incorporating other receiver designs and variables. For instance, validated thermal and optical models have already been presented for the trapezoidal cavity receiver. Furthermore, additional receiver design variables such as receiver width, number of tubes and receiver diameter can be considered for an optimal mirror-receiver design. Although a predesigned CPC was used in this work, solar flux distribution around the absorber can vary depending on mirror field parameters resulting in uneven flux distribution, including local hotspots. However, addressing receiver solar flux distribution can be a multi-objective optimization problem when considered with power generation efficiency or LCOE.

It is recommended that a detailed power block, storage and receiver flow modelling be included in future work. LFR power generation is typically based on the Rankine cycle, which requires flow parameters such as pressure and mass flow rate for modelling. Furthermore, the modelling process involves considering various steam properties such as enthalpy and entropy for numerous flow conditions and temperatures. Although the performance of optimized LFR systems was evaluated in this work for the ideal Rankine cycle, more detailed modelling and computational resources are necessary to integrate power block performance into the optimization process. This modelling can be started by addressing detailed flow conditions in the receiver tube, especially in the case of direct steam generation. Thermal storage is one of the unique features of CSP that increases its dispatchability over the other renewables. Some of the latest LFR plants use molten salts as a working fluid and storage medium, and report lower energy costs. Thermal storage modelling can be liked to power block and receiver flow modelling, providing one comprehensive model for optimum LFR designs. Although addressing the above work would provide more accurate performance and energy costs, the complexity arises from a large number of variables and the two-phase flow has to be carefully addressed to avoid excessive computational power requirements.

As the optimization framework presented in this work enabled the integration of alternative methods instead of GA, a better alternative can be used to address the complexity that arises from extended modelling or adding more design variables. This

study identified pattern search and simulated annealing as alternatives for GA. However, there is a large number of optimization methods to select from. The presence of both discrete and continuous variables in the mathematical models is one of the main limitations in selecting a suitable optimization method. Modifying existing optimization algorithms or conducting the optimization for a set of fixed discrete variables are some simple ways to solve this limitation.

With more recent technological developments and new LFR plants installed worldwide, a new cost model for the LFR systems can be developed. The cost model in this work has been developed based on the data obtained more than a decade ago. Although future cost fluctuations have been studied to some extent, the main cost assumptions have not been changed in this study. For instance, the cost of the tracking mechanism has been embedded in the mirror costs in this cost model and the cost of the mirror spacing largely depends on the structural design. More relevant cost breakdowns will lead to better decisions on number of mirrors and mirror spacing. Therefore, developing a detailed new cost model addressing new structural designs, tracking mechanisms, manufacturing and installation methods will result in more cost-efficient designs.

The design approach suggested in this research can be extended to other LFR systems, such as the Compact Linear Fresnel Reflectors (CLFR) (e.g. modelling a CLFR would only require minor modifications to incorporate a second receiver tower). A similar approach can be applied to other CSP systems; however, depending on the complexity of the design, computational times could be high. There is, therefore, a need to reduce optical and optimization simulation times whilst still achieving satisfactory accuracy and convergence of solutions when optimizing CSP systems.

# References


Abbas, R., Valdés, M., Montes, M. J., and Martínez-Val, J. M. (2017) 'Design of an Innovative Linear Fresnel Collector by Means of Optical Performance Optimization: A Comparison with Parabolic Trough Collectors for Different Latitudes'. *Solar Energy* 153, 459-470

Abbas, R. and Martínez-Val, J. M. (2015) 'Analytic Optical Design of Linear Fresnel Collectors with Variable Widths and Shifts of Mirrors'. *Renewable Energy* 75, 81-92

Abbas, R., Montes, M. J., Rovira, A., and Martínez-Val, J. M. (2016) 'Parabolic Trough Collector Or Linear Fresnel Collector? A Comparison of Optical Features Including Thermal Quality Based on Commercial Solutions'. *Solar Energy* 124, 198-215

Abbas, R., Muñoz, J., and Martínez-Val, J. M. (2012) 'Steady-State Thermal Analysis of an Innovative Receiver for Linear Fresnel Reflectors'. *Applied Energy* 92, 503-515

Ahmadi, M. H., Sayyaadi, H., Mohammadi, A. H., and Barranco-Jimenez, M. A. (2013) 'Thermo-Economic Multi-Objective Optimization of Solar Dish-Stirling Engine by Implementing Evolutionary Algorithm'. *Energy Conversion and Management* 73, 370-380

Ajdad, H., Filali Baba, Y., Al Mers, A., Merroun, O., Bouatem, A., and Boutammachte, N. (2019) 'Particle Swarm Optimization Algorithm for Optical-Geometric Optimization of Linear Fresnel Solar Concentrators'. *Renewable Energy* 130, 992-1001

Alhaj, M., Mabrouk, A., and Al-Ghamdi, S. G. (2018) 'Energy Efficient Multi-Effect Distillation Powered by a Solar Linear Fresnel Collector'. *Energy Conversion and Management* 171, 576-586

Aqachmar, Z., Ben Sassi, H., Lahrech, K., and Barhdadi, A. (2021) 'Solar Technologies for Electricity Production: An Updated Review'. *International Journal of Hydrogen Energy* 46 (60), 30790-30817

Arabkoohsar, A. (2020) 'Combined Steam Based High-Temperature Heat and Power Storage with an Organic Rankine Cycle, an Efficient Mechanical Electricity Storage Technology'. *Journal of Cleaner Production* 247, 119098

Askari, I. B. and Ameri, M. (2018) 'Solar Rankine Cycle (SRC) Powered by Linear Fresnel Solar Field and Integrated with Multi Effect Desalination (MED) System'. *Renewable Energy* 117, 52-70

Askari, I. B., Ameri, M., and Calise, F. (2018) 'Energy, Exergy and Exergo-Economic Analysis of Different Water Desalination Technologies Powered by Linear Fresnel Solar Field'. *Desalination* 425, 37-67

Askari, I. B. and Ameri, M. (2017) 'The Application of Linear Fresnel and Parabolic Trough Solar Fields as Thermal Source to Produce Electricity and Fresh Water'. *Desalination* 415, 90-103

Askari, I. B. and Ameri, M. (2016) 'Techno Economic Feasibility Analysis of Linear Fresnel Solar Field as Thermal Source of the MED/TVC Desalination System'. *Desalination* 394, 1-17

Aslambakhsh, A. H., Moosavian, M. A., Amidpour, M., Hosseini, M., and AmirAfshar, S. (2018) 'Global Cost Optimization of a Mini-Scale Liquefied Natural Gas Plant'. *Energy* 148, 1191-1200

Astolfi, M., Martelli, E., and Pierobon, L. (2017) '7 - Thermodynamic and Technoeconomic Optimization of Organic Rankine Cycle Systems'. in *Organic Rankine Cycle (ORC) Power Systems*. ed. by Macchi, E. and Astolfi, M. : Woodhead Publishing, 173-249

Azad, A., Aghaei, E., Jalali, A., and Ahmadi, P. (2021) 'Multi-Objective Optimization of a Solar Chimney for Power Generation and Water Desalination using Neural Network'. *Energy Conversion and Management* 238, 114152

Balaji, S., Reddy, K. S., and Sundararajan, T. (2016) 'Optical Modelling and Performance Analysis of a Solar LFR Receiver System with Parabolic and Involute Secondary Reflectors'. *Applied Energy* 179, 1138-1151

Barbón, A., Barbón, N., Bayón, L., and Sánchez-Rodríguez, J. A. (2018a) 'Optimization of the Distribution of Small Scale Linear Fresnel Reflectors on Roofs of Urban Buildings'. *Applied Mathematical Modelling* 59, 233-250

Barbón, A., Barbón, N., Bayón, L., and Otero, J. A. (2016) 'Optimization of the Length and Position of the Absorber Tube in Small-Scale Linear Fresnel Concentrators'. *Renewable Energy* 99, 986-995

Barbón, A., Sánchez-Rodríguez, J. A., Bayón, L., and Bayón-Cueli, C. (2019) 'Cost Estimation Relationships of a Small Scale Linear Fresnel Reflector'. *Renewable Energy* 134, 1273-1284

Barbón, A., Sánchez-Rodríguez, J. A., Bayón, L., and Barbón, N. (2018b) 'Development of a Fiber Daylighting System Based on a Small Scale Linear Fresnel Reflector: Theoretical Elements'. *Applied Energy* 212, 733-745

Bastidas-Rodriguez, J. D., Petrone, G., Ramos-Paja, C. A., and Spagnuolo, G. (2017) 'A Genetic Algorithm for Identifying the Single Diode Model Parameters of a Photovoltaic Panel'. *Mathematics and Computers in Simulation* 131, 38-54

Baum, V. A., Aparasi, R. R., and Garf, B. A. (1957) 'High-Power Solar Installations'. *Solar Energy* 1 (1), 6-12

Bayón-Cueli, C., Barbón, A., Bayón, L., and Barbón, N. (2020) 'A Cost-Energy Based Methodology for Small-Scale Linear Fresnel Reflectors on Flat Roofs of Urban Buildings'. *Renewable Energy* 146, 944-959

Bellos, E. (2019) 'Progress in the Design and the Applications of Linear Fresnel Reflectors – A Critical Review'. *Thermal Science and Engineering Progress* 10, 112-137

Bellos, E. and Tzivanidis, C. (2018a) 'Multi-Criteria Evaluation of a Nanofluid-Based Linear Fresnel Solar Collector'. *Solar Energy* 163, 200-214

Bellos, E. and Tzivanidis, C. (2018b) 'Development of Analytical Expressions for the Incident Angle Modifiers of a Linear Fresnel Reflector'. *Solar Energy* 173, 769-779

Bermejo, P., Pino, F. J., and Rosa, F. (2010) 'Solar Absorption Cooling Plant in Seville'. *Solar Energy* 84 (8), 1503-1512

Bernhard, R., Laabs, H., de LaLaing, J., Eck, M., Eickhoff, M., Pottler, K., Morin, G., Heimsath, A., Georg, A., and Häberle, A. (2008) 'Linear Fresnel Collector Demonstration on the PSA, Part I – Design, Construction and Quality Control'. in *14th International SolarPACES Symposium.* held March 3-7, 2008. Las Vegas (USA)

Besarati, S. M. and Goswami, D. Y. (2014) 'A Computationally Efficient Method for the Design of the Heliostat Field for Solar Power Tower Plant'. *Renewable Energy* 69, 226-232

Besarati, S. M., Goswami, D. Y., and Stefanakos, E. K. (2014) 'Optimal Heliostat Aiming Strategy for Uniform Distribution of Heat Flux on the Receiver of a Solar Power Tower Plant'. *Energy Conversion and Management* 84, 234-243

Boito, P. and Grena, R. (2016) 'Optimization of the Geometry of Fresnel Linear Collectors'. *Solar Energy* 135, 479-486

Boukelia, T. E., Arslan, O., and Mecibah, M. S. (2016) 'ANN-Based Optimization of a Parabolic Trough Solar Thermal Power Plant'. *Applied Thermal Engineering* 107, 1210-1218

Burin, E., Lo Giudice, P., and Bazzo, E. (2018) 'Paper Mill Cogeneration Power Plant Assisted by Linear Fresnel Collectors'. *O Papel* 79, 86-89

Burkholder, F. and Kutscher, C. (2009) *Heat Loss Testing of Schott's 2008 PTR70 Parabolic Trough Receiver* [online] available from <https://www.osti.gov/servlets/purl/1369635>

Cagnoli, M., Mazzei, D., Procopio, M., Russo, V., Savoldi, L., and Zanino, R. (2018) 'Analysis of the Performance of Linear Fresnel Collectors: Encapsulated Vs. Evacuated Tubes'. *Solar Energy* 164, 119-138

Carrizosa, E., Domínguez-Bravo, C., Fernández-Cara, E., and Quero, M. (2015) 'A Heuristic Method for Simultaneous Tower and Pattern-Free Field Optimization on Solar Power Systems'. *Computers & Operations Research* 57, 109-122

Cengel, Y.A. (2003) *Heat Transfer : A Practical Approach* (2nd ed.). London: McGraw-Hill Education

Chaitanya Prasad, G. S., Reddy, K. S., and Sundararajan, T. (2017) 'Optimization of Solar Linear Fresnel Reflector System with Secondary Concentrator for Uniform Flux Distribution Over Absorber Tube'. *Solar Energy* 150, 1-12

Chemisana, D., Barrau, J., Rosell, J. I., Abdel-Mesih, B., Souliotis, M., and Badia, F. (2013) 'Optical Performance of Solar Reflective Concentrators: A Simple Method for Optical Assessment'. *Renewable Energy* 57, 120-129

Cheng, Z., Zhao, X., He, Y., and Qiu, Y. (2018) 'A Novel Optical Optimization Model for Linear Fresnel Reflector Concentrators'. *Renewable Energy* 129, 486-499

Choudhury, C. and Sehgal, H. K. (1986) 'A Fresnel Strip Reflector-Concentrator for Tubular Solar-Energy Collectors'. *Applied Energy* 23 (2), 143-154

Collado, F. J. and Guallar, J. (2016) 'Two-Stages Optimised Design of the Collector Field of Solar Power Tower Plants'. *Solar Energy* 135, 884-896

CSP Focus (2021) *Project Database* [online] available from <http://www.cspfocus.cn/en/study/> [Oct 2021]

Dabwan, Y. N. and Mokheimer, E. M. A. (2017) 'Optimal Integration of Linear Fresnel Reflector with Gas Turbine Cogeneration Power Plant'. *Energy Conversion and Management* 148, 830-843

Debnath, N., Deb, S. K., and Dutta, A. (2013) 'Frequency Band-Wise Passive Control of Linear Time Invariant Structural Systems with H∞ Optimization'. *Journal of Sound and Vibration* 332 (23), 6044-6062

Department for Business, Energy & Industrial Strategy (2018) *Clean Growth Strategy: Executive Summary* [online] available from <https://www.gov.uk/government/publications/clean-growth-strategy/clean-growth-strategy-executive-summary> [Nov 10, 2018]

Desai, N. B. and Bandyopadhyay, S. (2015) 'Optimization of Concentrating Solar Thermal Power Plant Based on Parabolic Trough Collector'. *Journal of Cleaner Production* 89, 262-271

Desai, N. B., Kedare, S. B., and Bandyopadhyay, S. (2014) 'Optimization of Design Radiation for Concentrating Solar Thermal Power Plants without Storage'. *Solar Energy* 107, 98-112

Desideri, U., Zepparelli, F., Morettini, V., and Garroni, E. (2013) 'Comparative Analysis of Concentrating Solar Power and Photovoltaic Technologies: Technical and Environmental Evaluations'. *Applied Energy* 102, 765-784

Deslauriers, M., Sorin, M., Marcos, B., and Richard, M. (2016) 'Retrofit of Low-Temperature Heat Recovery Industrial Systems using Multiobjective Exergoeconomic Optimization'. *Energy Conversion and Management* 130, 207-218

Dobos, A. P. (2017) *LK Scripting Language Reference* [online] available from <https://sam.nrel.gov/images/web_page_files/lk_guide.pdf> [Apr 12 2018]

Duan, X., He, C., Lin, X., Zhao, Y., and Feng, J. (2020) 'Quasi-Monte Carlo Ray Tracing Algorithm for Radiative Flux Distribution Simulation'. *Solar Energy* 211, 167-182

Duffie, J. A. and Beckman, W. A. (2013) *Solar Engineering of Thermal Processes* (4th ed.). New Jersey: John Wiley & Sons, Inc.

Escalante, E. S. R., Balestieri, J. A. P., and de Carvalho, J. A. (2022) 'The Organic Rankine Cycle: A Promising Technology for Electricity Generation and Thermal Pollution Mitigation'. *Energy* 247, 123405

EU Science Hub (2019) *JRC Photovoltaic Geographical Information System (PVGIS)* [online] available from <https://re.jrc.ec.europa.eu/pvg_tools/en/#TMY> [Aug 12, 2021]

Facão, J. and Oliveira, A. C. (2011) 'Numerical Simulation of a Trapezoidal Cavity Receiver for a Linear Fresnel Solar Collector Concentrator'. *Renewable Energy* 36 (1), 90-96

Fagan, E. M., Flanagan, M., Leen, S. B., Flanagan, T., Doyle, A., and Goggins, J. (2017) 'Physical Experimental Static Testing and Structural Design Optimisation for a Composite Wind Turbine Blade'. *Composite Structures* 164, 90-103

Farges, O., Bézian, J. J., and El Hafi, M. (2018) 'Global Optimization of Solar Power Tower Systems using a Monte Carlo Algorithm: Application to a Redesign of the PS10 Solar Thermal Power Plant'. *Renewable Energy* 119, 345-353

Farooqui, S. Z. (2015) 'Impact of Load Variation on the Energy and Exergy Efficiencies of a Single Vacuum Tube Based Solar Cooker'. *Renewable Energy* 77, 152-158

Forristall, R. (2003) *Heat Transfer Analysis and Modeling of a Parabolic Trough Solar Receiver Implemented in Engineering Equation Solver* [online] available from <http://www.osti.gov/scitech/biblio/15004820>

Gallego, A. J. and Camacho, E. F. (2018) 'On the Optimization of Flux Distribution with Flat Receivers: A Distributed Approach'. *Solar Energy* 160, 117-129

Gallego, A. J., Merello, G. M., Berenguel, M., and Camacho, E. F. (2019) 'Gain-Scheduling Model Predictive Control of a Fresnel Collector Field'. *Control Engineering Practice* 82, 1-13

Ghirardi, E., Brumana, G., Franchini, G., and Perdichizzi, A. (2021) 'Heliostat Layout Optimization for Load-Following Solar Tower Plants'. *Renewable Energy* 168, 393-405

Global Monitoring Laboratory (2021) *NOAA Solar Calculator* [online] available from <https://gml.noaa.gov/grad/antuv/SolarCalc.jsp> [Jun 23, 2021]

Glynn John, S. and Lakshmanan, T. (2017) 'Cost Optimization of Dish Solar Concentrators for Improved Scalability Decisions'. *Renewable Energy* 114, 600-613

Gordon, J. M. (2001) *Solar Energy : The State of the Art : ISES Position Papers*. London: James & James

Guo, J. and Huai, X. (2016) 'Multi-Parameter Optimization Design of Parabolic Trough Solar Receiver'. *Applied Thermal Engineering* 98, 73-79

Häberle, A., Zahler, C., Lerchenmüller, H., Mertins, M., Wittwer, C., Trieb, F., and Dersch, J. (2002) 'The Solarmundo Line Focussing Fresnel Collector. Optical and Thermal Performance and Cost Calculations'. in *SolarPACES International Symposium*.

Han, Z., Wang, J., Chen, H., and Wang, J. (2021) 'Thermodynamic Performance Analysis and Optimization for a Novel Full-Spectrum Solar-Driven Trigeneration System Integrated with Organic Rankine Cycle'. *Energy Conversion and Management* 245, 114626

Hassan, A., Al-Abdeli, Y. M., Masek, M., and Bass, O. (2022) 'Optimal Sizing and Energy Scheduling of Grid-Supplemented Solar PV Systems with Battery Storage: Sensitivity of Reliability and Financial Constraints'. *Energy* 238, 121780

Hoseinzadeh, H., Kasaeian, A., and Behshad Shafii, M. (2018) 'Geometric Optimization of Parabolic Trough Solar Collector Based on the Local Concentration Ratio using the Monte Carlo Method'. *Energy Conversion and Management* 175, 278-287

Hu, P. and Huang, W. (2018) 'Performance Analysis and Optimization of an Integrated Azimuth Tracking Solar Tower'. *Energy*

IEA (2021a) *Key World Energy Statistics 2021*: International Energy Agency (IEA)

IEA (2021b) *Concentrated Solar Power (CSP)*. Paris: International Energy Agency (IEA)

IEA (2010) *Technology Roadmap, Concentrating Solar Power*: International Energy Agency (IEA)

Incropera, F. P. and DeWitt, D. P. (2002) *Fundamentals of Heat and Mass Transfer*. 5th edn. New York; Chichester: New York; Chichester : Wiley

Industrial Solar GmbH (2021) *Fresnel Collector* [online] available from <https://www.industrial-solar.de/technologies/fresnel-collector/> [Apr 7, 2021]

IRENA (2020) *Renewable Power Generation Costs in 2020*. Abu Dhabi: International Renewable Energy Agency (IRENA)

Islam, M. T., Huda, N., Abdullah, A. B., and Saidur, R. (2018) 'A Comprehensive Review of State-of-the-Art Concentrating Solar Power (CSP) Technologies: Current Status and Research Trends'. *Renewable and Sustainable Energy Reviews* 91, 987-1018

Kandpal, T. C. and Mathur, S. S. (1985) 'A Note on the Calculation of Geometrical Concentration Ratio of a Cylindrical Parabolic Trough with a Flat Absorber'. *Solar & Wind Technology* 2 (1), 77-79

Kincaid, N., Mungas, G., Kramer, N., and Zhu, G. (2019) 'Sensitivity Analysis on Optical Performance of a Novel Linear Fresnel Concentrating Solar Power Collector'. *Solar Energy* 180, 383-390

Kincaid, N., Mungas, G., Kramer, N., Wagner, M., and Zhu, G. (2018) 'An Optical Performance Comparison of Three Concentrating Solar Power Collector Designs in Linear Fresnel, Parabolic Trough, and Central Receiver'. *Applied Energy* 231, 1109-1121

Li, C., Zhai, R., Liu, H., Yang, Y., and Wu, H. (2018) 'Optimization of a Heliostat Field Layout using Hybrid PSO-GA Algorithm'. *Applied Thermal Engineering* 128, 33-41

Li, Y., Khajepour, A., Devaud, C., and Liu, K. (2017) 'Power and Fuel Economy Optimizations of Gasoline Engines using Hydraulic Variable Valve Actuation System'. *Applied Energy* 206, 577-593

Lin, M., Sumathy, K., Dai, Y. J., Wang, R. Z., and Chen, Y. (2013) 'Experimental and Theoretical Analysis on a Linear Fresnel Reflector Solar Collector Prototype with V-Shaped Cavity Receiver'. *Applied Thermal Engineering* 51 (1), 963-972

Liu, M., Steven Tay, N. H., Bell, S., Belusko, M., Jacob, R., Will, G., Saman, W., and Bruno, F. (2016) 'Review on Concentrating Solar Power Plants and New Developments in High Temperature Thermal Energy Storage Technologies'. *Renewable and Sustainable Energy Reviews* 53, 1411-1432

López, J. C., Restrepo, Á, and Bazzo, E. (2018) 'Exergy Analysis of the Annual Operation of a Sugarcane Cogeneration Power Plant Assisted by Linear Fresnel Solar Collectors'. *Journal of Solar Energy Engineering* 140 (6), 061004

López-Alvarez, J. A., Larraneta, M., Silva-Pérez, M. A., and Lillo-Bravo, I. (2020) 'Impact of the Variation of the Receiver Glass Envelope Transmittance as a Function of the Incidence Angle in the Performance of a Linear Fresnel Collector'. *Renewable Energy* 150, 607-615

Lovegrove, K. and Csiro, W. S. (2012) '1 - Introduction to Concentrating Solar Power (CSP) Technology'. in *Concentrating Solar Power Technology*. ed. by Lovegrove, K. and Stein, W. : Woodhead Publishing, 3-15

Marugán-Cruz, C., Serrano, D., Gómez-Hernández, J., and Sánchez-Delgado, S. (2019) 'Solar Multiple Optimization of a DSG Linear Fresnel Power Plant'. *Energy Conversion and Management* 184, 571-580

Mathur, S. S., Kandpal, T. C., and Negi, B. S. (1991a) 'Optical Design and Concentration Characteristics of Linear Fresnel Reflector Solar concentrators—II. Mirror Elements of Equal Width'. *Energy Conversion and Management* 31 (3), 221-232

Mathur, S. S., Kandpal, T. C., and Negi, B. S. (1991b) 'Optical Design and Concentration Characteristics of Linear Fresnel Reflector Solar concentrators—I. Mirror Elements of Varying Width'. *Energy Conversion and Management* 31 (3), 205-219

McIntire, W. R. (1982) 'Factored Approximations for Biaxial Incident Angle Modifiers'. *Solar Energy* 29 (4), 315-322

Mertins, M. (2009) *Technische Und Wirtschaftliche Analyse Von Horizontalen Fresnel-Kollektoren*. [online] thesis or dissertation

Mills, D. R. (ed.) (2012) *6 - Linear Fresnel Reflector (LFR) Technology.*: Woodhead Publishing

Moaleman, A., Kasaeian, A., Aramesh, M., Mahian, O., Sahota, L., and Nath Tiwari, G. (2018) 'Simulation of the Performance of a Solar Concentrating Photovoltaic-Thermal Collector, Applied in a Combined Cooling Heating and Power Generation System'. *Energy Conversion and Management* 160, 191-208

Moghimi, M. A., Craig, K. J., and Meyer, J. P. (2017) 'Simulation-Based Optimisation of a Linear Fresnel Collector Mirror Field and Receiver for Optical, Thermal and Economic Performance'. *Solar Energy* 153, 655-678

Moghimi, M. A., Craig, K. J., and Meyer, J. P. (2015) 'Optimization of a Trapezoidal Cavity Absorber for the Linear Fresnel Reflector'. *Solar Energy* 119, 343-361

Montes, M. J., Rubbia, C., Abbas, R., and Martínez-Val, J. M. (2014) 'A Comparative Analysis of Configurations of Linear Fresnel Collectors for Concentrating Solar Power'. *Energy* 73, 192-203

Morin, G., Dersch, J., Platzer, W., Eck, M., and Häberle, A. (2012) 'Comparison of Linear Fresnel and Parabolic Trough Collector Power Plants'. *Solar Energy* 86 (1), 1-12

Morin, G., Platzer, W., Eck, M., Uhlig, R., Häberle, A., Berger, M., and Zarza, E. (2006) 'Road Map Towards the Demonstration of a Linear Fresnel Collector using Single Tube Receiver'. in *13th International Symposium on Concentrated Solar Power and Chemical Energy Technologies*. held 2006-06-20. Seville (Spain)

Moya, E. Z. (2012) '7 - Parabolic-Trough Concentrating Solar Power (CSP) Systems'. in *Concentrating Solar Power Technology*. ed. by Lovegrove, K. and Stein, W. : Woodhead Publishing, 197-239

Natarajan, S. K., Reddy, K. S., and Mallick, T. K. (2012) 'Heat Loss Characteristics of Trapezoidal Cavity Receiver for Solar Linear Concentrating System'. *Applied Energy* 93, 523-531

Nixon, J. D. and Davies, P. A. (2012) 'Cost-Exergy Optimisation of Linear Fresnel Reflectors'. *Solar Energy* 86 (1), 147-156

Nixon, J. D., Dey, P. K., and Davies, P. A. (2013) 'Design of a Novel Solar Thermal Collector using a Multi-Criteria Decision-Making Methodology'. *Journal of Cleaner Production* 59, 150-159

Nixon, J. D. (2012) *Solar Thermal Collectors for use in Hybrid Solar-Biomass Power Plants in India*. [online] thesis or dissertation

NREL (2021) *Linear Fresnel | Concentrating Solar Power Projects* [online] available from <https://solarpaces.nrel.gov/by-technology/linear-fresnel> [Oct 7, 2021]

Pulido-Iparraguirre, D., Valenzuela, L., Serrano-Aguilera, J., and Fernández-García, A. (2019) 'Optimized Design of a Linear Fresnel Reflector for Solar Process Heat Applications'. *Renewable Energy* 131, 1089-1106

Pye, J. D. (2008) *System Modelling of the Compact Linear Fresnel Reflector*. [online] thesis or dissertation

Qiu, Y., Li, M., Wang, K., Liu, Z., and Xue, X. (2017) 'Aiming Strategy Optimization for Uniform Flux Distribution in the Receiver of a Linear Fresnel Solar Reflector using a Multi-Objective Genetic Algorithm'. *Applied Energy* 205, 1394-1407

Qiu, Y., He, Y., Wu, M., and Zheng, Z. (2016) 'A Comprehensive Model for Optical and Thermal Characterization of a Linear Fresnel Solar Reflector with a Trapezoidal Cavity Receiver'. *Renewable Energy* 97, 129-144

Qiu, Y., He, Y., Cheng, Z., and Wang, K. (2015) 'Study on Optical and Thermal Performance of a Linear Fresnel Solar Reflector using Molten Salt as HTF with MCRT and FVM Methods'. *Applied Energy* 146, 162-173

Reddy, K. S. and Kumar, K. R. (2014) 'Estimation of Convective and Radiative Heat Losses from an Inverted Trapezoidal Cavity Receiver of Solar Linear Fresnel Reflector System'. *International Journal of Thermal Sciences* 80, 48-57

Reliance Power Limited (2018) *Dhursar Solar Power Plant* [online] available from <https://www.protenders.com/companies/reliance-power-limited/projects/dhursar-solar-power-plant> [Nov 5, 2018]

RIOGLASS Solar (2020) *HCE Tubes* [online] available from <https://www.rioglass.com/our-products/hce-tubes.html> [Jul 20, 2021]

Rizvi, A. A., Danish, S. N., El-Leathy, A., Al-Ansary, H., and Yang, D. (2021) 'A Review and Classification of Layouts and Optimization Techniques used in Design of Heliostat Fields in Solar Central Receiver Systems'. *Solar Energy* 218, 296-311

Romero, M., Gonzalez-Aguilar, J., and Zarza, E. (2015) 'Concentrating Solar Thermal Power'. in *Energy Efficiency and Renewable Energy Handbook*. ed. by Goswami, D. Y. and Kreith, F. Boca Raton: CRC Press, 1237-1246

Roostaee, A. and Ameri, M. (2019) 'Effect of Linear Fresnel Concentrators Field Key Parameters on Reflectors Configuration, Trapezoidal Cavity Receiver Dimension, and Heat Loss'. *Renewable Energy* 134, 1447-1464

Rungasamy, A. E., Craig, K. J., and Meyer, J. P. (2019) 'Comparative Study of the Optical and Economic Performance of Etendue-Conserving Compact Linear Fresnel Reflector Concepts'. *Solar Energy* 181, 95-107

Saghafifar, M., Gadalla, M., and Mohammadi, K. (2019) 'Thermo-Economic Analysis and Optimization of Heliostat Fields using AINEH Code: Analysis of Implementation of Non-Equal Heliostats (AINEH)'. *Renewable Energy* 135, 920-935

Sahoo, S. S., Singh, S., and Banerjee, R. (2012) 'Analysis of Heat Losses from a Trapezoidal Cavity used for Linear Fresnel Reflector System'. *Solar Energy* 86 (5), 1313-1322

Sánchez, M., Clifford, B., and Nixon, J. D. (2018) 'Modelling and Evaluating a Solar Pyrolysis System'. *Renewable Energy* 116, 630-638

Sassi, G. (1983) 'Some Notes on Shadow and Blockage Effects'. *Solar Energy* 31 (3), 331-333

Schiel, W. and Keck, T. (2012) '9 - Parabolic Dish Concentrating Solar Power (CSP) Systems'. in *Concentrating Solar Power Technology*. ed. by Lovegrove, K. and Stein, W. : Woodhead Publishing, 284-322

SCHOTT solar (2013) *SCHOTT PTR®70 Receiver*. Mainz, Germany: SCHOTT Solar CSP GmbH

Serag-Eldin, M. (2014) 'Thermal Design of a Roof-Mounted CLFR Collection System for a Desert Absorption Chiller'. *Null* 33 (3), 506-524

Shahin, M. S., Orhan, M. F., and Uygul, F. (2016) 'Thermodynamic Analysis of Parabolic Trough and Heliostat Field Solar Collectors Integrated with a Rankine Cycle for Cogeneration of Electricity and Heat'. *Solar Energy* 136, 183-196

Sharan, P. and Bandyopadhyay, S. (2017) 'Solar Assisted Multiple-Effect Evaporator'. *Journal of Cleaner Production* 142, 2340-2351

Singh, P. L., Sarviya, R. M., and Bhagoria, J. L. (2010) 'Heat Loss Study of Trapezoidal Cavity Absorbers for Linear Solar Concentrating Collector'. *Energy Conversion and Management* 51 (2), 329-337

Singh, R. N., Mathur, S. S., and Kandpal, T. C. (1980) 'Some Geometrical Design Aspects of a Linear Fresnel Reflector Concentrator'. *Energy Research* 4, 59-67

Sirimanna, M. P. G., Nixon, J. D., and Innocente, M. S. (2022) 'Performance of Different Optimization Solvers for Designing Solar Linear Fresnel Reflector Power Generation Systems'. in *3rd International Conference on Energy and Sustainable Futures (ICESF)*. held Sep 7-8, 2022. Coventry, United Kingdom

Sirimanna, M. P. G. and Nixon, J. D. (2020) 'Effects of Mirror Geometry on the Optical Efficiency of a Linear Fresnel Reflector (LFR)'. in *Renewable Energy and Sustainable Buildings. Innovative Renewable Energy*. ed. by Sayigh, A. : Springer, Cham, 337-347

Sun, J., Liu, Q., and Duan, Y. (2018) 'Effects of Evaporator Pinch Point Temperature Difference on Thermo-Economic Performance of Geothermal Organic Rankine Cycle Systems'. *Geothermics* 75, 249-258

SUNCNIM (2019) *Inauguration Llo* [online] available from <https://cnim.com/en/medias/suncnim-and-banque-des-territoires-inaugurated-worlds-first-fresnel-type-thermodynamic-solar> [Oct 2021]

Sutter, F., Montecchi, M., von Dahlen, H., Fernández-García, A., and Röger, M. (2018) 'The Effect of Incidence Angle on the Reflectance of Solar Mirrors'. *Solar Energy Materials and Solar Cells* 176, 119-133

Tesfamichael, T. and Wäckelgård, E. (2000) 'Angular Solar Absorptance and Incident Angle Modifier of Selective Absorbers for Solar Thermal Collectors'. *Solar Energy* 68 (4), 335-341

Tsai, C. (2016) 'Optimized Solar Thermal Concentrator System Based on Free-Form Trough Reflector'. *Solar Energy* 125, 146-160

U.S. Department of Energy (2010) *Concentrating Solar Power Commercial Application Study: Reducing Water Consumption of Concentrating Solar Power Electricity Generation*. Washington, DC: United States. Department of Energy

U.S. Department of Energy (2003) *Parabolic Trough Solar Thermal Electric Power Plants*. United States: USDOE

U.S. Energy Information Administration (2021) *International Energy Outlook 2021*

United Nations Climate Change (2018) *What is the Paris Agreement?* [online] available from <https://unfccc.int/process-and-meetings/the-paris-agreement/what-is-the-paris-agreement> [Nov 10, 2018]

United Sun Systems International Ltd. (2012). File:Maricopa Dish-Stirling plant 03. [Photograph]. Wikimedia Commons. available from <https://commons.wikimedia.org/w/index.php?curid=39971729>

Vasallo, M. J. and Bravo, J. M. (2016) 'A MPC Approach for Optimal Generation Scheduling in CSP Plants'. *Applied Energy* 165, 357-370

Wang, A., Han, X., Liu, M., Yan, J., and Liu, J. (2019) 'Thermodynamic and Economic Analyses of a Parabolic Trough Concentrating Solar Power Plant Under Off-Design Conditions'. *Applied Thermal Engineering* 156, 340-350

Wang, J., Duan, L., and Yang, Y. (2018) 'An Improvement Crossover Operation Method in Genetic Algorithm and Spatial Optimization of Heliostat Field'. *Energy* 155, 15-28

Wang, K., He, Y., Xue, X., and Du, B. (2017) 'Multi-Objective Optimization of the Aiming Strategy for the Solar Power Tower with a Cavity Receiver by using the Non-Dominated Sorting Genetic Algorithm'. *Applied Energy* 205, 399-416

Wang, K., He, Y., Qiu, Y., and Zhang, Y. (2016) 'A Novel Integrated Simulation Approach Couples MCRT and Gebhart Methods to Simulate Solar Radiation Transfer in a Solar Power Tower System with a Cavity Receiver'. *Renewable Energy* 89, 93-107

Wang, X. D., Zhao, L., Wang, J. L., Zhang, W. Z., Zhao, X. Z., and Wu, W. (2010) 'Performance Evaluation of a Low-Temperature Solar Rankine Cycle System Utilizing R245fa'. *Solar Energy* 84 (3), 353-364

Wang, Y., He, Y., Mei, D., and Tao, W. (2011) 'Optimization Design of Slotted Fin by Numerical Simulation Coupled with Genetic Algorithm'. *Applied Energy* 88 (12), 4441-4450

Wendelin, T., Dobos, A., and Lewandowski, A. (2013) *SolTrace: A Ray-Tracing Code for Complex Solar Optical Systems*. United States

Xie, Q., Guo, Z., Liu, D., Chen, Z., Shen, Z., and Wang, X. (2021) 'Optimization of Heliostat Field Distribution Based on Improved Gray Wolf Optimization Algorithm'. *Renewable Energy* 176, 447-458

Yan, H., Wang, A., Chong, D., Liu, M., Liu, J., and Yan, J. (2021) 'Review on Performance Analysis of the Power Block in Concentrated Solar Power Plants'. *Energy Technology* 9 (1), 2000621

Yan, J., Peng, Y., and Cheng, Z. (2018) 'Optimization of a Discrete Dish Concentrator for Uniform Flux Distribution on the Cavity Receiver of Solar Concentrator System'. *Renewable Energy* 129, 431-445

Yang, S., Lee, K., and Lee, I. (2020) 'Pattern-Free Heliostat Field Layout Optimization using Physics-Based Gradient'. *Solar Energy* 206, 722-731

Yang, S., Sensoy, T. S., and Ordonez, J. C. (2018) 'Dynamic 3D Volume Element Model of a Parabolic Trough Solar Collector for Simulation and Optimization'. *Applied Energy* 217, 509-526

Zhang, H. L., Baeyens, J., Degrève, J., and Cacères, G. (2013) 'Concentrated Solar Power Plants: Review and Design Methodology'. *Renewable and Sustainable Energy Reviews* 22, 466-481

Zheng, H. (2017) 'Chapter 2 - Solar Energy Utilization and its Collection Devices'. in *Solar Energy Desalination Technology*. ed. by Zheng, H. Amsterdam: Elsevier, 47-171

Zhu, G., Wendelin, T., Wagner, M. J., and Kutscher, C. (2014) 'History, Current State, and Future of Linear Fresnel Concentrating Solar Collectors'. *Solar Energy* 103, 639-652

Zhu, G. (2013) 'Development of an Analytical Optical Method for Linear Fresnel Collectors'. *Solar Energy* 94, 240-252

Ziółkowski, P., Hyrzyński, R., Lemański, M., Kraszewski, B., Bykuć, S., Głuch, S., Sowiżdżał, A., Pająk, L., Wachowicz-Pyzik, A., and Badur, J. (2021) 'Different Design Aspects of an Organic Rankine Cycle Turbine for Electricity Production using a Geothermal Binary Power Plant'. *Energy Conversion and Management* 246, 114672

# Appendix A

This is one of the eight Matlab codes required to run the LFR design optimization framework. Purpose of this code was to generate primary mirror field and receiver geometrical data needed to run SolTrace. A LK scripting has been written to import the geometrical data provided by Matlab and to run ray tracing.

```
function  mirrorgen_v2(h,nmax,Dr,sm,wm,theta_T,fn)
 %this code generates the mirror field and receiver data set for soltrace


%get variables and fix relevant parameters
wr=Dr;% wr and Dr is based on the receiver type used; wr-trapezoidal; Dr-single tube
d_cp=0.12; %considering a fixed cavity depth, gap between the absorber plate and glass cover
t_g=0.003; %3mm cover glass
%AsR=3; %ratio between receiver width/gap
sm1=sm; %gap between fist two mirrors under the receiver
%qmfw= (sm1/2 + (nmax/2-1)*(wm+sm) + wm/2)/2; %mid point of one side of the mirror field
%fn=sqrt(qmfw*qmfw + h*h);%calculate a single focal length
theta_T=deg2rad(theta_T); %convert degree to radian


%assign arrays to save data
mirror_array=zeros(nmax,11);%for mirror field data
collecor_array=zeros(5,11);%for collector data
extra_array=zeros(1,11);%for other additional data
extra_array(1,1)=theta_T; %passing transverse angle


 %generating receiver and collector based on input design variables
        %define mirror field
        mirror_array(:,2)=0; %Y
        mirror_array(:,3)=0; %Z
        mirror_array(:,5)=0; %Yaimpoint
        mirror_array(:,6)=h; %Zaimpoint
        mirror_array(:,7)=0; %Zrotation
        mirror_array(:,8)=wm; %Aperture
        mirror_array(:,9)=1; %Aperture/plant width
        mirror_array(:,10)=fn; %focus of curved surface
        mirror_array(:,11)=0; %flat surface

        %define collector
        collecor_array(:,2)=0; %Y
        collecor_array(:,5)=0; %Yaimpoint
        collecor_array(:,6)=h; %Zaimpoint
        collecor_array(:,7)=0; %Zrotation
        collecor_array(:,9)=1; %Aperture/plant width
        collecor_array(:,10)=0; %flat surface1
        collecor_array(:,11)=0; %flat surface
```

```
%generating receiver and collector for different number of mirrors

        for n=2:2:nmax %generate mirror number set, code written for an even number of mirrors

        %define mirror field
        hmfw= sm1/2 + (n/2-1)*(wm+sm) + wm/2; %half mirror field width, distance between the
center points of the first and the last mirror
        beta_L=(theta_T-atan(hmfw/h))/2; %negative/west side of mirror field
        beta_R=(theta_T+atan(hmfw/h))/2; %negative/west side of mirror field

        Xaimpt_L=hmfw+h*tan(beta_L);
        Xaimpt_R=hmfw-h*tan(beta_R);

        mirror_array((nmax-n+2)/2,1)=-hmfw; %X negative x
        mirror_array((nmax+n)/2,1)=hmfw; %X possitive x
        mirror_array((nmax-n+2)/2,4)=-Xaimpt_L; %Xaimpoint negative x
        mirror_array((nmax+n)/2,4)=Xaimpt_R; %Xaimpoint possitive x
        %mirror_array((nmax-n+2)/2,8)=wm*cos((atan(hmfw/h))/2); %aperture negative x
        %mirror_array((nmax+n)/2,8)=wm*cos((atan(hmfw/h))/2); %aperture positive x

        n_mirror_array=mirror_array((nmax-n+2)/2:(nmax+n)/2,:); %selecting mirror array

        %define collector

        %d_cp=wr/AsR;% d_cp, gap between the absorber plate and glass cover
        theta_1=asin(hmfw/(sqrt(h^2+hmfw^2)));
        theta_2=asin((wm/2)/(sqrt(h^2+hmfw^2)));
        phi= (pi/2) - (theta_1+theta_2); %cavity wall inclination; slope

        collecor_array(1,1)= 0; %X absorber
        collecor_array(2,1)= -(wr/2 + d_cp/2/tan(phi)); %X negative x, left wall
        collecor_array(3,1)= (wr/2 + d_cp/2/tan(phi)); %X possitive x, right wall
        collecor_array(4,1)= 0; %X glass cover top
        collecor_array(5,1)= 0; %X glass cover bottom/mirror side

        collecor_array(1,3)= h; %Z absorber
        collecor_array(2,3)= h-d_cp/2; %Z left wall
        collecor_array(3,3)= h-d_cp/2; %Z right wall
        collecor_array(4,3)= h-d_cp; %Z glass cover top
        collecor_array(5,3)= h-d_cp-t_g; %Z glass cover bottom/mirror side

        collecor_array(1,4)= 0; %Xaimpoint absorber
        collecor_array(2,4)= -(wr/2 + d_cp/2/sin(phi)/cos(phi)); %Xaimpoint left wall
        collecor_array(3,4)= (wr/2 + d_cp/2/sin(phi)/cos(phi)); %Xaimpoint right wall
        collecor_array(4,4)= 0; %Xaimpoint glass cover top
        collecor_array(5,4)= 0; %Xaimpoint glass cover bottom/mirror side

        collecor_array(1,6)=(h+1); %Zaimpoint; to avoid Z and Zaimpoint being coincided

        collecor_array(1,8)= wr; %apature absorber
        collecor_array(2,8)= (d_cp/sin(phi)); %apature left wall
        collecor_array(3,8)= (d_cp/sin(phi)); %apature right wall
        collecor_array(4,8)= (wr + 2*d_cp/tan(phi)); %apature glass cover top
        collecor_array(5,8)= (wr + 2*d_cp/tan(phi)); %apature glass cover bottom/mirror side

        out_array=round([n_mirror_array;collecor_array],3);
```

```
        end

        out_array=round([out_array;extra_array],3);

%saving data to a txt file
dlmwrite('mfield.txt', out_array,'Delimiter','\t','newline','pc');
```

Running SolTrace from command prompt or any other platform such as Matlab can be essential in a complex modelling work. The following is an example command line that shows how this can be achieved using Matlab without using complex linking methods.

```
system('"C:\SolTrace\2012.7.9\SolTrace.exe" -s "C:\Users\sirimanm\Desktop\DR\3rd year\codes\20201112CPC.lk"'); % run soltrace from Matlab
```

Technical specification

| Components | Specification |
|---|---|
| Dimension | • length: 4060 mm at 20 °C ambient temperature (159.8 inches at 68 °F)<br>• aperture length: > 96.7 % of the bulk length at 350 °C / 662 °F working temperature |
| Absorber | • outer diameter: 70 mm / 2.75 inches<br>• steel-type: DIN 1.4541 or similar<br>• solar absorptance:<br>$\alpha_{ISO} \geq 95.5\%$<br>$\alpha_{ASTM} \geq 96\%$<br>• thermal emittance: $\varepsilon \leq 9.5\%$ |
| Glass envelope | • Borosilicate glass<br>• outer diameter: 125 mm / 4.9 inches<br>• antireflective coating<br>• solar transmittance: $\tau \geq 97\%$ |
| Thermal losses | • in conjunction with SCHOTT Solar CSP patented shields<br>< 250 W/m (@ 400 °C)<br>< 165 W/m (@ 350 °C)<br>< 110 W/m (@ 300 °C)<br><  70 W/m (@ 250 °C) |
| Vacuum | • residual gas pressure: $\leq 10^{-3}$ mbar |
| Heat transfer fluid | • non-corrosive thermal oil with an effective partial pressure of dissolved Hydrogen of $p_{H2} < 30$ Pa |
| Operating pressure | • ≤ 41 bar (absolute) |

Thermal losses

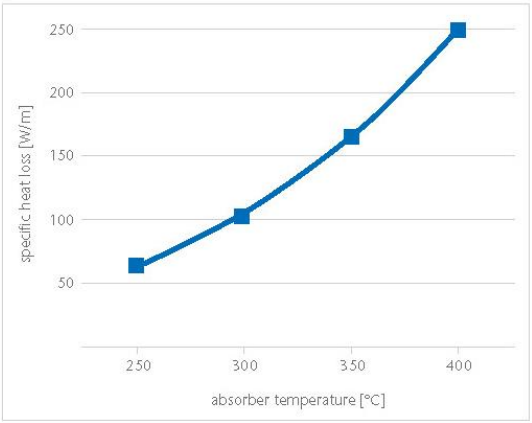


Figure Appendix A.1: Technical specifications of PTR®70 receiver tube used for modelling

# Appendix B

Table Appendix B.1: Starting points and optimized results for interior point and SQP algorithms for default stopping criteria

| Interior point algorithm | | | SQP algorithm | | |
|---|---|---|---|---|---|
| Starting point (m) | Optimum $h_r$ (m) | Max $\eta_{total,th}$ | Starting point (m) | Optimum $h_r$ (m) | Max $\eta_{total,th}$ |
| 24.81226 | 13.45124 | 0.216286 | 24.81226 | 24.81368 | 0.247707 |
| 27.36217 | 19.83134 | 0.24571 | 27.36217 | 27.36195 | 0.24727 |
| 5.555631 | 5.555484 | 0.099056 | 5.555631 | 5.560258 | 0.098922 |
| 27.57452 | 14.85076 | 0.225447 | 27.57452 | 27.56443 | 0.246869 |
| 19.70606 | 19.83028 | 0.244955 | 19.70606 | 19.70705 | 0.244419 |
| 4.731131 | 17.27246 | 0.237127 | 4.731131 | 4.732666 | 0.078588 |
| 9.79795 | 9.793423 | 0.178155 | 9.79795 | 9.793642 | 0.178611 |
| 17.31268 | 19.55012 | 0.243966 | 17.31268 | 17.31615 | 0.236464 |
| 28.81019 | 28.81316 | 0.245778 | 28.81019 | 28.81564 | 0.245942 |
| 29.01688 | 29.01969 | 0.246437 | 29.01688 | 29.01684 | 0.246128 |
| 6.413166 | 6.413166 | 0.118769 | 6.413166 | 6.414716 | 0.11862 |
| 29.1766 | 29.17826 | 0.245972 | 29.1766 | 29.17496 | 0.246407 |
| 28.80067 | 28.74749 | 0.246238 | 28.80067 | 28.80181 | 0.246424 |
| 15.59052 | 19.29316 | 0.243481 | 15.59052 | 15.59328 | 0.229089 |
| 24.40785 | 15.02757 | 0.225964 | 24.40785 | 24.40773 | 0.248441 |
| 5.972817 | 18.50725 | 0.240278 | 5.972817 | 5.972328 | 0.109259 |
| 13.80932 | 20.54982 | 0.247803 | 13.80932 | 13.80863 | 0.219366 |
| 27.64059 | 26.89027 | 0.248054 | 27.64059 | 27.63358 | 0.247646 |
| 24.18181 | 24.20838 | 0.249331 | 24.18181 | 23.96689 | 0.248823 |
| 28.86579 | 28.83587 | 0.245762 | 28.86579 | 28.86564 | 0.24585 |
| 20.36074 | 20.44159 | 0.247881 | 20.36074 | 20.36203 | 0.246369 |
| 2.999927 | 18.13249 | 0.239404 | 2.999927 | 2.997908 | 0.033405 |
| 25.77562 | 20.28293 | 0.247189 | 25.77562 | 25.78108 | 0.248598 |
| 28.15181 | 26.23068 | 0.24925 | 28.15181 | 28.15329 | 0.246798 |
| 21.00458 | 18.63845 | 0.241076 | 21.00458 | 21.00458 | 0.248129 |
| 23.21672 | 21.10763 | 0.248817 | 23.21672 | 23.22393 | 0.24911 |
| 22.80771 | 17.45378 | 0.237105 | 22.80771 | 22.80771 | 0.24877 |

| | | | | | |
|---|---|---|---|---|---|
| 12.98236 | 18.84466 | 0.242829 | 12.98236 | 12.98025 | 0.212628 |
| 20.35338 | 19.43661 | 0.243974 | 20.35338 | 20.35232 | 0.247503 |
| 6.793227 | 19.04078 | 0.242725 | 6.793227 | 6.787688 | 0.126387 |
| 21.76929 | 19.20968 | 0.243359 | 21.76929 | 21.77867 | 0.24889 |
| 2.89132 | 14.07336 | 0.221623 | 2.89132 | 2.892308 | 0.030434 |
| 9.753844 | 9.746044 | 0.178124 | 9.753844 | 9.753844 | 0.178263 |
| 3.292799 | 19.89084 | 0.246008 | 3.292799 | 3.292458 | 0.040508 |
| 4.71969 | 4.717823 | 0.077956 | 4.71969 | 4.72026 | 0.078176 |
| 25.05682 | 18.67019 | 0.241523 | 25.05682 | 25.05051 | 0.249241 |
| 21.4552 | 16.60782 | 0.233734 | 21.4552 | 21.48285 | 0.249048 |
| 10.87879 | 19.83164 | 0.246323 | 10.87879 | 10.87875 | 0.193291 |
| 28.60622 | 19.6109 | 0.24426 | 28.60622 | 28.60265 | 0.246102 |
| 2.96449 | 2.96449 | 0.032419 | 2.96449 | 2.96336 | 0.032397 |
| 14.28484 | 20.30682 | 0.246931 | 14.28484 | 14.28695 | 0.221431 |
| 12.68364 | 12.62151 | 0.209779 | 12.68364 | 12.68566 | 0.210128 |
| 23.43447 | 18.10263 | 0.240349 | 23.43447 | 23.44195 | 0.24922 |
| 24.2656 | 24.30493 | 0.249071 | 24.2656 | 24.28244 | 0.248934 |
| 7.232433 | 7.230509 | 0.135395 | 7.232433 | 7.232192 | 0.135405 |
| 15.7134 | 15.67399 | 0.230245 | 15.7134 | 15.71532 | 0.229329 |
| 14.47641 | 14.46413 | 0.223803 | 14.47641 | 14.47392 | 0.223001 |
| 20.09676 | 19.46254 | 0.245342 | 20.09676 | 20.09676 | 0.246132 |
| 21.86222 | 16.91846 | 0.235477 | 21.86222 | 21.86536 | 0.248441 |
| 23.13123 | 18.00697 | 0.239146 | 23.13123 | 23.13202 | 0.249146 |
| 9.728702 | 19.58212 | 0.244962 | 9.728702 | 9.728688 | 0.177791 |
| 21.03167 | 18.64608 | 0.24108 | 21.03167 | 21.03 | 0.248616 |
| 20.34274 | 17.62573 | 0.238008 | 20.34274 | 20.34439 | 0.247224 |
| 6.553129 | 6.545505 | 0.121662 | 6.553129 | 6.554046 | 0.121742 |
| 5.331935 | 19.02588 | 0.242731 | 5.331935 | 5.332491 | 0.093065 |
| 15.95419 | 15.94642 | 0.231197 | 15.95419 | 15.95295 | 0.231699 |
| 28.87283 | 28.57784 | 0.246939 | 28.87283 | 28.87451 | 0.246365 |
| 11.5308 | 11.53043 | 0.200388 | 11.5308 | 11.5308 | 0.199249 |
| 18.3875 | 18.3875 | 0.240755 | 18.3875 | 18.37834 | 0.240315 |
| 8.266734 | 19.9136 | 0.245935 | 8.266734 | 8.264175 | 0.154176 |

Table Appendix B.2: Starting points and optimized results for interior point and SQP algorithms for a specific stopping criteria

| SQP algorithm | | | Active set algorithm | | |
|---|---|---|---|---|---|
| Starting point (m) | Optimum $h_r$ (m) | Max $\eta_{total,th}$ | Starting point (m) | Optimum $h_r$ (m) | Max $\eta_{total,th}$ |
| 24.81226 | 24.82412 | 0.248398 | 24.81226 | 24.09938 | 0.249444 |
| 27.36217 | 27.3746 | 0.247222 | 27.36217 | 21.44605 | 0.248752 |
| 5.555631 | 5.555784 | 0.098758 | 5.555631 | 5.552213 | 0.099099 |
| 27.57452 | 27.57452 | 0.247858 | 27.57452 | 22.0575 | 0.249166 |
| 19.70606 | 19.70606 | 0.245023 | 19.70606 | 25.25674 | 0.248539 |
| 4.731131 | 4.731701 | 0.078084 | 4.731131 | 4.730798 | 0.077916 |
| 9.79795 | 9.791728 | 0.177981 | 9.79795 | 30 | 0.245525 |
| 17.31268 | 17.31264 | 0.236256 | 17.31268 | 23.00389 | 0.249038 |
| 28.81019 | 28.8112 | 0.245763 | 28.81019 | 29.37084 | 0.246065 |
| 29.01688 | 29.02915 | 0.246562 | 29.01688 | 23.0438 | 0.248971 |
| 6.413166 | 6.413873 | 0.118048 | 6.413166 | 6.395391 | 0.117898 |
| 29.1766 | 29.17654 | 0.246217 | 29.1766 | 22.02427 | 0.249612 |
| 28.80067 | 28.80328 | 0.245763 | 28.80067 | 28.87563 | 0.245851 |
| 15.59052 | 15.58868 | 0.228736 | 15.59052 | 30 | 0.24406 |
| 24.40785 | 24.40811 | 0.248406 | 24.40785 | 23.00736 | 0.24887 |
| 5.972817 | 5.972802 | 0.109336 | 5.972817 | 5.957299 | 0.108083 |
| 13.80932 | 13.8047 | 0.21901 | 13.80932 | 23.14956 | 0.249285 |
| 27.64059 | 27.64444 | 0.24743 | 27.64059 | 20.887 | 0.247959 |
| 24.18181 | 24.1834 | 0.249443 | 24.18181 | 21.40908 | 0.249292 |
| 28.86579 | 28.86582 | 0.245545 | 28.86579 | 21.83447 | 0.248789 |
| 20.36074 | 20.36228 | 0.246143 | 20.36074 | 20.35679 | 0.24757 |
| 2.999927 | 3.000261 | 0.033232 | 2.999927 | 22.9521 | 0.249265 |
| 25.77562 | 25.77332 | 0.249096 | 25.77562 | 26.33306 | 0.248183 |
| 28.15181 | 28.15181 | 0.245977 | 28.15181 | 23.53909 | 0.248676 |
| 21.00458 | 21.01481 | 0.248377 | 21.00458 | 23.34007 | 0.249122 |
| 23.21672 | 23.21668 | 0.248425 | 23.21672 | 21.89068 | 0.249672 |
| 22.80771 | 22.80466 | 0.24891 | 22.80771 | 22.07876 | 0.24834 |
| 12.98236 | 12.98234 | 0.211574 | 12.98236 | 12.96081 | 0.21252 |
| 20.35338 | 20.35348 | 0.246872 | 20.35338 | 20.06658 | 0.246377 |
| 6.793227 | 6.793461 | 0.127651 | 6.793227 | 25.26814 | 0.248481 |
| 21.76929 | 21.77035 | 0.249031 | 21.76929 | 21.76959 | 0.249654 |

| | | | | | |
|---|---|---|---|---|---|
| 2.89132 | 2.890304 | 0.03046 | 2.89132 | 30 | 0.243188 |
| 9.753844 | 9.753758 | 0.177806 | 9.753844 | 21.77502 | 0.248559 |
| 3.292799 | 3.292849 | 0.040165 | 3.292799 | 3.292168 | 0.040547 |
| 4.71969 | 4.71969 | 0.077761 | 4.71969 | 4.714381 | 0.077853 |
| 25.05682 | 25.06076 | 0.248198 | 25.05682 | 23.76855 | 0.248864 |
| 21.4552 | 21.45252 | 0.24839 | 21.4552 | 26.1058 | 0.249506 |
| 10.87879 | 10.88009 | 0.19219 | 10.87879 | 26.64125 | 0.247945 |
| 28.60622 | 26.25067 | 0.248501 | 28.60622 | 21.71121 | 0.24955 |
| 2.96449 | 2.966267 | 0.032208 | 2.96449 | 2.964491 | 0.032096 |
| 14.28484 | 14.28914 | 0.221951 | 14.28484 | 30 | 0.244132 |
| 12.68364 | 12.68159 | 0.210517 | 12.68364 | 27.0738 | 0.247814 |
| 23.43447 | 23.43584 | 0.24828 | 23.43447 | 21.46685 | 0.248974 |
| 24.2656 | 24.27486 | 0.250135 | 24.2656 | 24.17556 | 0.249583 |
| 7.232433 | 7.231731 | 0.135571 | 7.232433 | 7.222532 | 0.135879 |
| 15.7134 | 15.71338 | 0.230074 | 15.7134 | 25.53541 | 0.248637 |
| 14.47641 | 14.47641 | 0.22273 | 14.47641 | 25.31969 | 0.248727 |
| 20.09676 | 20.09455 | 0.246727 | 20.09676 | 19.95541 | 0.245666 |
| 21.86222 | 21.86596 | 0.249318 | 21.86222 | 24.08739 | 0.247593 |
| 23.13123 | 23.13311 | 0.248664 | 23.13123 | 20.57237 | 0.248468 |
| 9.728702 | 9.722319 | 0.177467 | 9.728702 | 9.698514 | 0.177444 |
| 21.03167 | 21.03413 | 0.247567 | 21.03167 | 20.58794 | 0.248625 |
| 20.34274 | 20.33719 | 0.246839 | 20.34274 | 25.70992 | 0.24843 |
| 6.553129 | 6.553653 | 0.122025 | 6.553129 | 30 | 0.243251 |
| 5.331935 | 5.335387 | 0.093416 | 5.331935 | 30 | 0.24371 |
| 15.95419 | 15.95605 | 0.23112 | 15.95419 | 15.95419 | 0.231436 |
| 28.87283 | 28.87283 | 0.245877 | 28.87283 | 23.27781 | 0.249407 |
| 11.5308 | 11.53207 | 0.199382 | 11.5308 | 26.31445 | 0.248449 |
| 18.3875 | 18.44263 | 0.240706 | 18.3875 | 25.01483 | 0.248743 |
| 8.266734 | 8.25945 | 0.154352 | 8.266734 | 8.230214 | 0.15496 |

Table Appendix B.3: Starting points and optimized results for pattern search and fminsearch solver for a specific stopping criteria

| Pattern search; function tolerance 0.001 | | | fminsearch; function tolerance 0.001 | | |
|---|---|---|---|---|---|
| Starting point (m) | Optimum $h_r$(m) | Max $\eta_{total,th}$ | Starting point (m) | Optimum $h_r$(m) | Max $\eta_{total,th}$ |
| 26 | 25.75 | 0.2486 | 14 | 21.7 | 0.2485 |
| 6 | 22.875 | 0.2504 | 25 | 22.85 | 0.2496 |
| 16 | 25 | 0.2493 | 3.3 | 24.915 | 0.2485 |
| 2.1 | 24 | 0.2486 | 11.34 | 24.381 | 0.2494 |
| 27.4 | 23.44 | 0.2489 | 25.5 | 26.217 | 0.2484 |
| 29.3 | 24.8 | 0.2494 | 29 | 23.2 | 0.2491 |
| 19.38 | 22.38 | 0.2488 | 20 | 22.98 | 0.2489 |
| 3 | 21.844 | 0.2486 | 5 | 23.78 | 0.2492 |

Table Appendix B.4: Starting points and optimized results for Simulated Annealing and Genetic Algorithm for a specific stopping criteria

| Simulated Annealing; function tolerance 0.001 | | | Genetic Algorithm; function tolerance 0.001 | | |
|---|---|---|---|---|---|
| Starting point (m) | Optimum $h_r$(m) | Max $\eta_{total,th}$ | Starting point (m) | Optimum $h_r$(m) | Max $\eta_{total,th}$ |
| 2.1 | 22.484 | 0.2498 | 22.998 | 0.2491 | 22.998 |
| 7 | 23.045 | 0.2503 | 22.600 | 0.2491 | 22.600 |
| 26 | 23.110 | 0.2494 | 22.747 | 0.2495 | 22.747 |
| 4 | 22.260 | 0.2493 | | | |
| 2.1 | 22.484 | 0.2498 | | | |

Table Appendix B.5: Detailed optimization results of three optimization algorithms for number of mirrors, $n_m$ =10

| | | Pattern search | | | Simulated Annealing | | | Genetic Algorithm | | |
|---|---|---|---|---|---|---|---|---|---|---|
| | | initial point (m) | optimized variable (m) | Max $\eta_{total,th}$ | initial point (m) | optimized variable (m) | Max $\eta_{total,th}$ | initial point | optimized variable (m) | Max $\eta_{total,th}$ |
| 1st run | $h_r$ | 3 | 10.5 | 0.1713 | 2 | 9.92 | 0.1715 | | 8.92 | 0.1711 |
| | $w_r$ | 0.19 | 0.878 | | 0.1 | 0.852 | | | 0.799 | |
| | $w_m$ | 0.14 | 0.89 | | 0.1 | 0.861 | | | 0.833 | |
| | $s_m$ | 0.06 | 0.247 | | 0.05 | 0.103 | | | 0.115 | |
| 2nd run | $h_r$ | 3 | 11 | 0.1701 | 3 | 9.9 | 0.1703 | | 10.276 | 0.1715 |
| | $w_r$ | 0.19 | 0.8 | | 0.19 | 0.867 | | | 0.867 | |
| | $w_m$ | 0.14 | 0.89 | | 0.14 | 0.889 | | | 0.885 | |
| | $s_m$ | 0.16 | 0.285 | | 0.06 | 0.076 | | | 0.157 | |
| 3rd run | $h_r$ | 3 | 10 | 0.1717 | 3 | 8.738 | 0.1697 | | 9.86 | 0.1719 |
| | $w_r$ | 0.19 | 0.878 | | 0.19 | 0.81 | | | 0.873 | |
| | $w_m$ | 0.14 | 0.89 | | 0.14 | 0.788 | | | 0.902 | |
| | $s_m$ | 0.06 | 0.193 | | 0.06 | 0.166 | | | 0.177 | |
| average time (minutes) | | 5 to 10 | | | 70 to 90 | | | 60 | | |

Table Appendix B.6: Results of the exhaustive search for $n_m$=30

| $h_r$ (m) | $w_r$ (m) | $w_m$ (m) | $s_m$ (m) | Max $\eta_{total,th}$ | Max $\eta_{total,th}$ (rounded) |
|---|---|---|---|---|---|
| 25 | 0.9 | 0.7 | 0.17 | 0.226448 | 0.226 |
| 21 | 0.9 | 0.7 | 0.05 | 0.226256 | 0.226 |
| 25 | 0.9 | 0.7 | 0.25 | 0.226113 | 0.226 |
| 21 | 0.9 | 0.7 | 0.09 | 0.225855 | 0.226 |
| 21 | 0.9 | 0.7 | 0.13 | 0.225532 | 0.226 |
| 25 | 0.9 | 0.7 | 0.21 | 0.22529 | 0.225 |
| 25 | 0.9 | 0.7 | 0.13 | 0.22517 | 0.225 |
| 25 | 0.9 | 0.7 | 0.09 | 0.22489 | 0.225 |
| 17 | 0.9 | 0.7 | 0.13 | 0.22455 | 0.225 |
| 17 | 0.9 | 0.7 | 0.21 | 0.22446 | 0.224 |
| 17 | 0.9 | 0.7 | 0.17 | 0.22439 | 0.224 |
| 25 | 0.9 | 0.7 | 0.29 | 0.224016 | 0.224 |
| 21 | 0.7 | 0.7 | 0.05 | 0.223717 | 0.224 |
| 21 | 0.9 | 0.7 | 0.21 | 0.223601 | 0.224 |
| 17 | 0.9 | 0.7 | 0.25 | 0.22351 | 0.224 |

Table Appendix B.7: Detailed optimization results of three optimization algorithms for number of mirrors, $n_m$ =30

| | | Pattern search | | | Simulated Annealing | | | Genetic Algorithm | | |
|---|---|---|---|---|---|---|---|---|---|---|
| | | initial point (m) | optimized variable (m) | Max $\eta_{total,th}$ | initial point (m) | optimized variable (m) | Max $\eta_{total,th}$ | initial point | optimized variable (m) | Max $\eta_{total,th}$ |
| 1st run | $h_r$ | 15 | 23 | 0.2296 | 9 | 18.563 | 0.2302 | | 21.01 | 0.2301 |
| | $w_r$ | 0.56 | 0.81 | | 0.9 | 0.742 | | | 0.806 | |
| | $w_m$ | 0.57 | 0.632 | | 0.8 | 0.582 | | | 0.678 | |
| | $s_m$ | 0.23 | 0.214 | | 0.07 | 0.074 | | | 0.09 | |
| 2nd run | $h_r$ | 5 | 23 | 0.2302 | 12 | 18.671 | 0.2294 | | 20.295 | 0.2322 |
| | $w_r$ | 0.2 | 0.825 | | 1 | 0.779 | | | 0.813 | |
| | $w_m$ | 1.13 | 0.661 | | 0.4 | 0.648 | | | 0.676 | |
| | $s_m$ | 0.17 | 0.186 | | 0.22 | 0.08 | | | 0.073 | |
| 3rd run | $h_r$ | 15 | 23 | 0.2306 | 18 | 23.109 | 0.2297 | | 20.539 | 0.2319 |
| | $w_r$ | 1 | 0.797 | | 1.16 | 0.818 | | | 0.806 | |
| | $w_m$ | 0.8 | 0.675 | | 0.7 | 0.727 | | | 0.654 | |
| | $s_m$ | 0.27 | 0.184 | | 0.13 | 0.108 | | | 0.1 | |
| average time (minutes) | | 5 to 10 | | | 90 to 100 | | | 85 | | |

Table Appendix B.8: Results of the exhaustive search for $n_m$=54

| $h_r$(m) | $w_r$(m) | $w_m$(m) | $s_m$(m) | Max $\eta_{total,th}$ | Max $\eta_{total,th}$(rounded) |
|---|---|---|---|---|---|
| 29 | 0.7 | 0.5 | 0.09 | 0.246946 | 0.247 |
| 21 | 0.9 | 0.5 | 0.17 | 0.246915 | 0.247 |
| 21 | 0.7 | 0.5 | 0.09 | 0.246669 | 0.247 |
| 21 | 0.7 | 0.5 | 0.13 | 0.246664 | 0.247 |
| 21 | 0.7 | 0.5 | 0.17 | 0.246465 | 0.246 |
| 21 | 0.7 | 0.5 | 0.21 | 0.246386 | 0.246 |
| 25 | 0.7 | 0.5 | 0.05 | 0.246302 | 0.246 |
| 29 | 0.7 | 0.5 | 0.05 | 0.246069 | 0.246 |
| 21 | 0.9 | 0.5 | 0.09 | 0.245364 | 0.245 |
| 25 | 0.9 | 0.5 | 0.21 | 0.245176 | 0.245 |
| 29 | 0.9 | 0.5 | 0.05 | 0.245051 | 0.245 |
| 25 | 0.9 | 0.5 | 0.13 | 0.245012 | 0.245 |
| 29 | 0.9 | 0.5 | 0.09 | 0.244998 | 0.245 |
| 17 | 0.7 | 0.5 | 0.13 | 0.244974 | 0.245 |
| 25 | 0.9 | 0.5 | 0.25 | 0.244865 | 0.245 |
| 21 | 0.9 | 0.5 | 0.25 | 0.244788 | 0.245 |
| 21 | 0.9 | 0.5 | 0.13 | 0.244615 | 0.245 |

Table Appendix B.9: Detailed optimization results of three optimization algorithms for number of mirrors, $n_m$ =54

| | | Pattern search | | | Simulated Annealing | | | Genetic Algorithm | | |
|---|---|---|---|---|---|---|---|---|---|---|
| | | initial point (m) | optimized variable (m) | Max $\eta_{total,th}$ | initial point (m) | optimized variable (m) | Max $\eta_{total,th}$ | initial point | optimized variables (m) | Max $\eta_{total,th}$ |
| 1st run | $h_r$ | 21 | 25 | 0.2506 | 28 | 20.225 | 0.2514 | | 20.862 | 0.2515 |
| | $w_r$ | 0.11 | 0.86 | | 0.7 | 0.782 | | | 0.841 | |
| | $w_m$ | 1.1 | 0.6 | | 0.14 | 0.491 | | | 0.553 | |
| | $s_m$ | 0.09 | 0.137 | | 0.26 | 0.095 | | | 0.137 | |
| 2nd run | $h_r$ | 10 | 21.984 | 0.2519 | 15 | 20.67 | 0.2505 | | 28.567 | 0.2512 |
| | $w_r$ | 0.21 | 0.772 | | 0.5 | 0.775 | | | 0.77 | |
| | $w_m$ | 1.11 | 0.548 | | 0.4 | 0.501 | | | 0.491 | |
| | $s_m$ | 0.29 | 0.114 | | 0.16 | 0.146 | | | 0.106 | |
| 3rd run | $h_r$ | 23 | 24.5 | 0.2499 | 21 | 25.534 | 0.2498 | | 21.188 | 0.2512 |
| | $w_r$ | 0.18 | 0.867 | | 0.11 | 0.85 | | | 0.791 | |
| | $w_m$ | 0.87 | 0.612 | | 1.1 | 0.56 | | | 0.53 | |
| | $s_m$ | 0.27 | 0.09 | | 0.09 | 0.182 | | | 0.141 | |
| Average time (minutes) | | 10 | | | 125 | | | 110 | | |

# Appendix C

Table Appendix C.1: Optimized LFR designs for different mirror cost drops

| | $h_r$(m) | $n_m$ | $w_m$(m) | $s_m$(m) | $T_r$(°C) | LCOE (€/kWh) | A(m²) |
|---|---|---|---|---|---|---|---|
| PSA, Spain | 8.86 | 22 | 0.628 | 0.101 | 300* | 0.072 | 13.82 |
| Cost 20% drop | 8.82 | 34 | 0.433 | 0.073 | 300* | 0.065 | 14.7 |
| Cost 40% drop | 8.4 | 34 | 0.436 | 0.068 | 300* | 0.059 | 14.8 |
| Cost 60% drop | 8.7 | 48 | 0.319 | 0.052 | 300* | 0.052 | 15.3 |

Table Appendix C.2: Three GA optimization runs for each LFR configuration and operating temperature condition

| Primary mirror type | $\eta_{total,th}$ maximized | $h_r$(m) | $n_m$ | $w_m$(m) | $s_m$(m) | $T_r$(°C) | $A_m$(m²) | $A_L$(m²) |
|---|---|---|---|---|---|---|---|---|
| | Variable receiver temperature operating condition | | | | | | | |
| Curved | 0.2820 | 2.344 | 30 | 0.0899 | 0.0693 | $T_r \leq 250$ | 2.6970 | 4.7067 |
| | 0.2826 | 2.341 | 38 | 0.0666 | 0.0574 | | 2.5308 | 4.6546 |
| | 0.2825 | 2.056 | 40 | 0.0662 | 0.0526 | | 2.6480 | 4.6994 |
| | 0.3065 | 2.645 | 44 | 0.0838 | 0.0504 | $T_r \leq 400$ | 3.6872 | 5.8544 |
| | 0.3034 | 2.701 | 28 | 0.1315 | 0.0539 | | 3.6820 | 5.1373 |
| | 0.3026 | 3.045 | 26 | 0.1477 | 0.0769 | | 3.8402 | 5.7627 |
| Slightly Curved | 0.2783 | 2.182 | 50 | 0.0525 | 0.0505 | $T_r \leq 250$ | 2.6250 | 5.0995 |
| | 0.2788 | 2.004 | 56 | 0.0500 | 0.0503 | | 2.8000 | 5.5665 |
| | 0.2784 | 2.066 | 50 | 0.0511 | 0.0503 | | 2.5550 | 5.0197 |
| | 0.2848 | 6.654 | 30 | 0.2417 | 0.1523 | $T_r \leq 400$ | 7.2510 | 11.6677 |
| | 0.2996 | 2.109 | 62 | 0.0599 | 0.0501 | | 3.7138 | 6.7699 |
| | 0.2873 | 6.190 | 30 | 0.2066 | 0.1657 | | 6.1980 | 11.0033 |
| Flat | 0.2493 | 4.396 | 36 | 0.1004 | 0.0566 | $T_r \leq 250$ | 3.6144 | 5.5954 |
| | 0.2492 | 4.263 | 30 | 0.1004 | 0.0848 | | 3.0120 | 5.4712 |
| | 0.2497 | 4.226 | 32 | 0.1004 | 0.0740 | | 3.2128 | 5.5068 |
| | 0.2792 | 5.505 | 60 | 0.1045 | 0.0581 | $T_r \leq 400$ | 6.2700 | 9.6979 |
| | 0.2788 | 5.639 | 62 | 0.1013 | 0.0743 | | 6.2806 | 10.8129 |
| | 0.2710 | 5.521 | 44 | 0.1217 | 0.1071 | | 5.3548 | 9.9601 |

| | Constant receiver temperature operating condition | | | | | | | |
|---|---|---|---|---|---|---|---|---|
| | 0.3017 | 3.26 | 24 | 0.156 | 0.102 | 363 | 3.7440 | 6.0900 |
| Curved | 0.3016 | 3.422 | 24 | 0.1643 | 0.1095 | 363 | 3.9432 | 6.4617 |
| | 0.3004 | 3.441 | 20 | 0.2086 | 0.1183 | 364 | 4.1720 | 6.4197 |
| | 0.2969 | 2.382 | 66 | 0.0587 | 0.0554 | 399 | 3.8720 | 7.4702 |
| Slightly curved | 0.2970 | 3.92 | 60 | 0.0762 | 0.0578 | 371 | 4.5720 | 7.9822 |
| | 0.2891 | 6.375 | 36 | 0.1988 | 0.1389 | 424 | 7.1568 | 12.0183 |
| | 0.2887 | 4.958 | 78 | 0.0677 | 0.0535 | 388 | 5.2806 | 9.4001 |
| Flat | 0.2868 | 5.043 | 72 | 0.0687 | 0.0635 | 382 | 4.9464 | 9.4549 |
| | 0.2869 | 4.673 | 66 | 0.0755 | 0.0570 | 385 | 4.9830 | 8.6880 |

Table Appendix C.3: Multiple LCOE optimization runs conducted for PSA, Spain

| $h_r$(m) | $n_m$ | $w_m$(m) | $s_m$(m) | LCOE (cents of €/kWh) |
|---|---|---|---|---|
| 8.8593 | 22 | 0.6278 | 0.1008 | 7.2166 |
| 8.8394 | 22 | 0.6208 | 0.1006 | 7.2104 |
| 8.8583 | 24 | 0.6060 | 0.1025 | 7.1686 |
| 8.8690 | 22 | 0.6189 | 0.0994 | 7.1537 |
| 8.7639 | 22 | 0.6253 | 0.1070 | 7.1982 |
| 8.9106 | 22 | 0.6156 | 0.1010 | 7.2019 |
| 8.8388 | 22 | 0.6303 | 0.1017 | 7.1982 |

# Appendix D

## Modelling results of existing prototypes

The method presented in this study was applied on two LFR prototypes: a plant installed in Vallipuram, India (Chaitanya Prasad, Reddy, and Sundararajan 2017; Balaji, Reddy, and Sundararajan 2016) and a design inspired by the well-known FRESDEMO prototype. Vallipuram plant has a similar receiver design modelled in this study; FRESDEMO prototype used a single tube receiver and a CPC, however the receiver aperture area is 20% higher compared to the current this study. An exact value for primary mirror curvature is not reported in either of these LFR plants. Therefore, Vallipuram plant was modelled as a fully curved mirror scenario similar to Balaji et al. (2016). The FRESDEMO inspired system was model as a slightly curved mirror scenario, which was similar to the actual design. Figure Appendix D.1shows current and optimized performance of Vallipuram system under different receiver temperatures. It is clear that the existing system cannot achieve a similar efficiency to the optimized system even though the receiver temperature is maintained at the maximum possible level. Table Appendix D.1 shows a detailed comparison of the optimized systems against existing LFR systems.

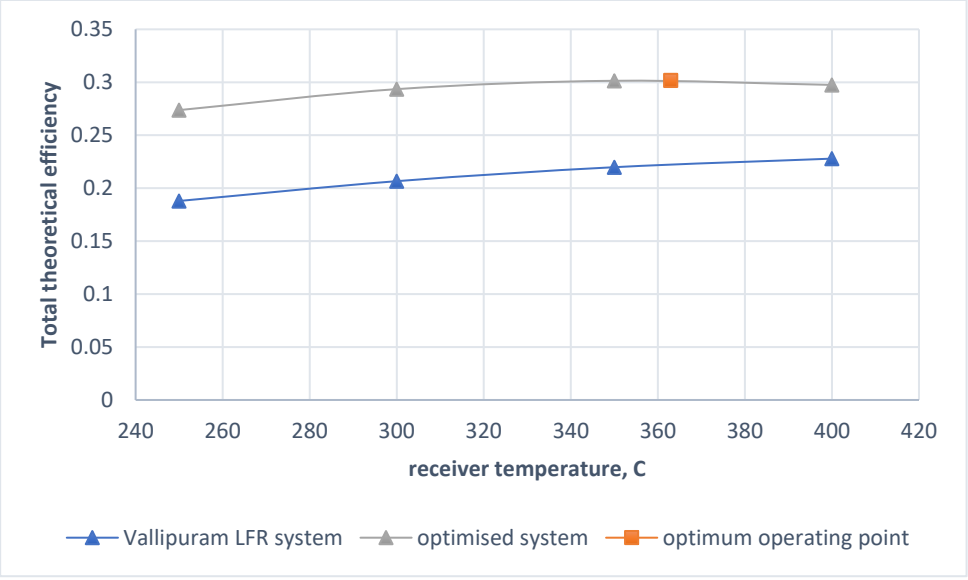


Figure Appendix D.1: Comparison of existing vs optimized designs of Vallipuram LFR system

Table Appendix D.1: Optimized results against existing designs of Vallipuram prototype and FRESDEMO inspired LFR design

| | Vallipuram LFR system | | FRESDEMO inspired system | |
|---|---|---|---|---|
| | Existing (Chaitanya Prasad, Reddy, and Sundararajan 2017), (Balaji, Reddy, and Sundararajan 2016) | Optimized | Non-optimized (Bernhard et al. 2008) | Optimized |
| $h_r$(m) | 7.9 | 3.26 | 8 | 3.92 |
| $n_m$ | 12 | 24 | 25 | 60 |
| $w_m$(m) | 1.07 | 0.156 | 0.6 | 0.0762 |
| $s_m$(m) | 0.43 | 0.102 | 0.25 | 0.0578 |
| $T_r$(°C) | 363 | 363 | 371 | 371 |
| $A_m$(m²) | 12.84 | 3.74 | 15 | 4.57 |
| $A_L$(m²) | 17.57 | 6.09 | 21 | 7.98 |
| $\eta_{total,th}$ | 0.2224 | 0.3017 | 0.2288 | 0.297 |
| Power output (kWh/m/d) | 12.19 | 4.5 | 13.78 | 5.6 |
| $A_m$ needed to obtain non-optimized power output (m²) | - | 10.16 | - | 11.24 |
| $A_L$ needed to obtain non-optimized power output (m²) | - | 16.5 | - | 19.63 |
| Mirror area saving | - | 20.87% | - | 25.07% |
| Land area saving | - | 6.09% | - | 6.52% |

| | | | | |
|---|---|---|---|---|
| Efficiency improvement | - | 35% | - | 30% |

Results indicate that a significant improvement can be achieved in terms of efficiency and mirror area by optimizing the existing LFR systems. 35% and 30% efficiency improvement can be achieved for Vallipuram and FRESDEMO inspired systems, respectively. Optimized designs employ narrow mirrors to reduce optical losses and result to compact systems showing a smaller mirror area per meter length of the plant. This causes power output to drop in comparison to non-optimized systems demanding longer or multiple systems to get the same power output. However, an optimized system can still show a saving in terms of mirror and land areas. For instance, optimized designs can save 21% and 25% mirror area after generating the same power output as in Vallipuram and FRESDEMO inspired systems. As optimized designs used more mirrors, land area saving was only around 6% for both cases.